3D Printed driving mechanism design for a high-speed reciprocating needle used during vitrectomy

Daisy Robijns
Delft University of technology
Master of Science in Mechanical Engineering
Track: BioMechanical Design
August 31, 2022

Supervised by: ir. K. M. Lussenburg, Prof. dr. ir. P. Breedveld and dr. M.J. Mirzaali

ABSTRACT

Vitrectomy is an often performed procedure during eye surgery and requires a high-precision vitreous cutter. The production of these precise and lightweight vitreous cutters sets high demands on the manufacturing process. Trained technicians must assemble the device step by step and continuously check and validate the manufacturing process. Additive manufacturing on the contrary allows for non-assembly mechanisms that can be printed at once without requiring any post-assembling steps. However, a high-speed vitreous cutter design suitable for 3D Printing is not yet presented. This research aimed to deliver a 3D Printed driving mechanism design for a high-speed reciprocating needle used during vitrectomy that does not require post assembly steps from trained technicians.

It was established that the driving mechanism should reciprocate two concentric needles by air pressure to cut vitreous. Currently used actuators are investigated and a prior attempt for a non-assembly vitreous cutter is analysed. The diaphragm and bellow-based design were considered a potential solution path. A suitable design for both potential solution paths is made. The bellow design consists of an inner and outer bellow to allow the passage of the needle. The diaphragm concept is already used for the first and only attempt to produce a non-assembly vitreous cutter. This prior attempt is further analysed and it became clear the damping of the diaphragm needed to be decreased to increase the speed of the backward motion. Therefore, a planar spring is added to the dual flat diaphragm design. Finally, the spring-reinforced dual flat diaphragm concept is selected for continuation and tested by using PolyJet prototypes.

Tests are executed to determine if the requirements could be met, especially focussing on the speed and force requirements. Different spring shapes and thicknesses are tested. It became clear that the behaviour of the spring-reinforced diaphragms is suboptimal. The return time is higher than preferred and damping is still present in a large extent due to hysteresis. To improve the design it was decided to continue with tests where the start position is relocated to form a pretension and overcome the damping seen especially at the last part of the return stroke. Pretension appeared successful and showed a 98% decrease in return time, but the requirements for the speed could not be obtained. Altering the thickness of the spring led to a sufficient high backward force but did not show direct influence on the speed of the backward motion.

Overall, a non-assembly vitreous cutter driving mechanism is made but not all requirements could be met. Exploring design directions which do have some drawbacks should be considered to offer a solution in the near future. Designing a driving mechanism that also requires 3D Printed flexible material, first requires a thoroughly material investigation to identify the mechanical properties and time-dependent behaviour such that a trustworthy design optimization can be made. However, a design for a non-assembly high-speed vitreous cutter is made and with the upcoming developments in the 3D Printing techniques and materials the design might form the basis of a high-speed vitreous cutter. This research tested the most ideal case and gave further insight bringing us a step closer towards a non-assembly high-speed vitreous cutter.

Keywords **--** additive manufacturing, 3D Printing, non-assembly, print-in-place, vitreous cutter, spring, spring reinforced diaphragm

CONTENTS

1 Introduction 4
1.1 Background vitrectomy 4
1.2 Background additive manufacturing 4
1.3 Problem definition 5
1.4 The goal of this study 5
1.5 The layout of the report 5
2 Analysis 5
2.1 State of the art 5
2.1.1 Vitreous cutters 5
2.1.2 DORC vitreous cutter 6
2.2 Function analysis 7
2.2.1 General function analysis 7
2.2.2 Specified function analysis 7
2.3 Design requirements 8
3 Pneumatic actuators 10
3.1 Introduction 10
3.2 Rotary actuators 10
3.2.1 Potential design directions 10
3.2.2 Feasibility of design directions 11
3.3 Linear actuators 11
3.3.1 Potential design directions 11
3.3.2 Feasibility of design directions 12
4 Dual flat diaphragm actuator 13
4.1 Prior attempt to 3D print a vitreous cutter 13
4.2 Theoretical working principle dual flat diaphragm actuator 14
4.3 Function analysis for redesigning 15
4.4 Mass-spring-damper model 15
4.5 Improving the dual flat diaphragm design 16
4.5.1 Adding a driving force 16
4.5.2 Increasing the spring constant 17
4.5.3 Reducing the damping coefficient 17
5 Spring reinforced dual flat driving mechanism design 18
5.1 Selection design direction 18
5.2 Spring configuration 19
5.3 Material and AM technique 19
5.4 Spring shape 20
5.5 Embodiment vitreous cutter design 21

6 Evaluation of varying spring designs 22
6.1 Test goal 22
6.2 Prototypes 22
6.3 Speed test 23
6.3.1 Test procedure and setup 23
6.3.2 Hypothesis 24
6.3.3 Test results and evaluation 24
6.4 Force test 25
6.4.1 Test procedure and setup 25
6.4.2 Hypothesis 25
6.4.3 Test results and evaluation 26
6.5 Overall test evaluation 27
6.6 Improving the design 27
7 Evaluation of varying relocated start positions 28
7.1 Prototypes 28
7.2 Test goal 28
7.3 Force test 28
7.3.1 Test procedure and setup 28
7.3.2 Hypothesis 29
7.3.3 Test results and evaluation 29
7.4 Speed test 29
7.4.1 Test procedure and setup 29
7.4.2 Hypothesis 30
7.4.3 Test results and evaluation 31
7.5 Overall test evaluation 33
8 Discussion 33
8.1 Progress 33
8.2 Test Limitations 33
8.3 Design limitations 35
8.4 Recommendations and further research 35
9 Conclusion 36
10 References 36
Appendix I Bellow-driven driving mechanism design 40
Appendix II Prototypes batch 1 42
Appendix III Prototypes batch 2 51
Appendix IV Fixtures 57
Appendix V Labview program Micro Epsilon ILD1420-10 laser 61
Appendix VI Labview program Micro Epsilon ILD1750-2 laser 62
Appendix VII Calculation minimal thickness 63

3D Printed driving mechanism design for a high-speed reciprocating needle used during vitrectomy

Daisy Robijns
Delft University of technology
August 31, 2022

1 INTRODUCTION

1.1 Background vitrectomy

In his private garage, David Kasner came to the radical conclusion that vitreous could be safely removed from the eye where after he tested his idea in 1961 on an eight-year-old boy who suffered from an injury due to a tent state [1]. Kasner paved the way for the now standard vitrectomy procedure, where the vitreous gel that fills the eye is aspirated. Clear vitreous allows the passage of light onto a thin tissue at the inner back wall of the eye. This fragile tissue, called the retina, as indicated in Fig. 1, transfers light to neural signals such that a person can see. Removing the vitreous is a valuable procedure to restore or improve vision. Vitrectomy can remove unclear vitreous or allow better access to the retina by decreasing the traction on the retina during surgery. To indicate the occurrence of this procedure, in England alone, 26,900 vitrectomies were reported in 2018 [2].

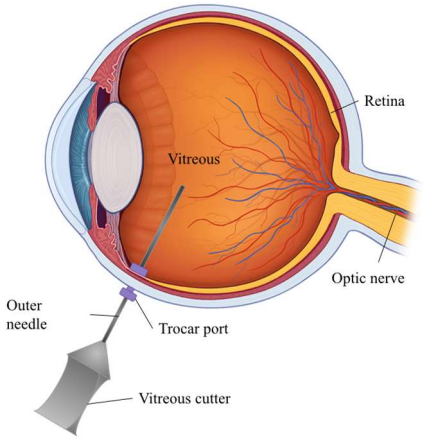

Fig. 1. Cross-section of the eye indicating the vitreous, retina, vitreous cutter and trocar port (Adapted from [3])

Since vitreous contains structural macromolecules like hyaluronan, proteoglycans, collagens and non-collagenous pro-teins in addition to around 99% water, the vitreous is cut before it is aspirated [4]. Cutting the vitreous is necessary to prevent traction forces on the retina that might be damaging [5]. Moreover, increasing the cut-rate decreases the viscosity of the vitreous composition, which results in a higher flow rate when transporting vitreous out of the eye [4],[5]. Accordingly, high-speed vitrectomy with up to 7500 cuts per minute improves fragmentation of the vitreous, resulting in lower viscosity and a higher flow rate, which reduces the procedure time [8]. In a modern high-speed vitrectomy, two concentric hollow needles are used to cut the vitreous. The needles are inserted through a trocar port at the side of the eye, as indicated in Fig. 1. The inner needle moves with respect to the outer needle at a high frequency to cut the vitreous. Simultaneously a vacuum is applied to the inner needle to aspirate the vitreous. Simultaneously, a saline solution is inserted into the eye to maintain the eye's internal pressure and shape.

1.2 Background additive manufacturing

Additive manufacturing (AM) or 3D Printing is a relatively new manufacturing technique that is rising in popularity and use. AM already has revolutionary applications in biomedical, aerospace, buildings and protective structures [9]. AM deposits material in a layer-by-layer manner, allowing users to freely design complex shapes without the limitations of conventional subtractive techniques. With AM, almost the same production time is needed for a geometrical shape like a cube and a complex shape with the same volume. AM directly creates a physical object from a computer-aided design (CAD). The technique has already been used for two decades to create fast prototypes. Recently, AM is also frequently used to produce functional end-user components [10]. The final prints can be made with multiple techniques based on a layering approach, like extrusion-based techniques, material jetting, binder jetting, sheet lamination, vat photopolymerization, powder bed fusion, directed energy deposition or direct write technologies.

AM also allows the fabrication of non-assembly mechanisms, which can be created without any post-assembling steps [11]. Therefore, overall production time can be reduced, and assembly technicians become superfluous. Moreover, costs can be reduced and friction losses limited. However, designing non-assembly mechanisms suitable for AM requires another solution path than manufacturing traditional mechanisms [12]. Multiple difficult design choices need to be made. Aside from the geometrical design, the proper AM process and

suitable material must be selected. AM allows for a wide range of materials, and also multi-material prints can be made. Moreover, printer settings still need to be optimized for each design. Overall, AM offers opportunities, but challenges need to be overcome.

1.3 Problem definition

Vitreous cutters are often small and lightweight to maximize the surgeon's comfort and enhance the precision required during vitrectomy [13]. However, the production of precise and lightweight vitreous cutters sets high demands on the manufacturing process. Trained technicians must assemble the device step by step and continuously check and validate the manufacturing process. During a conventional manufacturing process, individual parts are produced before being assembled in the final mechanism. This assembly process costs relatively much time and money, while high accuracy is required to prevent failure due to poor positioning of parts [14].

In contrast, AM allows for non-assembly mechanisms that can be printed at once without requiring any post-assembling steps. As a result, AM appears to be a valuable technique for manufacturing a driving mechanism for a high-speed reciprocating needle used during vitrectomy. However, conventional designs can often not be immediately transferred to a format suitable for AM. As a result, there is no AM driving mechanism design capable of translating the vitreous cutter needle at high frequencies until now. The required time for the forward and backward motion of previously 3D Printed prototypes shows a maximal cutting frequency potential more than 30 times lower than comparable devices with a rate of 8000 pulses/minute [15]. However, the cutting rate is crucial to decrease traction forces on the retina and increase the flow rate by lowering the viscosity of the vitreous. Overall, AM might overcome the current assembly difficulties of small vitreous cutter parts, but a suitable AM design is not yet presented.

1.4 The goal of this study

Since vitrectomy is an often performed procedure, the design of the vitreous cutter affects a large target group, emphasizing the importance of design improvements in this field. The aim of this study is to deliver a non-assembly 3D Printed driving mechanism design for a high-speed reciprocating needle used during vitrectomy. In this way, the need for trained technicians for assembly can be eliminated. Additionally, the goal is to validate the design through prototypes and tests. Hence comparisons regarding the specification of the design with current available vitreous cutters can be made. Special focus will be placed on the high-speed frequency requirements.

1.5 The layout of the report

This study is conducted in cooperation with Tu Delft and the Dutch Ophthalmic Research Centre (DORC). The study concerns a follow-up research on Stolk et al. [15] In this first chapter an introduction is given, the problem defined and the goal stated. In the second chapter, an analysis is made to identify the working of the current available vitreous cutters and identify the functions the device should fulfil. With this knowledge, the design requirements are formulated. In the third chapter, existing pneumatic actuators are explored to identify potential new design directions for the vitreous cutter. In the fourth chapter, the dual flat diaphragm is researched to determine if design adaptations might form a potential solution path. The working of the device is analyzed and points of improvement are formed by looking into the analysis of the design. In chapter 5, bot potential design directions formed by the pneumatic actuator research and improvements of dual flat diaphragm design are further specified by making a design suitable for the vitreous cutter. The most suitable design is selected for further tests. In chapter 6, tests are executed and results evaluated. Further improvements are stated and tested in the next chapter seven. Finally, the research is discussed by evaluating the test limitations, design limitations and recommendations for further research. Lastly, a conclusion is stated.

2 ANALYSIS

2.1 State of the art

2.1.1 Vitreous cutters

Many improvements followed after introducing the first vitreous cutter, which consisted of a drill powered by a regular battery[16]. Currently, vitreous cutters comprise two concentric needles. The needles can be inserted through trocar ports at the pars plana section of the eye. This section on the side of the eye has no known functions and allows for entrance into the eye without damaging the retina or the lens. The trocar port allows entering the eye through the same incision multiple times without releasing the pressure inside the eye. The small needles only require a small opening which minimizes the harm to the patient. The surgeon manually executes the insertion and position of the needles. Therefore the devices are made small and light to allow optimal user comfort.

If the needles are positioned, the vitreous can be separated from the retina by moving the concentric needles with respect to each other. By moving the needles at a high frequency, the macromolecules inside the vitreous are cut. After cutting the vitreous into

smaller pieces, the vitreous can be aspirated through the same needle and transported out of the eye. After that, the vitreous parts can be transported through the device. The patent review of Stolk et al. [17] describes a structured overview of all mechanisms used to drive the two concentric needles. The patents are categorized by two characteristics: the cutting motion of the needles and the engine type, as depicted in Fig. 2.

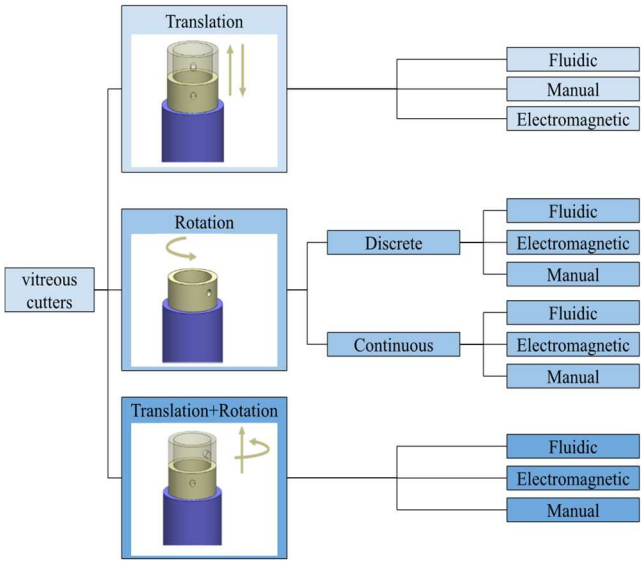

Fig. 2. Schematic representation of vitreous cutter patents categorization (Adapted from [17]*)*

The cutting motion of the needles can be obtained due to the relative movement between the two concentric needles. The outer needle is attached to the housing such that the needle stands still with respect to the inner needle, which is attached to the driving mechanism. Before cutting the vitreous, a small part of the vitreous is pulled inside the needle through the hole located at the tip of the outer needle. When the tip edge of the inner needle moves past the hole in the outer needle, a small part of the vitreous is cut off. A two-dimensional cutting cycle can be established when there is also a hole located at the tip of the inner needle. During a two-dimensional cutting cycle, the vitreous is cut in both the forward and backward motion. A schematic representation of a two-dimensional cutting cycle is given in Fig. 3. In the patent review of Stolk et al [17] it can be seen that the movement of the inner needle is either translating, rotating, or a combination of translating and rotating.

Multiple power supplies can drive the inner needle. The patents included by Stolk et al. [17] are categorized into three engine types: fluidic, electromagnetic and manual. Currently, a pneumatic-driven device is most common. Aside from the power supply for the driving mechanism, a vacuum is used to aspirate the separated vitreous pieces and transport the vitreous out of the eye. Using vacuum or pressure allows the device to be relatively lightweight. In addition, the devices can be implemented in a design as small as a marker such that surgeons can operate at high precision. Overall, there exists a wide range of vitreous cutter designs but they all have in common that trained technicians are required to assemble multiple small parts.

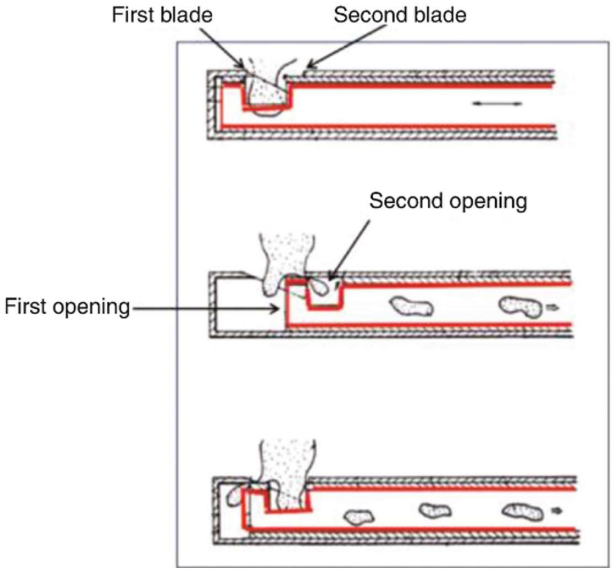

Fig. 3. Schematic representation of a two-dimensional cutting cycle where vitreous is cut both during the forward and backward motion. (Taken from [18])

2.1.2 DORC vitreous cutter

One example of a state-of-the-art vitreous cutter currently still used by surgeons is the 8268.VIT23 disposable high-Speed two-dimensional Cutter [19]. This device, depicted in Fig. 4, is developed and produced by DORC. A cross-section of the device is depicted in Fig 4 (a) to provide insight into the working principle. The air inlet of the vitreous cutter is connected by Festo tubes to the EVA pressure supply system [20]. EVA uses a fluid control system called Vacuflow VTi to deliver a precise flow pulsation to the vitreous cutter. The air pressurizes the air chamber, whereafter the diaphragm, with the attached inner needle, is pushed forward. The outer needle is attached to the housing such that the two concentric needles move with respect to each other. To cut the vitreous, the tip of the inner and outer needle has a hole like depicted in Fig. 4 (b). When the air chamber is depressurized, the helical spring pushes the diaphragm with the attached inner needle back to its initial position. The vitreous is cut both during the forward motion driven by the pressurized air and during the backward motion driven by the helical spring. Cut vitreous pieces are aspirated and transported through the hollow needle to the outlet on the back of the device.

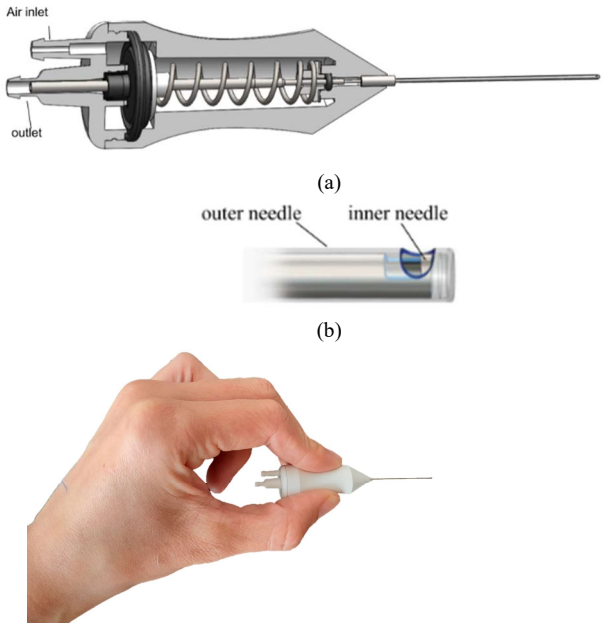

Fig. 4. Vitreous cutter by DORC (a) cross section 3D Model 8268.VIT23 (b) 3D model needle tiple (adapted from [19] *) (c) picture of the device*

2.2 Function analysis

2.2.1 General function analysis

After analysing the working principles of the current vitreous cutters, a function analysis can identify the general working and additional main functions a device should fulfil. By developing an abstract model, the solution space will not be limited by pre-defined design choices allowing for a broad spectrum of design solutions and stimulating creativity. The most abstract model can be described as a black box with additional material- and energy flow. In the case of the vitreous cutter, the device's primary function is to remove the vitreous from the eye. The input consists of power and the vitreous, resulting in the final output of the removed vitreous, as depicted in Fig. 5.

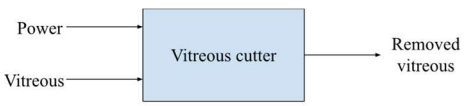

Fig. 5. Black box model representing the general working of a vitreous cutter

The primary function can be broken down into more manageable subfunctions. In Fig. 6, the subfunctions of the device are displayed in chronological order. The device must fulfil the subfunctions in chronological order to complete the main function of removing the vitreous out of the eye. Firstly, the device must access the vitreous. After entering the eye, the device must be positioned at the correct location. After positioning, the vitreous must be cut and separated from the retina since the vitreous is attached to the retina by fibers. After cutting, the vitreous pieces should be grabbed and then transported out of the eye.

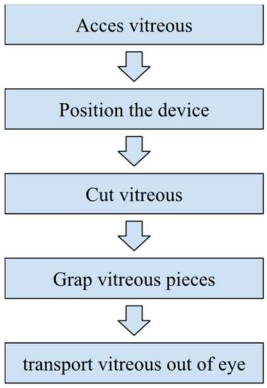

Fig. 6. Subfunctions in chronological order required to remove vitreous out of the eye

2.2.2 Specified function analysis

Since this study concerns a follow-up research, the design space can already be limited based on prior research. The relatively abstract function analysis described in the previous section can be specified. Pre-defined design choices are established for both the main function represented by the black box model in Fig. 5 and the subfunctions described in Fig. 6. The input power of the black box model should be pressurized-air and aspiration pressure. In the report by Stolk et al. [15] selecting a fluidic actuator is motivated by the use of electromagnetic and manual devices since electromagnetic devices are relatively heavy and manual devices are relatively difficult to operate. Overall pneumatic devices are preferred due to their relatively low cost, compact size, high power-to-weight ratio, reliability, and relative safety in high-risk environments [16].

Furthermore, the device should make use of two concentric hollow needles. The needles allow accessing the vitreous with minimum harm to the patient. After entering the eye, the vitreous can be cut, grabbed and removed out of the eye by using aspiration pressure. The positing of the device is determined to be a user task. Cutting the vitreous can be done by the relative movement of the two concentric needles. In the patent research of Stolk et al. [17] four cutting movements are identified: reciprocating translation, reciprocating rotation, continuous rotation and a combination of rotation and translation. Continuous rotation was mainly used in the early years but showed wind-up of the fibres around the needle, causing retinal detachment [21]. Aside from this negative effect of continuous rotation, it is still unknown which cutting movement is most effective.

It is decided to use a reciprocating translating cutting movement to stay in line with previous research and currently produced vitreous cutters by DORC. In Fig. 7, a black-box model of a pneumatic driving mechanism for a reciprocating needle is displayed. This black box model shows the main area of attention since this research mainly concerns a driving mechanism design. A non-assembly 3D Printed driving mechanism powered by pressurized air should translate two concentric needles at high frequency.

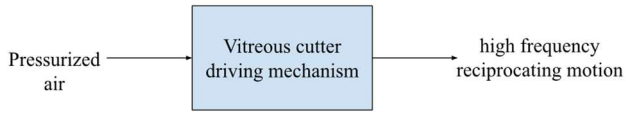

Fig. 7. Specified black-box model for a pneumatic driving mechanism of a reciprocating needle

2.3 Design requirements

The previous function analysis helps to establish design requirements. In Table *1* a list of design requirements is stated. The design requirements are divided into leading requirements and wishes, as indicated in the second column of Table *1*. The requirements must be met to offer a valuable design solution. The wishes, on the contrary, are requirements that should preferably be fulfilled and can be a reason to choose one concept over another. However, wishes might also be fulfilled in follow-up design improvements. The design requirements partly follow from the function analysis but are mainly based on target specifications. Target specifications are identified by selecting the vitreous cutter design from DORC, as described in the state of the art, as reference. This device was also selected by Stolk et al. [15] to serve as a reference. They formulated the requirements based on the 8268.VIT23 specifications, vitrectomy research and personal interviews with engineers working at DORC. Most design requirements are identical to the requirements set by Stolk et al. [15]. Therefore, easy comparisons can be made with previous non-assembly vitreous cutter research.

The first requirement is stated to overcome the main problem as described in the problem definition. The driving mechanism should be made by AM without requiring post-assembling steps of trained technicians (R.1). The device will not need a single post-processing step in the ideal case. However, designs requiring post-processing steps like support removal or easy assembling steps still offer a valuable solution to the stated problem, while trained technicians are no longer required. Nonetheless, AM comes with some additional limitations and guidelines that need to be taken into account, such as the minimal wall thickness, layer thickness, feature size, tolerances, and available material. Limitations and guidelines can differ for each AM technique but can also vary per machine. Therefore specific AM guidelines are not considered primary requirements but will be taken into account when specifying the design after selecting the suitable AM technique and machine.

The second requirement defines the power supply of the device. The driving mechanism should be powered by pressurized air (R.2). Furthermore,) to easily introduce the device to the market, the device should preferably be compatible with the EVA pressure supply system (R.3). The EVA pressure supply system is produced and brought on the market by DORC. This system is equipped with a Vacuflow fluid control system to deliver flow or vacuum precisely without unwanted additional flows or pulsations. The remaining requirements can be further elaborated by considering the subfunctions as noted in the function analysis.

Access the vitreous

First the device should access the vitreous with minimal harm to the patient. This requires a as small as possible access port into the eye to minimize the healing process. A small needle should be used that can enter the eye through trocar ports located at the pars planar section of the eye. Currently, it is not yet possible to produce reliable needles considering the limitations of AM. Therefore, the same needles as the 8268.VIT23 vitreous cutter from DORC will be used. Accordingly, it should be possible to attach a 0.32 mm diameter inner needle to the driving mechanism during or after printing (R-access.1). Since the device is used in a medical environment and comes in contact with the patient, the device should be preferably sterilizable and biocompatible (R-access.2).

Position the device

After inserting the needles, the device should be precisely positioned. This is best done by a trained surgeon. To allow for easy manoeuvring, the device should offer a good grip to the surgeon. Therefore, the handle of the device should have a maximal diameter of 16mm (R-position.1). This size, similar to 8268.VIT23 vitreous cutter from DORC, allows for a pen grip which is beneficial for stable and precise manoeuvring. The handle of the device should have a maximum length of 190 mm (R-position.2). To avoid discomfort, the maximum length is set to the length of a conventional pencil. Moreover, the device should preferably weigh less than 5 grams (R-position.3), similar to the 8268.VIT23 vitreous cutter from DORC.

Cut vitreous

When rightly positioned, the device should cut the vitreous into small pieces in order to separate the vitreous from the retina and lower the viscosity. The force required to cut vitreous and the most optimal cutting motion are unknown. Therefore, the requirements concerning the cutting of the vitreous are set by the target specification of the vitreous cutter from DORC. The driving mechanism should generate a reciprocating translation movement with a stroke length of 0.8 mm (R-cut.1). In this way, the new driving mechanism can be combined with the current 8268.VIT23 needles. The outer needle will be attached to the housing and the inner needle to the driving mechanism. With a stroke length of 0.8 mm, the cutting port from the inner needle completely bypasses the cutting port of the outer needle such that the vitreous is cut. To cut the vitreous, a force of 9N in the forward direction must be generated during the forward motion (R-cut.2) and a force of 8N must be generated in the backward direction during the backward motion (R-cut.3).

The driving mechanism must perform the forward motion within 0.0037 seconds (R-cut.4), and the driving mechanism must perform the backward motion within 0.0037 seconds (R-cut.5). These speeds are derived from the target specifications, where a maximum cutting frequency of 16000 cuts per minute is stated. A high cut-rate increases the flow rate, limits the traction on the retina and decreased the surgery time. Therefore, the maximal frequency of a vitreous cutter is a crucial factor for competitors in the vitreous cutter market. To offer a valuable addition to the current field of vitrectomy, the device should most ideally work at a similar frequency as currently sold devices. Due to the two-dimensional cutting needles, the driving mechanism should reciprocate at a maximum frequency of 8000 strokes per minute

Both the forward and backward motion must be performed at high speed to limit the traction on the retina. However, during vitrectomy, the cut frequency is varied for optimal operation. Hence, the driving mechanism should allow changing the frequency while the cut speed remains constant (R-cut.6). During a long vitrectomy procedure, the core vitrectomy procedure, where the central vitreous is removed, takes approximately ten minutes and works at around 10.000 cuts per minute. The retinal shaving step takes around five minutes at the maximal cut rate of 16000 cuts per minute. Overall, with the two-dimensional cutting cycle, the device should have a minimal lifetime of 90.000 cycles (R-cut.7) to guarantee the working of the device during the whole vitrectomy procedure.

Grab separated vitreous and transport vitreous out of the eye

After cutting the vitreous, the small vitreous pieces must be transported out of the eye. To minimize the harm to the patient, the transport should preferably be through the same hole as the access hole. This is best done by applying a vacuum to the hollow needles. To make the device compatible with the EVA pressure supply system, the device must allow for a vacuum inside the inner needle ranging from atmospheric pressure up to 0.13 bar (R-GRAP.1). After transporting the vitreous out of the eye the vitreous should be further disposed. Therefore, there must be provided a passage for the vitreous through the device (R-GRAP.2).

Table 1
Design requirements

R.1	leading	The driving mechanism must be made by AM without requiring post assembling steps of trained technicians.
R.2	leading	The driving mechanism must be powered by pressurized air.
R.3	wish	The device have to be compatible with the EVA system.
Access vitreous		
R-access.1	leading	It must be possible to attach a 0.32 mm diameter inner needle to the driving mechanism during or after printing.
R-access.2	wish	The device should preferably be sterilizable and biocompatible.
Position the device		
R-position.1	leading	The handle of the device must have a maximal diameter of 16mm.
R-position.2	leading	The handle of the device must have a maximal length of 190 mm.
R-position.3	wish	The device should preferably weigh less than 5 gram.
Cut vitreous		
R-cut.1	leading	The driving mechanism must generate a reciprocating translation movement with a stroke length of 0.8 mm.
R-cut.2	leading	A force of 9N in the forward direction must be generated during the forward motion.
R-cut.3	leading	A force of 8N must be generated in the backward direction during the backward motion.
R-cut.4	leading	The driving mechanism must perform the forward motion within 0.0037 seconds.
R-cut.5	leading	The driving mechanism must perform the backward motion within 0.0037 seconds.
R-cut.6	wish	The driving mechanism should allow changing the frequency while the cut speed remains constant.
R-cut.7	wish	The device should have a lifetime of minimum 90.000 cycles.
Grab vitreous pieces and transport out of the eye		
R.grab.1	leading	The device must allow for a vacuum inside the inner needle ranging from atmospheric pressure up to 0.13 bar.
R.grab.2	leading	There must be provided a passage for the vitreous through the device.

3 PNEUMATIC ACTUATORS

3.1 Introduction

The function analyses and the requirements stated in the previous chapter limit the design field to pneumatic devices. However, there exists a wide range of pneumatic devices. Research on the currently used pneumatic actuators is executed to explore the potential design directions. Pneumatic devices can be either linear actuators or rotating actuators. To drive the vitrectomy needle according to the stated requirements, the final output of the driving mechanism should be translating and reciprocating. Therefore, rotary actors should be combined with a conversion mechanism like a cam follower, screw, slider-crank or rack and pinion to convert the motion. Overall, both linear and rotary actuators can be considered as potential design directions. The potential design directions as indicated in Fig. 8 will be discussed in the next sections.

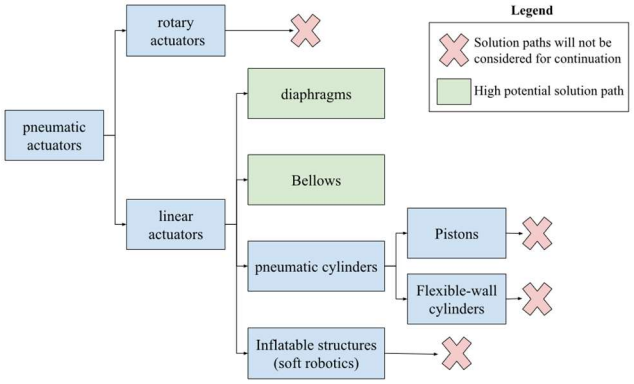

Fig. 8. Overview potential design directions for a pneumatic driving mechanism of a reciprocating needle

3.2 Rotary actuators

3.2.1 Potential design directions

For the rotary actuators, multiple designs can be found. In general, four main rotary motor types exist: vane, piston, turbine, or gear motor. Since airtight sealing is hard to 3D Print without post assembling steps, the turbine and gear pneumatic motor might form a potential design direction due to the minor importance of sealing. However, there is still a huge possible variety for the exact design within these major groups. Examples of rotary actuators used in similar applications might form a good starting point for designing a pneumatic rotary motor actuating a vitreous cutter. For example, the dental drill is a generally well-known handheld medical device working with a pneumatic turbine. The relatively small turbine is actuated by compressed air in the radial direction, as depicted in Fig. 9.

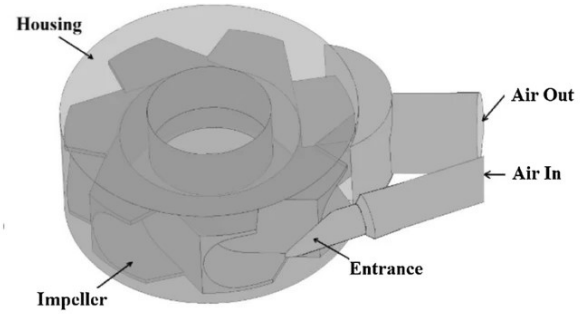

Fig. 9. 3D-model of a pneumatic rotary actuator used in a dental drill, example of a generally well-known handheld medical device working with a pneumatic turbine (taken from [22])

Another device with a similar application as a vitreous cutter is a tattooing machine. The design of a vitreous cutter can for example be based on the device as described in the patent by Carson F. Hill [23]. The working can be seen in Fig. 10. The compressed air blows against the turbine (30) in the radial direction. The came lobe (34) attached to the turbine transfers the rotation to a reciprocating translation by pushing against the side wall of a rectangular hole (36). This example only illustrates one example of a radial actuator with an additional conversion mechanism to show the potential of this design direction.

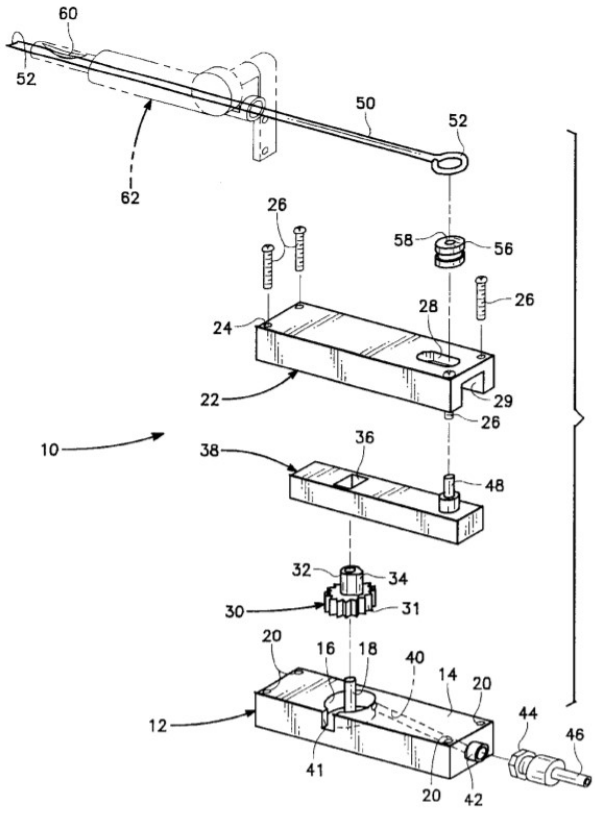

Fig. 10. Tattooing machine actuated by air turbine, example of a device with a similar application as a vitreous cutter (taken from [23])

3.2.2 Feasibility of design directions

In contrast to all other solutions paths, Rotary actuators do not require flexible materials. This might be beneficial for the lifetime and cut rates can be easily increased by increasing the pressure. To give an indication, the dentist drill can obtain speeds up to 500 000 rotation per minute [24]. For each turbine, a specific curve exists, drawing the relation between the speed and torque. At relatively high speeds, the torque decreases with increasing speed. Since the vitreous cutter should be optimized for 8000 rpm while maintaining an output force of 8N, finding the optimum design to fulfil the speed and torque requirement might be challenging. A selection should be made out of a wide range of possible turbine designs. As described, designs with similar applications like a dentist drill or tattooing machine can form a good starting point but still need to be optimized to fulfil the exact requirements, which can be time-consuming.

Moreover, the turbine design should be translated to a non-assembly 3D Printable design. Since a rotor should freely move within a housing, a small space between these elements has to be maintained. Soluble support structures might form an outcome, but no direct guarantee for success can be made since removing the support from these small spaces might be challenging. In the limited amount of non-assembly 3D Printed rotary actuators found in literature, this problem is solved by printing a liquid oil layer [25] or co-printing of solids and liquids [26] such that the rotor can be easily separated after printing. However, it is preferred to first explore design solutions where conventional 3D Printers can be used. Wei et al. [14] attempted to solve the problem and concluded that an open fan turbine could allow easy support removal. However, it is unwanted to use a device where compressed air is freely released, to prevent harm to the patient.

Also, the high rotation speed might cause problems concerning wear. Another drawback is the dependence of the cut speed on the frequency (R-cut.6). Different cutting frequencies are used during a vitrectomy procedure, which is easily allowed by applying different pressure levels on the turbine. However, when working at lower frequencies, a minimal cut speed should still be maintained to cut the vitreous. In the case of a direct coupling between the turbine and cutting needles, the cut speed will always be dependent on the frequency. Additionally, the needles cannot be easily stopped, which is required for safety reasons and easy control. Overall, rotating actuators are not considered for the continuation of this study due to multiple drawbacks mentioned in the section above.

3.3 Linear actuators

3.3.1 Potential design directions

The conventional translating actuators can be divided into diaphragms, bellows and pneumatic cylinders [27]. An example of a 3D Printed diaphragm is depicted in Fig.11. When pressurizing the air chamber the flexible diaphragm will extend. A few examples of 3D Printed diaphragms can already be found in the literature [28]–[32]. Diaphragm actuators form the basis of the state-of-the-art 3D Printed vitreous cutter driving mechanisms and will be further elaborated on in the next chapter. The bellows might form an interesting potential design direction. Already multiple examples of 3D Printed bellows can be found in the literature [26], [33]–[36]. An example of a 3D Printed bellow is depicted in Bellows can either be extended by positive pressure or compressed by negative pressure.

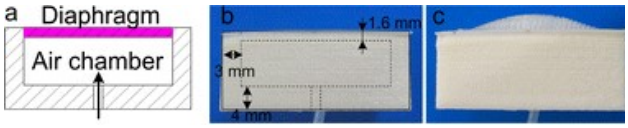

(a) (b) (c)

Fig. 11. Printed pneumatic diaphragm (a) schematic drawing (b) diaphragm at rest (c) pressurized diaphragm (Taken from [28])

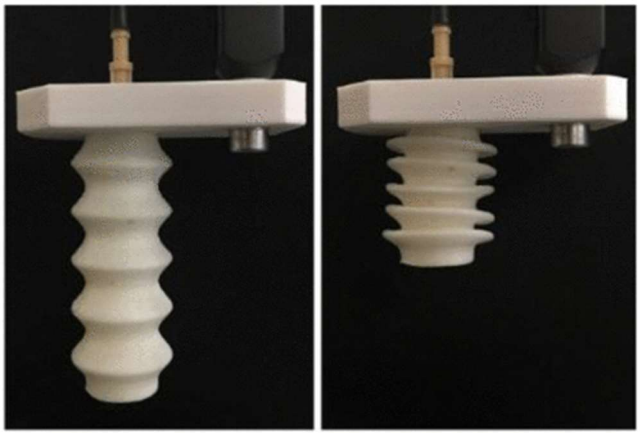

(a) (b)

Fig. 12. Bellow manufactured with FDM (a) bellow at rest (b) bellow compressed by negative pressure. (taken from [36])

Also, the pneumatic cylinders can be considered a potential design direction. Conventional pneumatic cylinders move a piston forward by pressurized air. Special care is needed for the sealing around the piston, making the actuator hard to print without any post assembling steps. However, a rolling diaphragm piston and flexible chamber piston can offer an alternative to the conventional sealing rings around the piston [27]. In Fig. 13 a schematic drawing of such a flexible chamber piston is shown. The two flexible chambers (2) and (4) can be pressurized to actuate the piston (7). The folds in the

sealing around the chambers allow altering the chamber size without air leakage. A rolling diaphragm is based on the same principle and has sealing folds located directly next to the piston head.

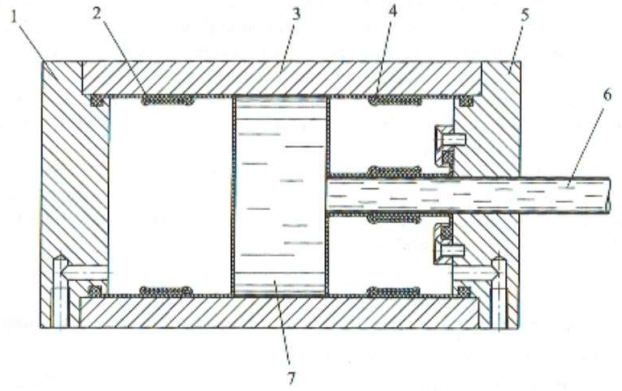

Fig. 13. Schematic drawing of flexible chamber piston (Taken from [27])

Another option is the flexible-wall cylinder, like the pneumatic muscle or so-called McKibben actuator. This actuator consists of an elastic tube with reinforced fibres to limit the strain. When pressure is applied, the elastic tube expands and hence pushes the reinforced fibres outward, making the muscle shorter. As a result, a linear motion and additional force can be generated as also seen in the silicone 3D Printed muscle depicted in *Fig. 14*. McKibben's muscle is only one example of an artificial muscle. Zhang et al. l [37] describe the wide range of artificial muscles. In the field of soft robotics, multiple kinds of artificial muscles can be found based on the principle of inflatable structures consisting of elastic and non-elastic parts.

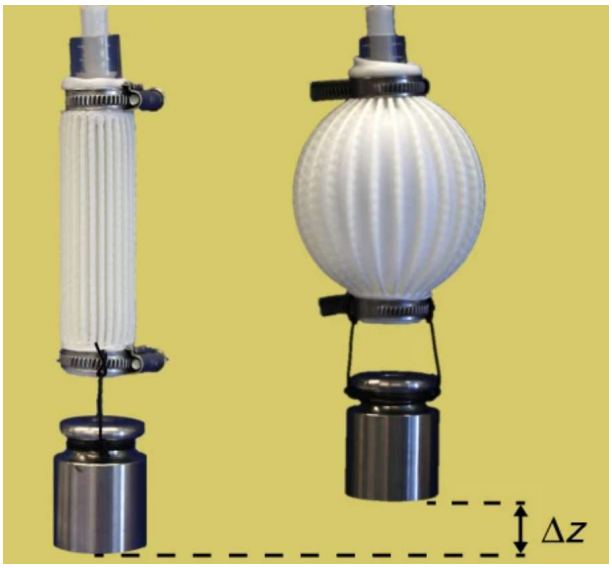

Fig. 14. McKibben muscle fabricated by multi-material 3D Printing of silicones, depicted at rest and after applied pressure (taken from [38]*)*

The field of soft robotics might offer more insight into potential design directions aside from the conventional pneumatic actuators. Multiple review papers [35], [39]–[41] on inflatable actuators for soft robotics already highlight the potential of this field. Actuators similar to the conventional actuators like the bellow, diaphragm and McKibben can be found but also slightly different actuators like for example depicted in Fig. 15. By designing the compartments of inflatable structures in specific ways different actuator types can be made. Especially interesting is that these soft robotics are currently already made by additive manufacturing in some cases [43]. Overall, elastic inflatable structures such as those used in the field of soft robotics might form a potential design direction.

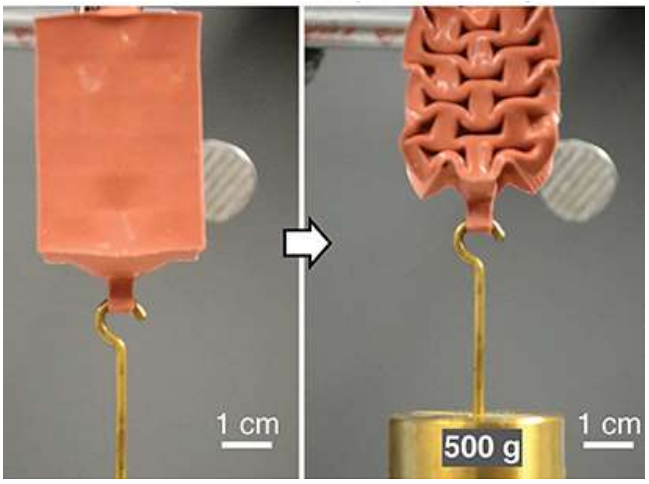

(a) *(b)*

Fig. 15. Soft robotic actuators (a) at rest (b) shortened by applied negative pressure (taken from [42] *)*

3.3.2 Feasibility of design directions

The above-stated pneumatic actuators might form a potential design direction. However, the question is how feasible it is to meet all the requirements and make a vitreous cutter driving mechanism design suitable for 3D Printing. Multiple examples of 3D Printed linear actuators can already be found in literature concerning soft robotics. Currently, soft robotics is a hot literature topic, a prelude to the prominent role the devices might fulfil in the future [40]. Hence, these actuators might also form an outcome in the field of vitrectomy. Especially the elastic inflatable actuators might be a beneficial solution path. These devices are preferred due to their safety, energy efficiency, low cost and the high output force that can be obtained [37]. In the medical field, the safety of the actuators is an important benefit [40]. Compared to the diaphragm design, the considered linear actuators take more advantage of the available space in the longitudinal direction. However, even though there is

currently a lot of research in the field of soft robotics, soft robotics is still in its infancy [41], [43].

Especially the longevity (R-cut.7) of 3D Printed soft robotic actuators is a major concern. 3D Printed material can easily break due to the low tensile strength and the silicones that are often used due to their flexibility and producibility have a negative effect on the lifetime [44]. Consequently, soft robotics with a sufficiently high lifetime could not be found in the literature. As a result, inflatable structures dependent on high material strain are considered an unsuitable design direction. Moreover, the limitations of 3D Printing material do not allow for designs based on a rolling diaphragm. The design's high material strain and fatigue are significant problems [26]. When more materials are available in the future, a rolling diaphragm might be especially beneficial since this design does not require sliding seals or high stretchable structures. Therefore, the described rolling diaphragm piston and flexible chamber piston might be a beneficial design direction in the future but are currently not possible within the limitations of 3D Printing.

Also for the McKibben artificial muscle, multiple drawbacks are found. The braided design of the outer sleeve causes a high hysteresis due to the friction with the inner tube [37]. Moreover, the design exhibits non-linear behaviour, and no force is generated during return (R-cut.3). Hence the McKibben actuator can not directly be connected to the conventional pressure supply system (R.3). The 3D Printed example found in literature requires special 3D Printing techniques and materials [38]. With state-of-the-art available materials and 3D Printing processes, the material strain might still be a problem for the lifetime of McKibben actuators (R-cut.7).

In contrast, the bellow actuators exhibit relatively less material strain due to the unfolding design, which is not solely dependent on the material strain to generate motion [37]. The unfolding design requires a smaller volume change and hence exhibits lower material strains, which positively affects the lifetime and allows for faster actuation [43]. Even though the lifetime is still a concern, some examples of 3D Printed bellows with a relatively high lifetime can be found in the literature. Tawk et al. [36] optimized a bellow to obtain 80,000 actuation cycles before failure. During the corona pandemic, the urgent need for a bellow that could be used in medical ventilators encouraged the development of a fusion jet printed design made from TPU that was tested up to 1.5 million cycles [45]. Overall, the bellow might form a potential design direction for developing a 3D Printable vitreous cutter.

4 DUAL FLAT DIAPHRAGM ACTUATOR

4.1 Prior attempt to 3D print a vitreous cutter

Aside from researching pneumatic actuators to find potential design directions, previous attempts to make a 3D Printable vitreous cutter might also form a valuable design direction for a redesign. Only one attempt to make a non-assembly vitreous cutter is known by the author. Stolk et al [15] made the first prototypes of a dual flat diaphragm driving mechanism design suitable for 3D PolyJet printing. The schematic cross-section in Fig. 16 shows an embodiment of the device they had in mind. Considerable similarities exist with the working principle of the vitreous cutter from DORC, as described in the state-of-the-art section.

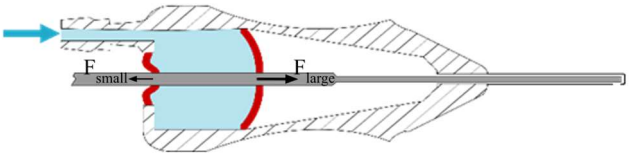

Fig. 16. Schematic cross-section showing an embodiment of the dual flat diaphragm driving mechanism design suitable for 3D PolyJet printing.

The working principle of the forward motion of the inner needle can be explained by means of Fig. 16. Pressurized air enters the device at the blue arrow to increase the pressure inside the chamber indicated in blue. The pressurized chamber is sealed by a small and a large flexible diaphragm indicated in red. Due to the increased pressure, both diaphragms tend to move outwards while exerting a force in the outward direction. Since the inner needle is attached at the centre of both diaphragms, the total force and displacement of the inner needle can be described by the sum of both the large and small diaphragms. As a larger diaphragm surface results in a larger force, the resultant force and displacement on the inner needle act in the forward direction. When the pressure is released, the spring force of the diaphragms moves the inner needle back to the initial position while exerting a force in the backward direction.

To test the concept of a dual flat diaphragm driving mechanism Stolk et al. [15] made prototypes like depicted in Fig. 17. By using soluble support material, the prototypes could be directly 3D PolyJet printed and required only one post assembly step where the cleaning hole was closed. Because the stiffness of the diaphragm plays a crucial role in the working of the device, multiple prototypes of different diaphragm materials were obtained and tested on the set requirements. Since Polyjet only allows for a limited amount of standard materials, where the exact material properties are unknown, material mixtures of Vero and Agilus30 were used. Vero is relatively stiff and Agilus30 relatively flexible.

Therefore, mixtures with a low percentage Vero are relatively flexible and mixtures with a high percentage Vero are relatively stiff. Multiple ratios are tested to find the most suitable material.

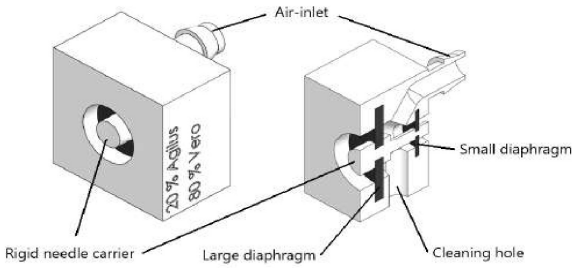

Fig. 17. 3D model of dual flat diaphragm driving mechanism prototype. (Taken from [15])

Tests of the prototypes showed a high potential of the device. Table II displays the test results of the prototypes that underwent both a force-displacement and a pressure-displacement test. The prototypes could reach the minimal displacement (R-cut.1) and the minimal force at the start point of the backward motion (R-cut.3), as depicted in the third and fourth row of Table II respectively. However, the force during the backward motion was only high enough for the stiffest sample. The main limitation of the prototype was the relatively slow speed of the backward motion but the required speed during forward motion could also not be obtained. The forward speed is displayed by the time required to move 0.8 mm forward and stated in the fifth row of Table II. The backward speed is determined by the time needed to move 0.8 mm backwards from the maximum displacement, as displayed in the last row of Table II. The time required to move the last 0.8 mm back to the initial position was even longer and lied between 5.59 and 73.3 seconds. Overall, a design that met all previously stated requirements could not yet be obtained.

Table 2
Test results prior attempt 3D Printed dual flat diaphragm actuator

	50Agilus3050Vero	80Agilus3020Vero	20Agilus3080Vero-2.1	50Agilus3050Vero-2.1	80Agilus3020Vero-2.1
Percentage Agilus30	50%	80%	20%	50%	80%
Percentage Vero	50%	20%	80%	50%	20%
Max displacement	2.00 [mm]	1.83 [mm]	1.49 [mm]	1.85 [mm]	1.76 [mm]
Force at 0.8 mm displacement	3.89 [N]	3.14 [N]	9.82 [N]	4.04 [N]	3.53 [N]
Time to move 0.8 mm forward	0.175 [sec]	0.183 [sec]	0.567 [sec]	0.156 [sec]	0.11 [sec]
Time to move 0.8 mm backward	0.258 [sec]	0.326 [sec]	1.483 [sec]	0.180 [sec]	0.134 [sec]

4.2 Theoretical working principle dual flat diaphragm actuator

Stolk et al [15] used the formulas below to approximate the overall theoretical working of the dual flat diaphragm. The formulas are based on the theory of a rigid centre diaphragm [27], [46] with an outer diameter (D_o) and rigid centre diameter (D_i). The formulas apply under the condition that the diaphragm thickness is than the diaphragm displacement [27]and larger than 20% of the outer diameter of the diaphragm [46]. Additionally the material should act as a linear elastic material. During the forward motion, the force is generated by pressure. Due to the increased pressure, both diaphragms tend to move outwards while exerting a force in the outward direction. These forces, indicated by black arrows in Fig. 16, can be described by the pressure difference (ΔP) times the effective area of each diaphragm (A_{eff}), see equation (1). The effective area of each diaphragm can be calculated by equation (2). Since the inner needle connects both diaphragms the resultant force in the forward direction can be described by the difference in the force generated by the large diaphragm (F_{large}) and the force generated by the small diaphragm (F_{small}), see equation (4). When applying pressure, the resultant force acts in the forward direction. Due to the larger diameter, the large diaphragm generates a relatively larger force.

The backward motion and backward force are caused by the stiffness (k) of the diaphragms. Each stiffness can be described by equation (5) and is dependent on the thickness (T), outer diameter (D_o), rigid centre diameter (D_i), elastic modules (E) and Poisson's ratio (μ). The two diaphragms can be seen as two springs working in parallel since the diaphragms are rigidly connected and have an equal displacement. Therefore the overall backward force can be described as the sum of the stiffness of the large diaphragm (k_{large}) and stiffness of the small diaphragm (k_{small}) times the displacement (s), see equation (6).

$$F_{diaphragh} = \Delta P * A_{eff} \quad (1)$$

$$A_{eff} = \frac{4D_o^2 * (\frac{n^2-1}{4n^2} - \frac{\ln(n)^2}{n^2-1})}{1-n^{-4}-4n^{-2} * \ln(n)} \quad (2)$$

$$n = \frac{D_o}{D_i} \quad (3)$$

$$F_{forward} = F_{large} - F_{small} \quad (4)$$

$$k_{diaphraghm} = \frac{16\pi * E * T^3 * n^2 * (n^2-1)}{3 * D_o^2 * (1-\mu^2) * ((n^2-1) - 4n^2 * \ln(n)^2)} \quad (5)$$

$$F_{backward} = s * (k_{large} + k_{small}) \quad (6)$$

4.3 Function analysis for redesigning

A function analysis diagram (FAD) is a useful starting point for adaptive and variant design [47]. A FAD consists of blocks representing a part of the device, the blocks are connected by arrows representing the functional relationship between the blocks. In Fig. 18 a FAD applicable to the dual flat diaphragm driving mechanism design can be seen. The dual flat diaphragm driving mechanism design can be divided into eight blocks and three additional blocks for the operator, compressed air and the vitreous. The air inlet provides an inlet and outlet port for the compressed air while sealing the air chamber. The inner needle cuts and transports the vitreous out of the eye, whereafter also providing a passage through the device for the vitreous. The outer needle can grab and cut the vitreous. The outer needle is attached to the housing, which houses the device while providing an interface for the operator. On the other hand, the inner needle is attached to the needle carrier while the needle carrier is connected to both the small and large diaphragm.

The small and large diaphragm serve multiple functions and show a lot of functional relationships. Both diaphragms seal the air chamber and align the needle carrier at the central position while allowing a passage for the inner needle. On the one hand, the large diaphragm moves forward and exerts a forward force due to the compressed air. On the other hand, the small diaphragm moves backwards and exerts a backward force due to the compressed air. Since both diaphragms are attached to the needle carrier the resultant force and movement are exerted on the needle carrier. The needle carrier moves forward when the air chamber is pressurized due to the relatively higher force on the large diaphragm. The forward motion is limited due to the pressure on the small diaphragm and due to the stiffness of both diaphragms, causing a force in the backward direction. If the pressure is released, the needle carrier moves back to the initial position due to the resultant force in the backward direction caused by the spring stiffness of both diaphragms.

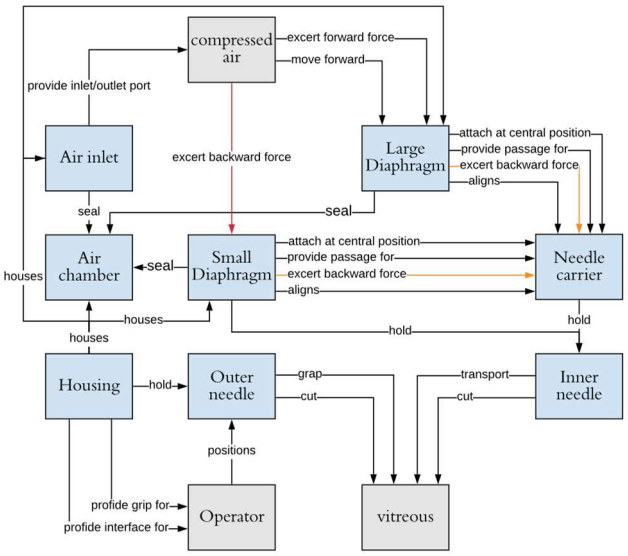

Fig. 18. Function analysis diagram of the dual flat diaphragm driving mechanism design

4.4 Mass-spring-damper model

The mass-spring-damper model, as visualized in Fig. 19, can describe the dual flat diaphragm driving mechanism in a more comprehensive abstract way. Since the spring-mass-damper system is a well-studied problem, the model allows for easy insight into the cooperation of different forces acting on the system. The diaphragm can be defined by a spring with a spring constant k. More specifically, the spring symbolizes the resultant spring constant of the small and large diaphragm working in parallel. The model simplifies the system's mass to a single point mass attached to the spring. In an ideal case, the system could be solely described by this spring and mass. When giving the mass an initial displacement, the system will keep vibrating infinitely according to newtons laws.

However, this theoretical case does not include any energy losses, which is unrealistic. Therefore, a damper with damping coefficient c, is added to the system, modelling all the potential energy losses. In general, this can contain viscous damping, coulomb/dry friction damping, material or hysteretic damping and magnetic damping. A driving force is used to still provide a continuous reciprocating motion of the vitreous cutter. The driving force puts energy lost due to damping back into the system. Because the driving force only acts during forward motion, the force is modelled as a time-dependent force F(t). This force represents the resultant force caused by the applied pressure on both diaphragms.

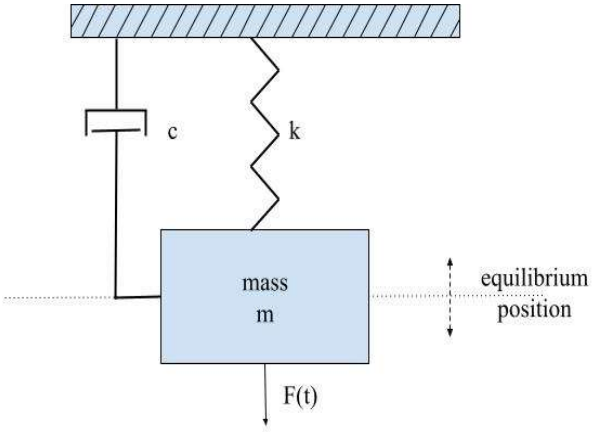

Fig. 19. mass-spring-damper model

With the defined model parameters the damping ratio ζ can be described by equation (7). The damping ratio is a dimensionless parameter that indicates the oscillation decay of the system, giving insight into how fast the spring returns or passes the equilibrium position. A damping ratio smaller than one results in a sinusoidal-shaped graph decaying over time. This so-called underdamped system passes the equilibrium position and oscillates until completely damped and returned to the equilibrium position. An overdamped system, in the contrary, has a damping ratio larger than one and moves slowly back to the equilibrium position without oscillating, like visualized in Fig. 20. The time displacements graph resulting from the prototype tests by Stolk et al [15] indicates the overdamped nature of the current dual flat diaphragm design. Overall, the smaller the damping ratio, the faster the equilibrium position will be passed for the first time, like seen in Fig. 20.

$$\zeta = \sqrt{\frac{c^2}{4\,m\,k}} \qquad (7)$$

As a result, decreasing the damping ratio corresponds to decreasing the time required for the backward motion of the dual flat diaphragm design. Since this is the main area of attention for improving the dual flat diaphragm design, the damping ratio can indicate the main ways to improve the design. Decreasing the damping ratio can be done by increasing the spring stiffness, decreasing the damping coefficient, and increasing the mass. However, increasing the mass is not a preferred solution path since it is preferred to make a lightweight device. Another potential point of improvement is adding a force actuating the spring in the backward direction during backward motion. Adding a driving force, increasing the spring constant and reducing the spring constant will be further elaborated on in the next section for potential points of improvement.

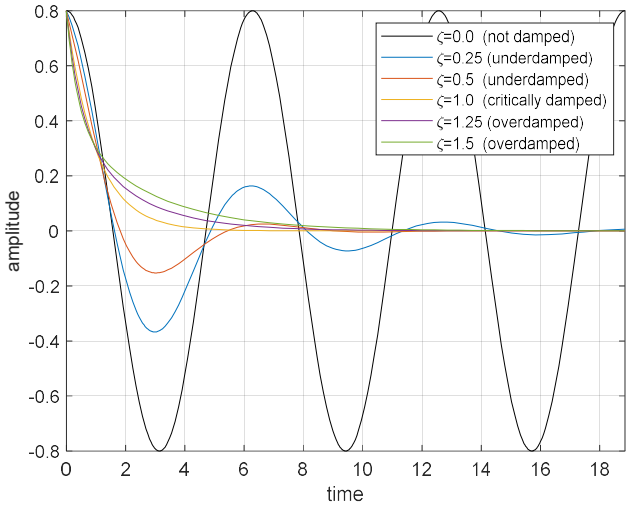

Fig. 20 Visualization of example responses with different damping ratios

4.5 Improving the dual flat diaphragm design

4.5.1 Adding a driving force

The speed in the backward direction can be increased by adding an additional force in the backward direction. The required function of storing energy for the backward motion and enclosing the air chamber are separated by adding an additional force to the dual flat diaphragm design. The diaphragm can be optimized to seal and allow the forward motion and additional force. Accordingly, less emphasis is on balancing the optimal material that requires both flexible and stiff properties at once. Moreover, the need for material mixtures with a potentially negative effect on the hysteresis can be reduced.

In general, forces can be generated by: magnetism, Coulomb interaction, gravitation, elasticity, impact, muscular power, pressure difference, thrust, buoyancy or nuclear power. However, not all possible ways to generate a force are equally suitable. For example, gravitation is unsuitable since the device must work in all orientations and should be kept lightweight. As noted earlier, a complete pneumatic device compatible with the EVA pressure supply system is preferable. A pressure difference can either be generated by applying under pressure in the current air chamber or by applying an overpressure on the opposite site of the diaphragm. This concept can be embodied by enclosing the room in front of the diaphragm and applying pressure to the chamber.

In the ideal case, the backward force is only present during the backward motion, which could be represented by a time-dependent driving force in the mass-spring-damper model. The timing of a time-dependent backward force is essential but rather difficult to control at high frequencies. However, dual pneumatic vitreous cutters where an overpressure is alternated between the front and

backside of the diaphragm are currently already on the market [48]. Hence, the required control systems for regulating pressure already exist and can be used. However, it is preferred to first explore the possibilities within the capabilities of DORC and the accompanying EVA pressure supply system, like also described in the stated wishes.

Overall, it is preferred to first explore solutions of lower device complexity. Hence, alternating the pressure is not the preferred solution path but can still offer an outcome when simplistic solutions are unsuitable. Moreover, solely adding a driving force for the backward motion while the damping is still relatively high, requires a rather large driving force to still obtain a significant change in the speed of the backward motion. It would be ideal if the diaphragm could vastly return to its initial position without additional actuation forces.

4.5.2 Increasing the spring constant

The spring constant in the spring-mass-damper model corresponds to the stiffness of the diaphragms. On the one hand, stiffness of the diaphragm is required to obtain a spring force high enough to move the needle back to the initial position at the preferred speed while still exerting a force during the backward motion to cut the vitreous. On the other hand, a flexible diaphragm is preferred to not limit the forward motion and hence reduce the required pressure. Hence, there are contradicting requirements on the design parameters. From the theoretical working principle, it can be seen that the design parameters are limited to the outer diameter (D_o), rigid centre diameter (D_i), thickness (T) and materials properties like the e modules (E) and poisons ratio (μ). The stiffness of the diaphragm can be increased by decreasing the outer diameter, increasing the thickness and the stiffness of the material which is associated with the E modules.

Schuurman et al. [49] started with the optimization process of the design parameters for the dual flat diaphragm design. Since the design parameters all influence each other, Schuurman et al. [49] made an optimization model. Assuming that the stiffer diaphragm moves back faster to its original position, the model aims to maximize the stiffness of the large diaphragm and minimize the force during the pressurized air pulse for the small diaphragm. However, the prototypes with mixtures of Vero and Agilus3030 showed return times contradictory to this theory. Moreover, the formulas on which the optimization model is based do not seem to match reality. Schuurman et al. [49] tested multiple samples of Vero and Agilus30 mixtures on the mechanical properties since these are not precisely known. When coupling the founded E modules back to the formulas (1)-(6) it can be seen that the theoretical backward force does not match the test results from Stolk et al [15]. Conclusively, solely optimizing the diaphragm to obtain a higher spring constant does not seem a valuable solution.

Instead of only optimizing the current design, the spring constant might also be increased by adding an additional spring to the system. In this way, the diaphragm can be optimized for sealing purposes while the spring on the contrary can be optimized to store energy for the backward motion and hold the needle in the central position. The additional spring can be mainly based on a flexible material like the diaphragm but can also be a mechanical spring more based on a shape deformation. The stiffness of a mechanical spring can be altered in a wide range without changing the material. Therefore, a spring offers more design properties to optimize for.

4.5.3 Reducing the damping coefficient

Since the system appears overdamped, reducing the damping coefficient is an important aspect of increasing the return speed. Small improvements might already result in a beneficial effect, considering that the damping coefficient is to the power two, according to equation (7). The diaphragm can be optimized such that the forces in the backward direction are increased while the forces in unwanted directions, like friction forces and internal friction forces, are decreased. Hysteresis is associated with the energy loss due to internal friction forces, a material dependent parameter. From the force displacements graph of Stolk et al. [15] it can be seen that hysteresis might play a large role. Since the hysteresis and stiffness are both dependent on the material, a high emphasis is on the material selection of the diaphragm to increase the return speed.

In the previous dual flat diaphragm design, material mixtures of Agilus3030 and Vero were used to vary the mechanical properties in the desired range. However, mixtures of Vero and Agilus3030 showed unexpected hysteresis behaviour. Materials with a low percentage Vero are relatively flexible and hence are expected to have a higher hysteresis. On the contrary, flexible rubber-like materials always exert relatively more hysteresis and hence are expected to have a lower hysteresis. Both the research of Schuurman et al. [49] and Stolk et al. [15] show results contradicting this theory, relatively flexible mixture with a low percentage Vero show a lower hysteresis than stiffer mixtures. This contradicting result probably caused a relatively low return speed. Hence, optimising the percentage Vero and Agilus3030 does not seem to offer a valuable solution.

On the contrary, other materials might reduce the hysteresis while still offering sufficient stiffness. Aside from selecting an optimal material for the entire large diaphragm, the material can also be optimized per part to reduce energy losses. Polyjet printing allows altering the material properties per pixel by using material mixtures [50]. However, the diaphragm always needs to be relatively flexible to obtain the desired range of motion and hence hysteresis is inevitable for the dual flat diaphragm design.

Instead of altering the material, the shape can be improved such that less emphasis is on the extension by material strain and more on extension due to shape deformation. As a result, there is also less emphasis on selecting the optimal material, which is crucial since the materials available for multi-material PolyJet printing are limited. Contrary to material optimization, optimizing the shape might offer more possibilities. Multiple diaphragm shapes are already in use [51], showing the range of possibilities that might form an improvement to the flat diaphragm. For example, adding convolutions to the diaphragm allows for a rolling or bending movement instead of pure stretching of the material itself. Like also seen in the pneumatic valve diaphragm design obtained by an optimization process by Javorik et al [52] and depicted in Fig. 21. Another well-known diaphragm shape is the corrugated diaphragm. The corrugations allow for a relatively larger stroke length while using stiffer materials.

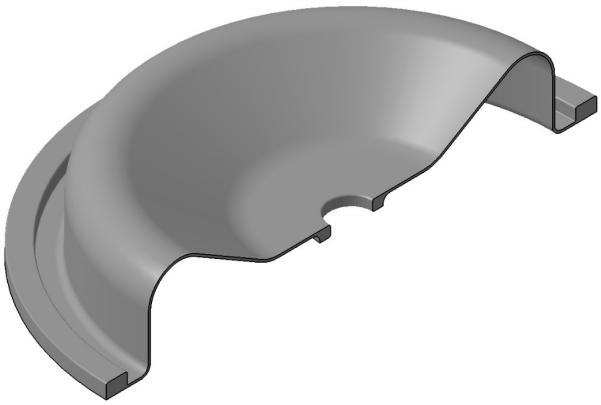

Fig. 21. Cross section of diaphragm shape optimized for pneumatic valve (taken from [52])

However, the design freedom of the diaphragm shape is limited due to the minimal thickness for 3D Printing and the additional size requirements of to the small vitreous cutter handle, leaving only a few mm extra for additional shapes like a corrugation. On the contrary, more space might be used when designing a flexible structure in the longitudinal direction. The bellow design can be considered a longitudinal version of the corrugated diaphragm, where more corrugations can be added while still fulfilling the dimensional requirements. The bellow can allow a sufficient motion range by adding multiple corrugations even though the bellow material is relatively stiff. To give an indication, bellows are often even made out of metals. Reducing the need for flexible material can reduce the hysteresis. Hence, bellows, as discussed under the linear actuator section, might offer a better solution than a shape optimization of the diaphragm.

With the same reasoning adding a spring to the dual flat diaphragm design might reduce the hysteresis. Springs can be made of stiff material while still allowing motion since springs are not solely dependent on material strain but also on shape deformation. Springs are expected to benefit from a lower hysteresis compared to flexible material since less internal material friction is expected. In this way, the diaphragm can be optimized for sealing purposes only, and the spring can exhibit the backward motion. In conclusion, adding a spring appears to be a beneficial design direction since a spring can both increase the spring stiffness and reduce the damping coefficient of the mass-spring-damper model. Overall, both a spring-reinforced dual flat diaphragm design and a bellow will be considered for further design as described in the next section.

5 SPRING REINFORCED DUAL FLAT DRIVING MECHANISM DESIGN

5.1 Selection design direction

Both the spring-reinforced dual flat diaphragm concept and the bellow-driven concept can over an outcome. One attempt for The dual-diaphragm concept is already printed by Stolk et al [15]. Support material could be removed and the device was airtight. A 3D printed bellow driven vitreous cutter design on the other hand is not presented beforehand. A first attempt of the bellow is printed with the printer settings reported by Tawk et al [36]. Multiple failures occurred during FDM printing. It appeared the printer settings still needed to be adapted since warpage occurred and small holes were visible in the structure making it not airtight. Moreover, it appeared support was needed during the printing process. However, it is unknown how feasible easy support removal is due to the small size, corrugations and limited space for support removal holes. Overall, it is decided to first proceed with the spring-reinforced dual flat diaphragm driving mechanism design since no direct advantage of a bellow in comparison with the spring-reinforced diaphragm can be found. To specify a potential spring reinforced diaphragm design a spring configuration, AM material, AM technique and spring

shape are selected, as discussed in the next section. For the bellow concept, the first steps towards a potential design are discussed in Appendix I.

5.2 Spring configuration

To specify the spring-reinforced dual flat diaphragm design, the general spring type and configuration need to be selected. There exist a wide variety of 3D Printable spring designs that can be categorized into three main categories: line structure, a planar structure and 3D structure [53]. In contrast to the other spring types, the planar structure can be directly combined with the diaphragm which is expected to be beneficial. First of all, the required space can be reduced by directly combining the planar spring with the diaphragm. Secondly, the planar spring limits the diaphragm from excessive deformations which can cause rupture. In contrast, if for example a helical spring would be attached to the needle, the diaphragm will be pushed forward due to the applied pressure while only the centre of the diaphragm is held back by the spring.

The planar spring can be either placed in front of the diaphragm, integrated into the diaphragm or behind the diaphragm, as visualized in Fig. 22. When placing the spring in front of the diaphragm, the air pressure will press directly onto the diaphragm by passing through the gaps in the spring and pushing the diaphragm away from the spring. Therefore, the working of this design is highly dependent on the layer-to-layer adherence between the spring and diaphragm. When directly integrating the spring into the diaphragm, the adherence between the two materials maintains a problem for the gaps of the springs that are filled with diaphragm material. Due to the expected movement between the spring members and the additional air pressure on the gaps, high stresses on the material inside the gap are expected.

On the contrary, layer-to-layer adherence between the spring and diaphragm does not play a crucial role in the configuration of the spring behind the diaphragm. When applying air pressure, the diaphragm will be pushed against the spring and during the backward motion, the spring will push the diaphragm back. This optimal configuration can be further combined by also adding an additional diaphragm behind the spring or material inside the spring gaps. However, no additional benefits are expected when further combining the configurations. Conclusively, the configuration with a planar spring behind the diaphragm is selected for the design.

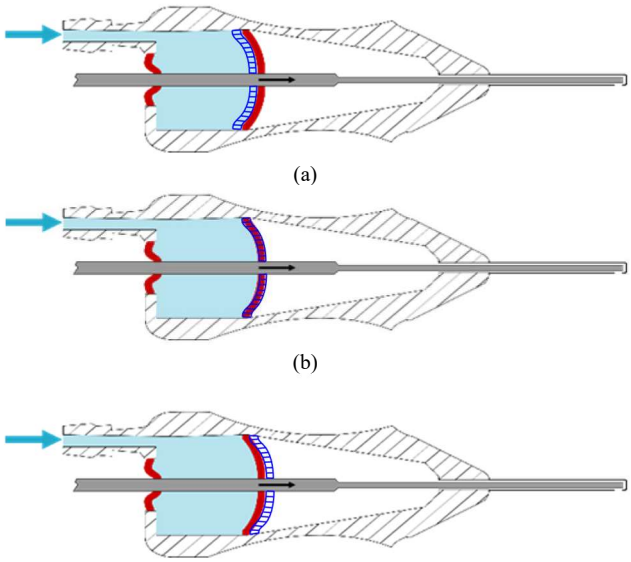

Fig. 22. Graphical image of planar spring configuration witch flexible diaphragm in red and spring dark blue cross-hatched (a) spring in front of diaphragm (b) spring integrated into diaphragm (c) spring behind the diaphragm

5.3 Material and AM technique

The proposed design requires airtight flexible diaphragms. This sets similar requirements for the production technique as elastic inflatable structures which can be made by Stereolithography, PolyJet, selective laser sintering and fused deposition modelling (FDM) [40]. However, the proposed design does not only require flexible materials for the diaphragms but also stiffer materials for the casing and spring. Both FDM and PolyJet are capable of multi-material printing. It is decided to use PolyJet printing. The first prototypes of Stolk et al [15] already showed that an airtight air chamber can be obtained by PolyJet printing and that support could be removed. FDM on the contrary requires an optimization process for the printing parameters of flexible materials such that an airtight structure can be obtained.

The materials for PolyJet printing are limited, for this research there is only access to Vero and Agilus30. Therefore the diaphragms will be made out of Agilius30 and the rigid casing and spring out of Vero. There will not be made use of material mixtures to avoid potential negative effects on the hysteresis. The use of Agilus30 will be minimized such that the backward motion is mainly forced by the Vero spring. Additionally, soluble support material will be used to print the part. Support material is essential during the printing of soft actuators to prevent deformation caused by the own weight of the flexible material [41].

5.4 Spring shape

A spring shape compatible with the dual flat diaphragm design needs to be selected to further specify the design. The centre of the spring should hold the inner needle and allow out-of-plane movement while holding the needle at the central position. Moreover, the spring should exert a force in the backward direction when moving the centre out-of-plane. Meanwhile, the other side of the spring should be connected to the housing keeping the spring in place. This description is perfectly suitable for an ortho-planar spring. An ortho-planar spring consists of an outer base connected by flexible elements to a central platform that can move in the out-of-plane direction. The number and shape of flexible elements can differ. Planar springs can generally be based on two main structural elements: the spiral structure and the zigzag structure [53]. The folded beam can be obtained by mirroring the zigzag structure. Each of the selected springs depicted in Fig. 23 is based on one of these structures such that all general shapes for the flexible members can be tested. The exact dimension of the springs can be found in 0 and will be further elaborated in the description of the prototypes in section 6.1.

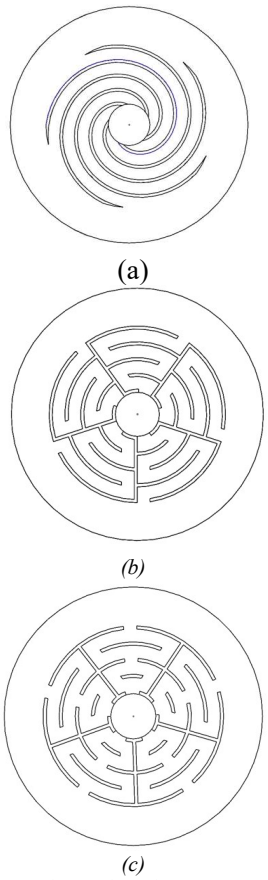

Fig. 23. selected spring shapes based on main structural elements (a) spiral (b) zigzag (c) folded beam

The three specific spring shapes are based on some potentially beneficial design choices. First of all, all three spring designs consist of five flexible elements. An odd number of flexible elements is more stable than a similar even number of flexible elements [54]. Moreover, five flexible elements are considered more stable than three flexible elements, since the corresponding configuration limits twisting of the flexible segments about the central axes [54]. The spring elements of the ortho-planar springs cooperate to hold the central platform in the middle. The zigzag and folded beam based springs are one potential embodiment of a Ortho-planar linear motion springs. The Ortho-planar linear motion springs are designed to restrict the rotation of a central platform with respect to the outer base, while allowing linear out-of-plane axial movement [55].

Secondly, the flexible elements are shaped such that as much diaphragm area is covered as possible. It is expected that springs covering a large part of the diaphragm area are beneficial to prevent the diaphragm from deforming excessively. When applying pressure to a soft sealing diaphragm, it is expected to slightly bend into the gaps of the spring. In Fig. 24 another zigzag-based ortho-planar spring is depicted to easily visualize a design with a relatively low surface covering. It can be imagined that a diaphragm will be pushed into the five triangular gaps, potentially causing the diaphragm to rupture. If the gaps are relatively small, less stress and smaller deformation of the flexible diaphragm are expected. As a result, it is expected that designs covering a larger part of the diaphragm surface could withstand higher pressure pulses and have a relatively higher lifetime. Therefore the gap size in the selected springs is set equal to 0.25 mm, following the minimum required clearance for PolyJet printing.

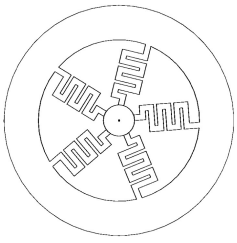

Fig. 24. Zigzag based ortho-planar spring only partly covering the diaphragm

Thirdly, the selected spring shapes are expected to deform similar to the natural diaphragm deformation form. This corresponds with a concave deformation shape where the out-of-plane displacement decreases radially toward the outer edges, and the maximum displacement is at the centre. Since the spring should limit the diaphragm from excessive deformations, it is

expected that springs that deform in a similar shape as the diaphragm are preferred. The exact shape of the zigzag element is considered a minor importance for the stiffness. These can be freely shaped lines or more geometrical shapes like circular, triangular, or the selected rectangular-based zigzag structures. The stiffness of a zigzag spring is mainly dependent on the thickness and amplitude of the zigzag structure [56]. To define the most ideal thickness and corresponding stiffness, tests are required.

5.5 Embodiment vitreous cutter design

To give a first indication of the potential final design a 3D model is shown in Fig. 25. This design serves as a visualization of a potential final product even though multiple embodiments of a design can be argued. Pressurized air can enter the device through the air inlet to push the spring-reinforced diaphragm forward. When the needle carrier is 0.8 mm displaced it will be stopped by a stop plate located inside the handle. The outer needle is attached to the casing and located at the tip of the device. The needles can be glued to the device and allow the transport of vitreous to the outlet. The same outlet and air inlet can be used to remove support out of the air chamber after PolyJet printing. Support can be removed by using water jets with requires two holes. To remove the support out of the front part of the device an additional support removal hole can be used in combination with the hole for the outer needle at the tip of the device. The most ideal specifications should be researched. To find the most suitable specifications like the most suitable spring thickness with corresponding stiffness and speed, prototypes will be produced and evaluated, as reported in the next chapter. Additionally. all three spring shapes will be tested before selecting the final spring shape.

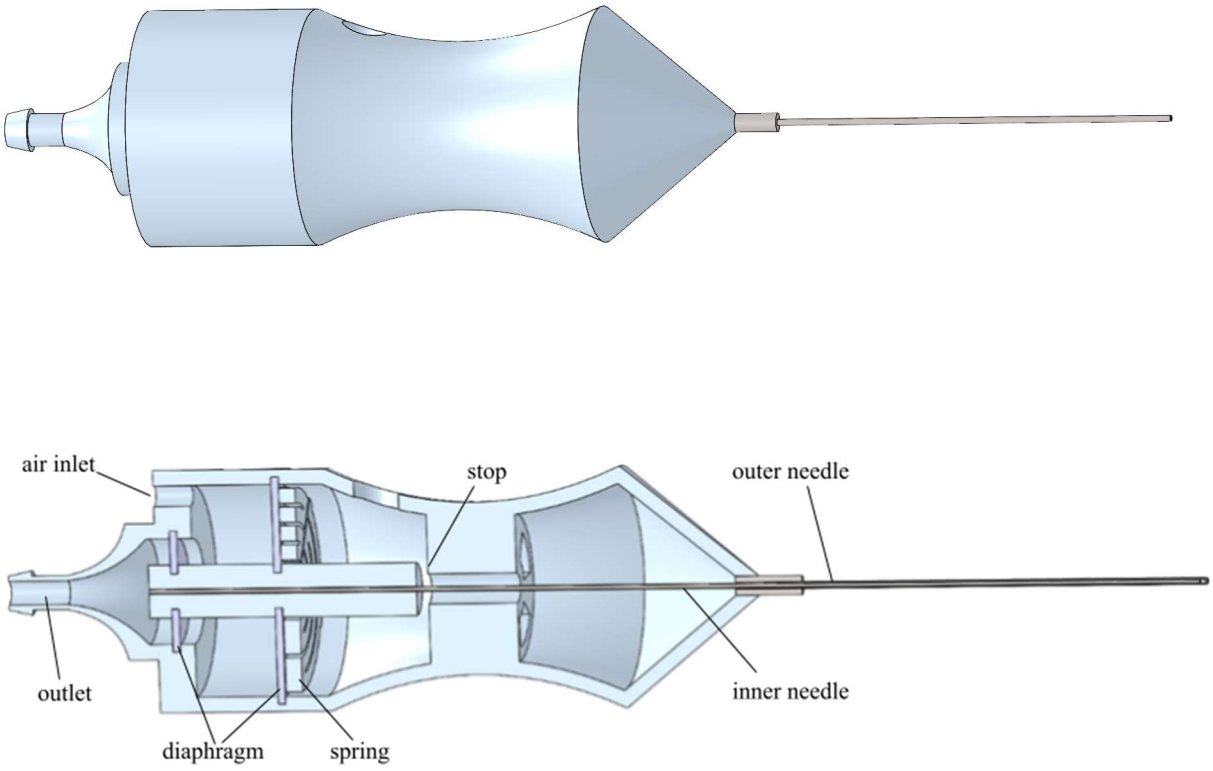

Fig. 25. 3D model spring reinforced dual flat diaphragm driven vitreous cutter and cross-section of the device

6 EVALUATION OF VARYING SPRING DESIGNS

6.1 Test goal

The working of the final selected vitreous cutter design described in section 5.5 should be tested. For testing purposes, six prototypes are created as described in section 6.2. Two tests are executed on the prototypes, the speed test and the force test, which will be described in sections 6.3 and 6.4 respectively. First of all, these tests should reveal if the stated requirements can be met for all prototypes. The speed test should show if the backward motion can be obtained within 0.0037 seconds. The force test should show if a force of 8N can be reached at a displacement of 0.8mm. Tests with air pressure are not executed since the diaphragms were leak due to production failures. Therefore, the speed of the forward motion could not be tested. However, the speed of the backward motion can still be tested by manually extending the springs.

Secondly, the tests should provide insight into the influence of the different design parameters like the shape and thickness of the spring. By obtaining insight into the influence of the design parameters it can be determined if altering the parameters might help to meet the requirements if they are not met in first instance. The most optimal design cannot completely be determined beforehand and requires more insight. Since the exact material properties are unknown the force test should reveal the actual stiffness of the prototypes that can later be used to design the exact preferred stiffness. Additionally, the force test should provide insight into the hysteresis of the spring-reinforced diaphragms since hysteresis was reasoned by Stolk et al [15] as the main reason for the relatively low backward motion.

6.2 Prototypes

Multiple prototypes are made to test the spring-reinforced dual flat diaphragm's principle. The prototypes should clarify if adding a spring to the dual flat driving mechanism design can decrease the return time. Therefore it is decided to first focus on the large diaphragm with additional spring. The small diaphragm is not included in the prototype design since Stolk et al. [15] already proved that the basic principle of the dual flat driving mechanism design functions and support can be removed. As described in section 5.3, three spring shapes will be tested. All springs consist of a needle carrier connected by flexible members to the outer base. The prototypes are made on the same scale as the preferred final design. The outer base diameter is set to 14 mm such that the design could fit inside the handle of the vitreous cutter. The diameter of the needle carrier forming the central platform of the spring is set to 2.72 mm to hold the inner needle of 0.32 mm. The exact dimensions of the prototypes can be found in 0.

Even though the flexible members are differently shaped, dimensions are chosen as consistent as possible to allow comparison. All spring elements have a minimum width of 1mm, corresponding with the minimum thickness of a supporting wall for PolyJet printing. Each design covers as much diaphragm area as possible by minimizing the space between the spring members to 0.25mm. By altering the thickness, the stiffness of the spring can be varied. On the one hand, the stiffness of the spring should at least generate a backward force of 8N at a displacement of 0.8mm and enhance the speed of the backward motion. On the other hand, the stiffness of the spring restricts the forward motion and requires a stronger pressure supply. Therefore, the optimal stiffness should be researched. However, it is difficult to determine the exact stiffness beforehand since the spring is not only loaded in the centre and deforms in a particular shape. Moreover, the exact material properties of the PolyJet materials are not stated by the manufacturer. The E-modules lies between 2000-3000 Mpa [57]. To give a rough indication of the final spring thickness, the minimal thickness of the spring is approximated by a complete diaphragm in the Vero material with a rigid centre. In Appendix VII the exact calculation based on equation (5) can be found. Adding cut-outs to the rigid material diaphragm to create spring elements only makes it softer, so the spring should at least have the thickness of a diaphragm in the same material. This result in a minimal spring thickness of 0.28 mm.

Aside from this simplified algebraic method, a numerical method can be used. The finite Element Analysis (FEA) tool of SolidWorks is used to determine the required thickness of each spring such that a backward force of 8 N is generated at 0,8 mm displacement. FEA is frequently used in soft robotics due to the common lack of methods and models with a feasible computation time [44]. For computation purposes, the lowest noted E-modules of 2000 MPa is used such that at least the minimal required force is generated. Since the actual E-modules is probably larger these springs are expected to be stiffer in reality. The springs with a thickness of 0.28mm are expected to be on the lower side of the stiffness range and the thickness calculated by FEA is expected to be on the upper side of the stiffness range. By selecting one relatively flexible spring and one relatively stiff spring but close to the final preferred stiffness of 8N at 0.8mm extension it can be researched if it could at least be possible to obtain the desired speed. Moreover, by testing the two extrema of

the flexibility range the influence of the thickness can be researched and afterwards a final spring thickness within this range can be selected. Overall, six samples are created with different shapes and thicknesses, as noted in Table 3. Each shape is produced in two thicknesses.

Table 3
Overview printed prototypes of varying spring shapes and thicknesses

Name	Spring shape	Spring thickness
S0.28	Spiral	0.28 mm
Z0.28	Zigzag	0.28 mm
F0.28	Folded beam	0.28 mm
S2.73	Spiral	2.73 mm
Z1.12	Zigzag	1.12 mm
F0.51	Folded beam	0.51 mm

The behaviour of these springs is dependent on different parameters like the shape, thickness and corresponding stiffness. By keeping all parameters constant and changing one parameter the influence of a specific parameter can be tested. In this way, the influence of the spring parameters can be revealed by selecting certain sets of springs for comparison. Comparing two samples with the same shape but different thicknesses can show the influence of the thickness. This can be done for each spring shape. The three prototypes of equal thickness of 0.28mm can show the influence of the shape on the stiffness and return time. S2.73, Z1.12 and F0.51 are expected to be of equal stiffness due to the FEA optimization. This allows testing the influence of the shape when the stiffness of each spring is equal.

Underneath each spring, an Agilus30 diaphragm of 0.5 mm thickness is placed to form the complete spring-reinforced large diaphragm. The Agilus30 diaphragm is only required for sealing purposes since the spring is responsible for the required stiffness for the backward motion. To minimize the use of flexible material, the thickness of the Agilus30 diaphragm is set equal to the minimum wall thickness for PolyJet printing. Since the elongation of flexible material results in hysteresis, minimizing the amount of flexible material is expected to increase the return speed. The Agilus30 diaphragm and spring are placed into a square housing, to allow easy clamping during tests. In Fig. 26 (a) one of the six spring-reinforced diaphragm prototypes is shown. The air inlet and stop plate are not directly integrated into the prototypes to simplify the production of the prototypes and allow easy support removal.

To still allow testing with air pressure, the prototypes can be attached to an air inlet part and a stop plate by four M3 bolts, as shown in Fig. 26 (b). The air inlet, as depicted in Fig. 26 (c), allows to form a closed air chamber and provides a connection to 10 mm diameter Festo tubes for the pressure supply system. The stop-plate, as depicted in Fig. 26 (d), limits the needle carrier's movement to 0.8 mm to prevent damage and allow to test the required time for the backward motion starting from the stop-plate. The exact dimensions of the prototypes, air inlet part and stop plate can be found in 0. All parts are printed at the Technical University of Delft on a Stratasys PolyJet printer. Visual inspection of the samples shows that the 0.28 mm prototypes are all slightly concave or convex in the rest position. Unfortunately, all printed samples were not airtight due to misaligning of the Agilus30 diaphragm. Luckily, some insightful tests could still be executed, as discussed in the next sections.

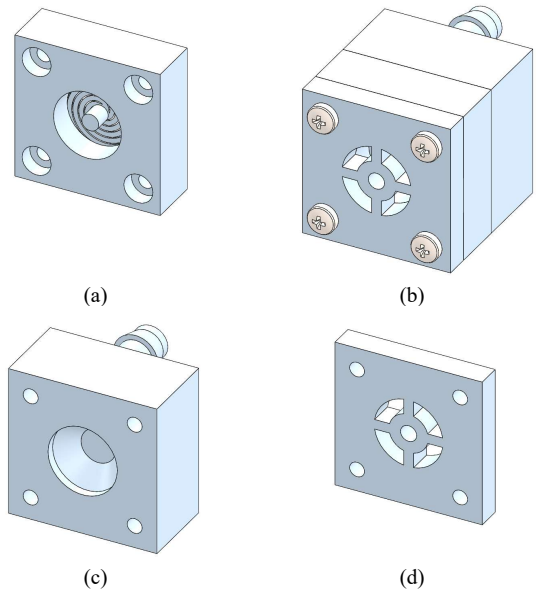

Fig. 26. 3D model of the prototype with (a) one of six spring reinforced diaphragm prototypes (b) prototype connected to air-inlet and stop-plate (c)air inlet (d) stop-plate

6.3 Speed test

6.3.1 Test procedure and setup

Since the prototypes appeared not airtight due to misaligning of the Agilus30 diaphragm, tests with air pressure could not be executed. However, the speed of the backward motion is still tested by manually extending the spring-reinforced large diaphragms. The needle carrier is pushed forward by a wooden rot until the top of the needle carrier is 0.8 mm displaced from the start position. The original stop plate is mounted on the back of the prototype to guide the rot. After the needle carrier is completely pushed forward and extended by 0.8 mm, the needle carrier is released to measure the return time. The displacement is measured during the complete forward and backward motion until no measurable motion for one minute after the release is noted.

A Micro-Epsilon ILD1420-10 laser sensor with additional National Instruments NI USB-6008 data

acquisition device is used to measure the displacement. The laser sensor is mounted onto a custom fixture that can clamp the prototype. The exact details of the fixture can be found in Appendix IV. The test setup, as depicted in Fig. 27, restricts movement between the laser and the clamped prototypes and assures that the extended needle carrier moves in the measurable range of the laser sensor. All measurements are saved with a loop time of 100 msec by a custom data collection program in LabVIEW, as described in Appendix V. All six prototypes are tested three times.

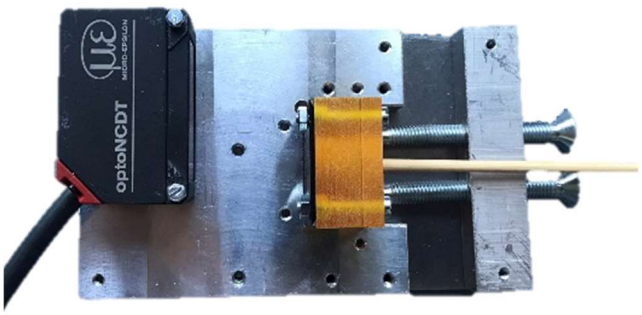

Fig. 27. Top view test setup manual speed test

6.3.2 Hypothesis

It is expected that the return time is mainly dependent on the stiffness. Increasing the stiffness results in decreasing the damping ratio and increasing the natural frequency, so stiffer samples are expected to return faster. Therefore, it is expected that S2.73, Z1.12 and F0.51 have the same return time due to the comparable stiffness. Furthermore, it is expected that these samples move back way faster than the 0.28 mm samples. Within the samples of 0.28 mm thickness, S0.28 is expected to have the slowest return time and F0.28 the fastest return time since from the FEA it appeared the spiral is the weakest shape and the folded beam the stiffest shape. Furthermore, it is expected that hysteresis has a negative effect on the return time. It is expected that the hysteresis ratio for all springs is in the same range since the same material is used for each spring. Therefore no significant difference in return time is expected due to hysteresis except for the spiral. The spiral is expected to have a slightly higher hysteresis ratio due to the additional rotation of the needle carrier. When loading a spiral structure in the out-of-plane direction a slight rotation is expected at the centre since the direction of the spring element forces all generate a moment in the same direction. Unwanted movement of the attached needle carrier will result in additional friction and hence additional hysteresis. However, the out-of-plane motion is relatively small, so the spiral spring's rotational effects might be neglectable.

6.3.3 Test results and evaluation

To evaluate the backward motion, the data set is shortened such that the last data point at an extension of 0.8mm or larger is defined as the start of the backward motion. Since most samples did not return exactly to a displacement of 0.0 mm, the time required for the backward motion is determined by taking the time difference between the start of the backward motion and the first datapoint with a displacement smaller than 0.05mm after the start of the backward motion. In Table 4 the mean time required to return to a displacement smaller than 0.05 mm is indicated for each prototype. The results of Z0.28 and F0.51 are marked in red since these springs appeared already broken after visual inspection. None of the samples reaches the start position within the stated requirements of 0.0037 seconds. The slowest tests are from S2.73, this was not expected since S2.73 is also relatively stiff in comparison with the 0.28 mm thickness prototypes. When not taking the result of the broken F0.51 into account, it appears that thicker springs move back slower than the 0.28 mm springs, which is unexpected. Considering the shape, F0.28 is slower than S0.28 which is also not expected.

Table 4
Mean time required to return to a extension smaller than 0.05 mm (n=3, each prototype is tested three times)

Name	Mean return time	Standard deviation
S0.28	21.9 sec	13.4 sec
Z0.28	19.9 sec	7.9 sec
F0.28	23.9 sec	4.2 sec
S2.73	67.4 sec	36.2 sec
Z1.12	34.4 sec	7.1 sec
F0.51	20.0 sec	22.6 sec

= unreliable results due to prior breakage

Fig. 28 the results of the first two minutes of the tests are all depicted in the time-displacement graph. The graph shows that all springs show similar behaviour, all prototypes move back immediately after the release, whereafter the backward speed keeps decreasing. At the end of the movement, the needle carrier slowly approximates the start position, indicated by a displacement of zero. Even though the spring was expected to decrease the damping ratio, the shape of all graphs indicates that the damping ratio is still larger or equal to 1, indicating a damped system. Especially the last 0.2 mm back to the start position requires a large part of the total return time. The expectations might not be fulfilled since it was expected that mainly the stiffness influenced the return time but when looking at the behaviour of the spring, especially the damping plays a crucial role. Moreover, the consistency between repetitive tests is low as indicated by the standard deviation in the last column of Table 4.

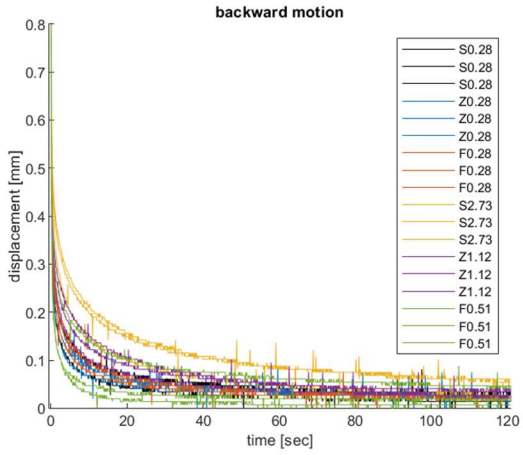

(a)

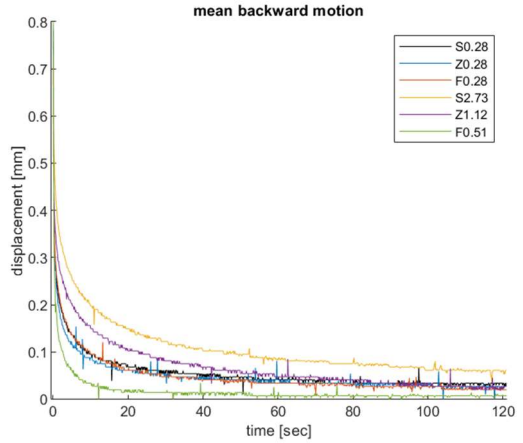

(b)

Fig. 28. Time displacement graph (a) backward motion, (b) mean backward motion for each prototype

6.4 Force test

6.4.1 Test procedure and setup

A picture of the total test setup for the force test is depicted in Fig. 29. A Lloyd LS1EH tensile tester with a 10N loadcell, a tapered needle and a custom fixture are used. The exact dimension of the custom fixture can be found in Appendix IV. The prototype is clamped into the custom fixture with the spring facing down and the Agilus30 diaphragm on top. The tapered needle is lowered until making the first contact with the needle carrier of the prototype. A measured contact force of 0.02N defines the first contact point. After the first contact, the needle pushes the needle carrier of the prototype downwards with a constant speed of 1mm/min until 0.8 mm extended, whereafter the needle starts moving upwards at the same speed to return to the initial position. Starting from the first contact point until completely returned, a thousand data points with the measured load and corresponding displacement are stored by the data collection software Nexygen plus. After testing each prototype once, the tests are repeated in the same order to assure that there are at least ten minutes between repeated tests on the same prototype. In this way, the prototypes can restore to their original position between tests and all six prototypes can be tested twice within a minimal overall testing time.

Fig. 29. Test setup force test

6.4.2 Hypothesis

Due to the SolidWorks optimization, it is expected that S2.73, Z1.12 and F0.51 show equal stiffness. However, this might not be exactly 8N at 0.8mm since the exact E-modules was unknown. Since the lowest indicated E-modules was used for the iteration process, it is expected that the springs are in reality stiffer. All 0.28 mm thickness springs are expected to be relatively weaker due to the small thickness. Furthermore, it is expected that from the springs with an equal thickness of 0.28 mm S0.28 is the weakest and F0.28 the stiffest prototype due to the found results of the FEA. The weakest spring is expected to have the lowest hysteresis and the stiffest spring the highest hysteresis due to the relatively higher overall elastic energy. Therefore, for the S2.73, Z1.12 and F0.51 a similar hysteresis is expected. However, the spiral shape is expected to have slightly higher hysteresis since this shape is expected to cause a small rotation of the needle carrier causing unwanted interaction with the diaphragm.

Furthermore, it is expected that all spring reinforced diaphragms show significantly less hysteresis than the original flat diaphragm design since the springs do not solely depend on material deformation but also on shape deformation and no material mixtures are used. However,

hysteresis is still expected since flexible materials are used and small energy losses are inevitable. It is expected that the hysteresis ratio for all springs is in the same range since the same material is used for each spring and aside from the internal material friction similar friction forces are expected. The spiral is expected to have a slightly higher ratio due to the additional rotation.

6.4.3 Test results and evaluation

The collected data points can be plotted in a force-displacement graph to provide direct insight into the spring-reinforced diaphragm's behaviour. These plots, depicted in

Fig. 30, show that repetitive tests behave similarly. The low force of the F0.51 sample is probably caused by prior spring breakage, which could be confirmed by visual inspection. From visual inspection and analysis of the graph, it appeared Z0.28 has also broken already; therefore, both results are considered inaccurate and are marked in red in Table 5. In Table 5 relevant data that can be extracted from the force displacements datapoints is noted. All results show the mean value of two force tests on the same prototype.

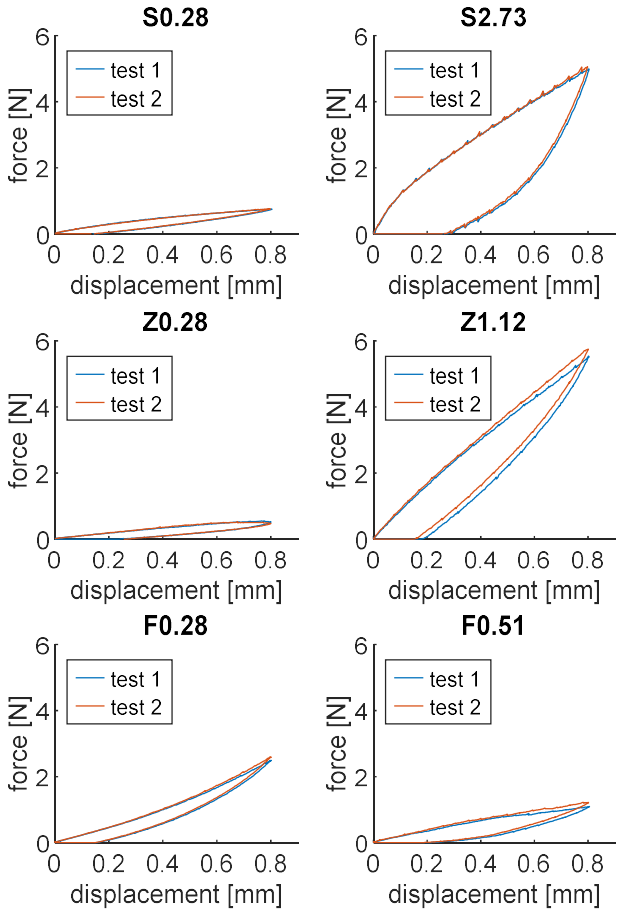

Fig. 30. force-displacement graphs of six spring reinforced diaphragm prototypes that are each tested twice.

Table 5
Mean values extracted from force-displacement datapoints (n=2, each prototype is tested twice)

Name	Force at 0.8 mm extension	Intersection x-axis	Hysteresis	Hysteresis loss ratio
S0.28	0.75 N	0.16 mm	0.15 Nmm	0.41
Z0.28	0.50 N	0.25 mm	0.15 Nmm	0.58
F0.28	2.54 N	0.15 mm	0.25 Nmm	0.28
S2.73	5.00 N	0.27 mm	1.44 Nmm	0.62
Z1.12	5.64 N	0.17 mm	0.90 Nmm	0.37
F0.51	1.15 N	0.21 mm	0.28 Nmm	0.53

= unreliable results due to prior breakage

In the second column of Table 5 the force at an extension of 0.8mm is noted. It can be seen that none of the prototypes reaches the preferred 8 N. Not taking Z0.28 into account, the spiral is the weakest shape, like expected. It can be seen that thicker springs are indeed relatively stiffer. Even though the results do not match the Solidworks iteration S2.73 and Z1.12 show a relatively similar force at 0.8 mm extension. However, it was expected that this force would be larger than 8N. The low forces might have had a negative effect on the speed of the backward motion. Moreover, none of the plots completely returns to the origin which might also have had a negative effect on the speed of the backward motion. In the third column of Table 5 the intersection point with the x-axis for all tests is noted. Around an extension of 0.2mm, the force is back to zero for all prototypes. This might be an explanation for the decrease in speed around an extension of 0.2mm during the speed test.

In the third column of Table 5 the hysteresis is noted. Hysteresis is defined by taking the difference between the area under the loading curve and unloading curve, represented by the upper and lower line in

Fig. 30 respectively. Hysteresis is related to energy losses due to internal friction and heat exchange with the environment. The results show that all springs exhibit hysteresis which is in line with the damping seen in the speed test. The hysteresis probably caused a low return speed of the spring-reinforced diaphragm. The thicker springs exhibit more hysteresis, which can be explained by the larger overall energy required to load the stiffer spring. For a stiffer spring, more energy is available to return the spring but also more energy is lost during the process. The ratio, between the lost energy and available energy, can offer more insight for comparison since for the final design all springs need to be optimized to fulfil the minimal required stiffness.

In the last column of Table 5, the hysteresis loss ratio is noted. This normalized value defined by the hysteresis loop area divided by the total area under the loading

curve can be used for comparisons, where a lower hysteresis loss ratio is beneficial. A hysteresis loss ratio of zero indicates a purely elastic spring where no energy is lost. It can be seen that the spiral with a thickness of 2.73 mm exhibits the most hysteresis since this graph corresponds with the largest hysteresis area and highest loss ratio. This is in line with the relatively slow results from the speed test and might be explained by the expectation that the spiral caused extra energy loss due to a rotational movement of the central platform causing additional friction. Even though it was expected that the spiral shape caused a slightly higher hysteresis ratio it was expected that the energy losses were mainly dependent on the material and hence more similar. The lower ratio of S0.28 in comparison to S2.73 might indicate that a thicker spring has a relatively higher hysteresis loss ratio which is contradictory to the expectations. Since the data of Z0.28 and F0.51 is considered unreliable due to the breakage of the parts, the other shapes cannot confirm the negative effect of the thickness. Overall, the hysteresis ratio is higher than expected and probably caused the low backward speed.

6.5 Overall test evaluation

Both the force test and the speed test show that the behaviour of the spring-reinforced diaphragms is suboptimal. The return time is higher than preferred and hysteresis is still present to a large extent. The stated requirements for the backward motion and force can not be obtained. In the research of Stolk et al. [17], the return time to span the last 0.8 mm back to the initial position for the relatively weak 80% Agilus30 and relatively stiff 80% Vero prototypes lies between 5.59 and 73.7 seconds respectively. Z1.12 might indicate an improvement to these designs since a higher return time can be obtained while still exerting a larger backward force. To meet all requirements, both sufficient stiffness and a fast return time should be obtained. However, no immediate conclusions can be drawn if the spring-reinforced diaphragm forms an improvement to the dual flat diaphragm design. Both designs show hysteresis which probably causes a low backward speed. However, the hysteresis can not be directly compared with each other since no hysteresis ratio is indicated in the report by Stolk et al. [17] and the absolute hysteresis cannot be directly used for comparison due to the difference in stiffness.

Overall, it is clear that design improvements to the spring-reinforced diaphragm are necessary to obtain a sufficient return time. Especially, the speed around the start position should be increased. Noticeable is the correspondence between the decrease of the backward motion speed around a displacement of 0.2 mm and the intersection with the x-axis around 0.2 mm from the force-displacement graph indicating that no force is generated in the backward direction. Additionally, follow-up tests should indicate the consistency of the prototypes to assure the production of a high-precision device. The visible inspection of the prototypes showing slight concave and convex deformation in rest position form a major concern. Additionally, tests with air pressure should still be executed to get more insight into the behaviour of the spring-reinforced diaphragm.

6.6 Improving the design

To obtain a sufficiently high backward speed, the design should be improved. Solely changing the spring thickness, shape or materials is not expected to solve the problem sufficiently. To compensate for the decrease in speed around the start position, the start position can be relocated. In this way, the complete stroke length can for example be relocated to start from 0.2mm and end at 1mm. At the relocated start position a force in the backward direction is still present, contrary to the backward force at the original start position. Relocation of the start position can be embodied by actuating the diaphragm before completely returned, a pre-pressure or a pre-tension.

Relocating the start position by actuating the diaphragm before completely returned does not require additional assembly steps. However, rightly balancing the design such that the exact preferred stroke length is obtained is challenging and the stroke length of the first and last actuation will be higher than 0.8 mm. Moreover, the driving mechanism should allow changing the frequency while the cut speed remains constant according to requirement fourteen. This cannot be obtained when the start location is dependent on the actuation frequency.

A pre-pressure on the other hand can allow for a consistent relocation of the start position. The air chamber itself can be pressurized or an additional chamber behind the spring-reinforced diaphragm can be pressurized. Pressurizing the current air chamber is not in line with requirement three, since this requires a slightly different actuation device than the current EVA pressure supply system. An additional pressure chamber behind the diaphragm requires an additional assembly step to pressurize and seal the chamber. Additionally, the spring-reinforced diaphragm start position will be relocated in the opposite direction such that the diaphragm moves through the original start position, making the spring only act in the backward direction after passing the original start position.

Mechanical pre-tension can me simply embodied by pushing the needle carrier forward during assembly to relocate the start position. Even though this requires an

additional assembly step, the need for trained technicians might still be eliminated. The device can be designed such that applying pretension is a simple assembly step like for example fastening a screw that pushes the needle carrier forward. Moreover, pretension allows to easily test the design on different relocated start positions to give a primary indication of the possible improvement. In the next section, the design of the prototypes allowing to test different relocated start positions is elaborated.

7 EVALUATION OF VARYING RELOCATED START POSITIONS

7.1 Prototypes

To test prototypes at different relocated start positions the prototypes are adapted. In Fig. 31 (a) the 3D model of one of the prototypes is depicted. The needle carrier is extended such that it can be placed into the additional pretension part depicted in Fig. 31 (b). The start and stop location of the prototypes can be relocated to preference by moving the additional pretension unit forward and tightening the two M2 bolds into the additional slots. The cross-section in Fig. 31 (c) clarifies the exact working of the stop plate, the disk mounted on the needle carrier is pulled forward by the pretension part to define the start position. When applying sufficient air pressure the disc is pressed against the other side of the pretension part such that a consistent stroke length of 0.8 mm is obtained.

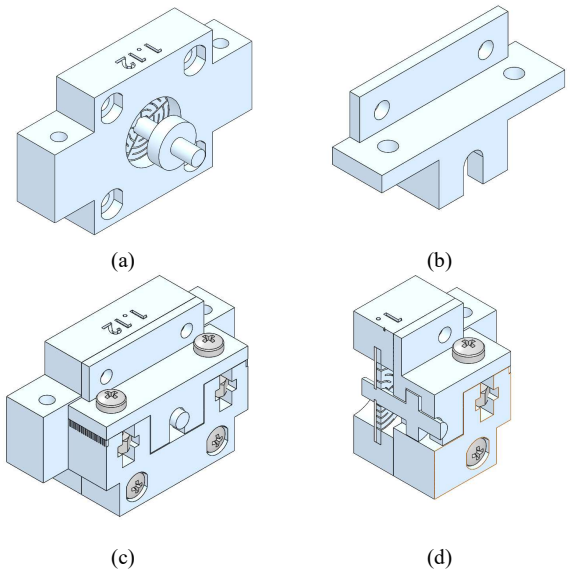

Fig. 31. (a) prototype, (b) additional pretension part (c) prototype mounted onto pretension parts (d) cross-section pretension part mounted onto prototype

To limit the cost and testing time of the prototypes it is decided to only continue the research with one spring shape. No immediate conclusion could be drawn from the previous test about the optimal spring shape but the spiral spring shape appeared non-beneficial. The zigzag-based spring shape is selected due to the promising result of the Z1.12 sample. Showing a relatively faster return time while still exerting a relatively higher backward force. The zigzag spring is produced in three varying thicknesses; 0.28 mm, 1.12 and 2.24 mm. To check the consistency and validate the test, each prototype is printed in threefold at 3D LifePrints. The samples are named by the spring shape and sample number, for example Z0.28_S1. The 0.28 mm and 1.12 mm samples can provide a validation of the previous test and the 2.24 mm sample can show the influence of a relatively stiffer sample since the required stiffness was not obtained in previous tests.

7.2 Test goal

The main aim is to determine if the required backward force, forward speed and backward speed can be obtained. The tests should provide insight into how these requirements might be met by investigating the influence of the pressure, spring thickness and start position. Additionally, the tests should substantiate the previously described results with more tests and prototypes. Since previous tests could not be tested with air pressure also the influence of the air pressure on the behaviour of the spring-reinforced diaphragms should still be investigated.

The force test in section 7.3 should determine if a force of 8N can be obtained at an extension of 0.8mm. The influence of the thickness on the backward force should indicate if the requirements might be met by altering the spring thickness. Additionally, this test should provide insight into the potential hysteresis of the designs. The force test is executed first for all prototypes since this test has a lower chance of breakage. The speed test described in section 7.4 should determine if a forward motion of 0.8mm can be obtained within 0.0037 seconds and if the backward motion of 0.8mm can be obtained within 0.0037 seconds. For the forward motion, it should be identified if altering the pressure allows for meeting the requirements. For the backward motion, it should be identified if altering the start position or spring thickness allows for meeting the requirements.

7.3 Force test

7.3.1 Test procedure and setup

For the force test, the same test setup as the previously described force test in section 6.4 is used. The prototypes are attached to one of the old prototypes from which the spring-reinforced diaphragm is removed. In this manner, the enlarged needle carrier can move freely and the prototype can be clamped. In Fig. 32 a picture of the

prototype in white attached by four M3 bolds to the housing of the old prototype depicted in yellow is shown. Due to the limited testing time each prototype is only tested once.

Fig. 32. prototype attached on top of the old yellow prototype with removed diaphragm

7.3.2 Hypothesis

The previous batch with different spring shapes gave already an indication of the stiffness and hysteresis. Since the Z0.28 sample appeared broken in the previous tests, it is expected that the results of the second batch have a higher stiffness. For the Z1.12 sample results similar to the previous batch are expected. Furthermore, it is expected that thicker designs have a higher spring stiffness, like also shown in the previous tests. Since the shape is the same for all prototypes, similar friction forces are expected and more over similar internal friction forces associated with the material are expected. As a result, the hysteresis loss ratio is expected to be the same for all prototypes even though the previous test of the spiral showed different results.

7.3.3 Test results and evaluation

In Fig. 33 the results of the force tests are plotted. The y-axis is scaled to the maximum force to clearly display all graphs. It can be noted that thicker samples indeed show a higher maximum force at 0.8 mm, like also noted in Table 6. Z2.24 meets the requirement of 8N at an extension of 0.8 mm. The Z1.12 samples show a maximum force of around four newtons which is lower in comparison to the previous batch, showing a maximum of around 5.5 N. The inconsistency might be caused by printing the samples on a different printer or due to the slightly different material use. However, the prototypes produced on the same printer and having the same design still show inconsistencies. Especially the second Z0.28 prototype shows different behaviour than the other Z0.28 prototypes. This is probably because the Z0.28 prototypes do not all have the same stable flat start position. All samples appeared slightly concave or convex and show a slightly tilted needle carrier.

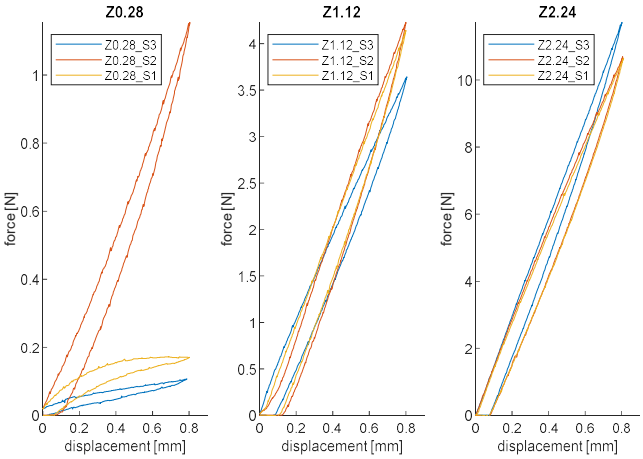

Fig. 33. force-displacement graphs of Z0.28, Z1.12, Z2.24 and D0.50 with three prototypes per design. Note the different scales of the Y-axis.

Table 6
force at 0.8mm extension

Name	Prototype 1	Prototype 2	Prototype 3	Mean
Z0.28	0.17 N	1.15 N	0.11 N	0.48 N
Z1.12	4.13 N	4.22 N	3.64 N	4.00 N
Z2.24	10.65 N	10.69 N	11.70 N	11.02 N

The hysteresis loss ratio, noted in Table 7, is as expected, quite similar for all prototypes. Prototypes of the same thickness also show a consistent hysteresis loss ratio. However, inconsistencies with the previous batch are shown again for the Z1.12 prototypes. The prototypes of the second batch show less hysteresis than the previous batch. Again this can be caused by the different printer or material. The removal of the support material might also influence the hysteresis. In the first batch, the support still needed to be removed by using a sodium hydroxide solution and in the second batch, the support was already removed by the external company 3D LifePrints. The prototypes of both batches show some residual support onto the surface when whetting the prototypes and lightly scratching the surface. Especially support between the spring members might cause some additional hysteresis.

Table 7
hysteresis loss ratio

Name	Prototype 1	Prototype 2	Prototype 3	Mean
Z0.28	0.292	0.209	0.315	0.272
Z1.12	0.201	0.213	0.215	0.210
Z2.24	0.186	0.200	0.159	0.182

7.4 Speed test

7.4.1 Test procedure and setup

To measure the displacement of the spring-reinforced diaphragm by means of an applied pressure, a Micro-Epsilon ILD1750-2 laser is used. This laser sensor measures at a rate of 7000 samples/second. This is higher than the previous laser described in 6.3 such that the speed can be measured with higher accuracy. The laser

sensor and prototype are mounted onto the custom fixture described in Appendix IV. In Fig. 34 a graphical visualization of the test setup is depicted. On the right side, the laser is attached to a National Instruments NI USB-6008 data acquisition device. This device is connected to a PC running the LabVIEW data collection software described in 0. In this way, data points containing the distance to the needle carrier are stored. The needle carrier can be displaced by applying pressure. A GE Pace 5000 Pressure controller connected to a 10-bar air supply is used to precisely apply pressure. The pressure controller is connected with 10mm diameter Festo tubes to the prototype via a pressure tank and a valve. The Festo valve allows applying a pressure pulse to the prototype. The CRVZS 0.4L Festo pressure tank is used to compensate for the sudden volume change due to the additional tubes and air chamber in the prototype after opening the valve.

Fig. 34. Graphical visualization of the speed test setup

This test setup is used to determine both the required time of the forward motion and the required time of the backward motion. For the forward motion test, the response of the prototypes is tested on different pressure levels and for the backward motion test, the response of the prototypes is tested for different relocated start positions. For the forward motion one prototype in each thickness is used. Another three prototypes in each thickness are used for the backward motion. Only three prototypes per test could be used due to the fast breakage of the springs. The pretension part is attached to the prototypes to limit the movement. For the forward motion, this part is attached to fungate as a stop plate without relocating the start or applying a pretension. For the backward motion on the other hand the pretension part allows to relocate the start position and apply a pretension, as described in section 7.1.

Before each test, a calibration test is done to determine the pressure required for an 0.8mm extension. During the calibration test, the valve is kept open and the pressure gradually increased until a displacement of 0.8 mm is reached. For the forward motion test also the required pressure for an extension of 0.1mm is noted. This pressure is used as an incremental step of the forward motion test. During the forward motion test, the preferred pressure is installed on the pressure controller, and as soon as the pressure is constant, the valve is manually opened. As a result, the spring-reinforced diaphragm is pushed forward. When a displacement of 0.8 mm is noted or no displacement is noted for 30 seconds the valve is closed. After the valve is closed, the spring-reinforced diaphragm starts the backward motion. If the prototype is returned, the next test is executed. All three prototypes are tested twice on each pressure level until breakage.

Before testing the backward motion, the offset in the LabVIEW control panel is calibrated such that the natural position of the diaphragm is set to a displacement of zero. In this way, the measured distance to the needle carrier is compensated and the start position can be easily read from the control panel. The start can be relocated by pulling the pretension part forward until the preferred displacement is noted in the LabVIEW control panel. After the start position is relocated and the pretension part is locked by the two M2 bolds the preferred pressure level, obtained from the calibration test, is installed on the pressure controller. If the pressure is constant the valve is opened and the diaphragm pushed forward. As soon as a displacement of 0.8mm is noted the valve is closed. If the reinforced diaphragm is returned to the relocated start position or no displacement is noted for 2 minutes the measurement is stopped. Each prototype is tested on relocated start positions ranging from 0 mm to 0.8 mm with an incremental step of 0.1 mm. At each start position, the test is repeated once for each prototype.

7.4.2 Hypothesis

For the calibration, it is expected that the thicker samples require more pressure for the same amount of extension. For the forward motion, it is expected that an increase in pressure has a positive effect on the speed of the forward motion. Moreover, it is expected that with sufficiently high pressure the forward motion can be executed within 0.0037 seconds. However, some prototypes might break beforehand. Moreover, for the stiffer Z2.24 sample the 10-bar pressure supply might not be sufficient to obtain the required speed.

For the backward motion, it is expected that relocating the start position result in a faster return time. The pretension due to the relocated start position is expected to have an overall positive effect on the speed due to the increased force at the relocated stroke. Moreover, the pretension is expected to compensate for the decrease in speed around the original start position seen in previous tests, since pretension will cause the diaphragm to also exert a force at the relocated start position. With this reasoning, it is expected that the largest speed increase is up to an extension of 0.2 mm. It is expected that the speed still keeps increasing when relocating the start position even further away from the original start but at a lower rate. Theoretically, the thickness is also expected to have a positive effect on the return time. Thicker samples are expected to return faster due to the increased stiffness even though previous tests showed that a thicker spiral had a lower speed than a thinner spiral. Overall, it is expected that the combination of a thicker sample and a higher pretension allows to return to the relocated start position within 0.0037 seconds.

7.4.3 Test results and evaluation

From the calibration test of the three prototypes used for the forward motion test, it appeared that the minimum pressure required for a displacement of 0.8 mm was 20 Pa, 250 Pa and 400 Pa for the Z0.28_S1, Z1.12_S2 and Z2.24_S3 samples respectively. However, when applying the pressure pulse for the forward motion, the samples did not directly reach the 0.8mm extension and slowly approximated the final extension, or the final extension of 0.8mm was not reached at all. In the fourth column of Table 8, the time required to move 0.8mm forward is shown. The Z0.28_S1 prototype did not reach an extension of 0.8 mm. Since the 5 Pa incremental step in pressure did not result in sufficient extension increase, tests at 50 Pa an 100 Pa followed, but 0.8mm extension was not reached. Z1.12 and Z2.24 did reach the preferred extension, but none of the prototypes reached an extension of 0.8mm within 0.0037 seconds.

Especially the last part of the forward motion is relatively slow. In Fig. 35 the time displacement plot of Z1.12_S2 at a pressure of 250 Pa is shown to give an illustration of the behaviour. It can be seen that for an extension up to 0.7 mm less than a second is required whereafter reaching the final extension of 0.8 mm requires more than a hundred seconds. This might be due to the added extra volume inside the prototypes and hoses directly after opening the valve. Another explication might be creep, a phenomenon seen in viscoelastic material. Creep results in an extension increase due to a constant applied force. During calibration, the diaphragm was pressurized for a prolonged time which might have resulted in a higher extension under relatively lower pressure. This might explain why there is also a longer time required to reach the final 0.8 mm extension. For PolyJet materials like Agilus30 viscoelastic effects like time dependency and creep is a still investigated effect [58].

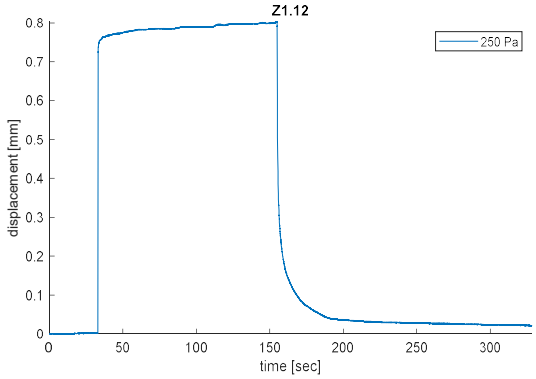

Fig. 35. Time displacement graph Z1.12 prototype response at 250 Pa

In contrast to the last part of the forward motion, the first part of the plot is relatively steep. In Fig. 36 the mean forward motion up to an extension 0f 0.4 mm is plotted. The plots show close to linear behaviour and all reach 0.4 mm within 0.01 seconds. The mean time required between an extension of 0.05mm until 0.4mm is exactly shown in the last column of Table 8. For Z0.28 it can be clearly seen that increasing the pressure has a positive effect on the speed of the forward motion. Also for Z2.24 the pressure increase has a positive effect up to a pressure of 500 Pa whereafter the differences become smaller. For the Z1.12 insight into the pressure influence could not be obtained due to breakage of the prototype. A small leak in the diaphragm might influence the speed of the forward motion while it is not exactly determined when the leaks are formed. A leak was only noted after the diaphragm completely broke or the diaphragm could not be moved forward sufficiently by pressure. The leak of the diaphragm and breakage of the spring might be due to the higher pressures or due to fatigue after multiple tests.

Table 8
Results forward motion
(Each prototype is tested twice on each pressure level)

Name	Applied pressure	rupture	Time required for 0.8 mm extension	Time between 0.05mm - 0.4mm
Z0.28 S1	20 Pa	-	0.8mm not reached	Mean = 5.6e-3 sec
	25 Pa	-	0.8mm not reached	Mean = 4.6e-3 sec
	30 Pa	-	0.8mm not reached	Mean = 3.6 e-3 sec
	50 Pa	-	0.8mm not reached	Mean = 3.1 e-3 sec
	100 Pa	-	0.8mm not reached	Mean = 1.9 e-3 sec
Z1.12 S2	250 Pa	-	Mean = 145.7 sec	Mean = 7.0 e-3 sec
	270 Pa	At test 2	Test 1 = 37.7 sec	Test 1 = 8.0 e-3 sec
Z2.24 S3	400 Pa	-	0.8mm not reached	Mean = 7.7 e-3 sec
	450 Pa	-	Mean = 38.6 sec	Mean = 7.1 e-3 sec
	500 Pa	-	Mean = 9.1 sec	Mean = 5.9 e-3 sec
	550 Pa	-	Mean = 11.8 sec	Mean = 5.6 e-3 sec
	600 Pa	At test 2	Test 1= 3.1 sec	Test 1= 6.0 e-3 sec

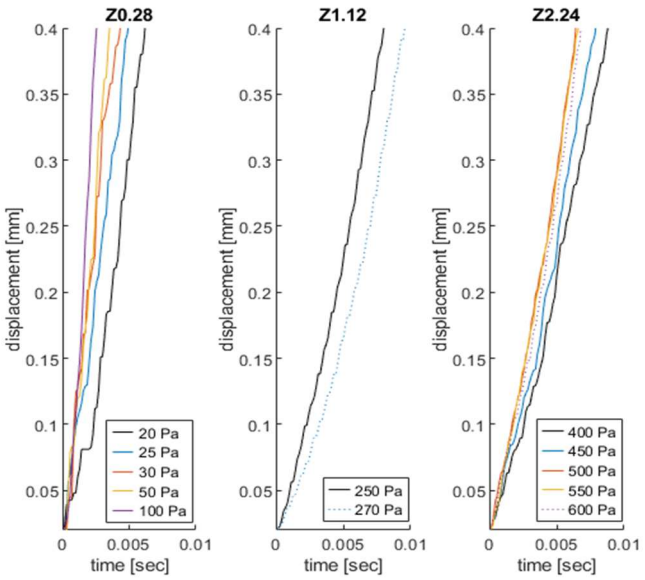

Fig. 36. Mean forward motion of first 0.4 mm extension. (Dashed line shows the results of a single test since the sample broke at the second repetitive test)

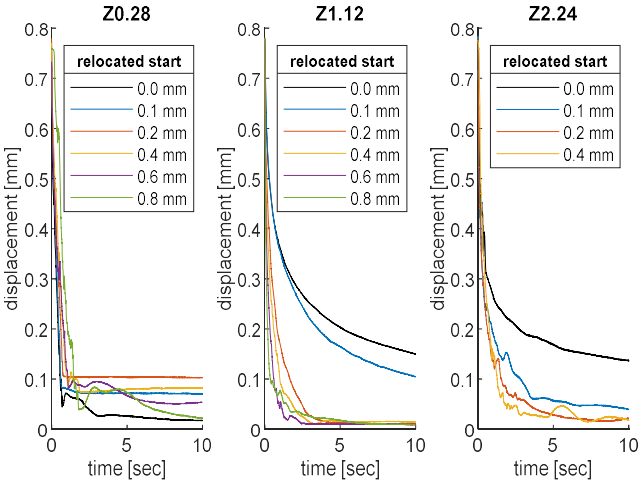

Fig. 37. Mean return time of two tests on the same prototype for different relocated start positions (pretension).

For the backward speed, the Z0.28_S1, Z1.12_S1 and Z2.24_S2 samples are tested at a pressure of 20Pa 300Pa and 500 Pa respectively. Each prototype is tested twice on each relocated start position. In Fig. 37 the mean backward motion is plotted. It can be seen that the speed remains higher at the beginning of the backward motion and decreases around the relocated start position. In Table 9 the exact results are stated. Since most samples did not return exactly to the relocated start position, the required return time depicted in the second column of Table 9 shows the time required to return to a displacement within 0.05 mm from the relocated start position. However, not all tests returned, as stated in Table 9.

The Z0.28 only reached an extension of 0,8 mm and completely returns for both tests at a relocated start position of 0.8mm. As a result, the influence of a relocated start on the complete backward motion cannot be shown for Z0.28. For Z1.12 and Z2.24 relocating the start further away appears beneficial, as expected. The pretension of Z1.12_S1 appears mainly beneficial up to 0.2mm whereafter the difference in return time becomes smaller, as expected. The return time of the Z1.12_S1 prototype decreases when increasing the pretension, until a slight increase is noted for the last measured mean return time. The last measured return time might be slightly increased due to small breakages in the spring. Breakage of the spring might also form an explanation for the bumps seen in the plots. Additional friction might have been caused by spring breakage or friction between thee needle carrier with the stop plate and the pretension part.

Table 9
Results backward motion (n=2)

Name	Start relocated	Mean return time (within 0.05 mm from start)	Mean time between 0.6mm and 0.2mm
Z0.28_S1	0.0 mm	0.8mm extension not reached	0.4 sec
	0.1 mm	Not all tests returned	0.4 sec
	0.2 mm	Not all tests returned	0.5 sec
	0.4 mm	Not all tests returned	0.7 sec
	0.6 mm	Not all tests returned	0.8 sec
	0.8 mm	1.7 sec	0.7 sec
Z1.12_S1	0.0 mm	47.0 sec	5.4 sec
	0.1 mm	23.9 sec	3.4 sec
	0.2 mm	2.5 sec	0.8 sec
	0.4 mm	1.6 sec	0.6 sec
	0.6 mm	1.1 sec	0.3 sec
	0.8 mm	2.3 sec	0.2 sec
Z2.24_S2	0.0 mm	Not all tests returned	2.5 sec
	0.1 mm	4.4 sec	1.0 sec
	0.2 mm	3.2 sec	0.6 sec
	0.4 mm	1.9 sec	0.6 sec
	0.6 mm	Rupture at test 1	-

Overall, the Z1.12_S1 sample at a relocated start of 0.6mm shows the fastest measured mean return time of 1.1 seconds. Even though the pretension does increase the speed of the backward motion in comparison with the tests without pretension, none of the tests meets the requirements of a return time below 0.0037 seconds. Especially the last part of the backward motion maintains relatively slow. In Fig. 38Fig. 38 and the last column of Table 9 the time between an extension of 0,6 and 0.2 mm is shown. When ignoring the first 0.2mm of the starting and ending, it can be seen that the time can be relatively reduced. As a result, it might be beneficial to create vitreous cutters with room for overshoot. For Z1.12 and Z2.24 relocating the start has an overall positive effect on the return time indicated by the decaying line in Fig. 38.

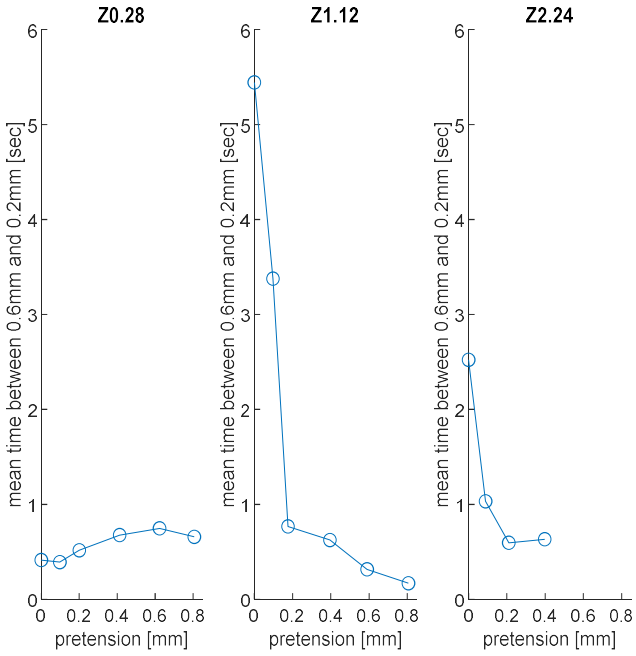

Fig. 38. mean time required to return from 0.6mm to 0.2mm

7.5 Overall test evaluation

From the tests, it becomes clear that the stated speed requirements can not be obtained. Since no sufficient increase in speed is revealed due to an increase in thickness, pressure or pretension, it is expected that this speed can also not be obtained by slightly altering the design. Additionally, the lifetime of the prototypes appeared insufficient. The samples broke either due to high pressure or due to fatigue from repeated movements. The Z0.28 prototypes were deformed in the rest position which can result in unpredictable and inaccurate behaviour with is not acceptable within the high precision requirements. A minimum stiffness is required to ensure that the reinforced diaphragm remains at the rest position when not pressurized. The Z2.24 showed the highest stiffness and could meet the force requirement of minimum 8N at 0.8mm extension.

Even though the speed requirements could not be fulfilled, relatively high speeds where noted for the beginning of the forward and backward motion, indicated by a steep slope in the time displacements plots. Relocating the start position appeared beneficial for decreasing the return time. Moreover, the spring-reinforced diaphragms are more likely to completely return to the relocated start position when relocating the start position. The Z1.12 at a relocated start of 0.6mm shows the fastest return time of 1.1 seconds which is a 98% decrease in return time compared with the return time for the same prototype without a relocated start.

8 DISCUSSION

8.1 Progress

3D Printing is a rather new production process for developing end-user components. Specific material properties are often unknown and mechanical responses are not yet widely researched. Research in this field can contribute to the further understanding of the design possibilities and limitations. This research contributed to new knowledge and further insight into PolyJet printing. The speed test revealed the displacement over time after an extension of the spring-reinforced diaphragm. It could be seen that a Vero spring exhibits damping and slowly approximates the initial rest position. Implying the relatively stiffer Vero material still exhibits hysteresis, even though Vero was produced into a spring shape to allow extension. The force test confirmed the presence of hysteresis and revealed the mechanical responses of a spring-reinforced diaphragm. An important finding that can now be taken into account for developing devices dependent on the mechanical response of Vero.

In the specific case of producing a non-assembly vitreous cutter, more insight is obtained into the possibilities and additional drawbacks. Different potential design directions are revealed and the spring reinforced dual flat diaphragm design is tested. A first indication is given into the influence of multiple parameters like the spring shape, thickness and relocating the start position. The shape and thickness did not appear to offer a high increase in backward speed. Especially relocating the start position appeared beneficial, showing a decrease in the return time of 98%. More insight into the spring-reinforced diaphragm's behaviour is obtained which allows further advances in future designs. Even though not all requirements were fulfilled, a design for a non-assembly high-speed vitreous cutter is made. With the upcoming developments in the 3D Printing techniques and materials, the design might form the basis of a working vitreous cutter.

8.2 Test Limitations

Vitreous cutters are often small and lightweight to enhance the precision required during vitrectomy. However, the precision of the stated prototypes and tests can be argued. The executed tests did encounter some limitations. During the speed test with pressure, the exact stroke length of the tests differed, causing a difference in the measured return time. The difference in stroke length can be due to insufficient pressure or a slight deformation of the spring-reinforced diaphragm causing the start position to relocate. Another reason might be a slight variation in dimensions of the thickness of the stop disc. By soaking the prototype in water and slightly scratching

the surface, it was noted that for all prototypes a small layer of support covered the surface. In the case of the stop disc, variation in thickness of this support residue might cause a difference in the stroke length. However, the same problem will be encountered during the production of the final design for consumer purposes, making the result realistic for production but hard to use for comparison reasons within the different prototypes.

The measured speed might also be influenced by the manually closing of the valve. A slower closing of the valve might cause a delay. Some graphs show a sharp return at the start of the backward motion whereas other graphs show first a slight displacement decrease before quickly starting the return. The test setup allowed to first identify the working of one single forward and backward motion. However, the found result might not exactly match the final behaviour when mounting the device to the EVA pressure supply system. During the pressure tests, the valve is kept open until a complete extension could be reached. On the contrary, the EVA pressure supply system will give multiple short pressure pulses. When applying pressure pulses the reinforced diaphragm might not completely extend at the same pressure level. Moreover, the diaphragm will probably not be completely returned before the next pulse is given. Applying direct pulses instead of waiting till completely extended or returned will probably also influence the behaviour of the spring-reinforced diaphragm due to the time dependency of the material.

Time dependency due to viscoelastic effects of the material was not taken into account beforehand. It was assumed Vero in the shape of a spring would behave elastic, but viscoelastic effects might have occurred and influenced the results and the design choices. Hysteresis is also a viscoelastic effect and resulted in a lower backward speed. Another viscoelastic effect is relaxation, a decrease in force at a constant extension. The relaxation effect can influence the results of the speed tests and force tests. If the spring force decreases when the diaphragm is extended for a prolonged time a lower force will be measured at a relatively slow force test. During the speed test, the speed of the backward motion can decrease due to a prolonged extension time before starting the backward motion. The extension time of each test differed since each diaphragm was pressed forward until an extension of 0.8mm was reached. The different extension times might have influenced the speed of the backward motion. Moreover, the backward speed might be different in the final application when the diaphragm is only pressed forward for a short amount of time.

Creep was also seen in the results. Resulting in slowly approximating the 0,8mm extension at a constant pressure. This might have caused the required pressure during the calibration test not to coincide with the required pressure for the pressure pulse during the speed test, resulting in a shorter stroke length which is hard to compare. Also the rate dependency might have influenced bot the speed and force test. At a higher rate, viscous elastic material behaves stiffer. So the speed of the force test might have led to a lower measured force than that would be present when giving a direct pressure pulse. Changing the speed of the speed test can cause different results.

Moreover, the force test is done at a rate of 1mm/min, resulting in a backward motion within 48 seconds. From the speed test, it could be seen that naturally, it can take even longer to completely return. If you move the tensile tester faster than the diaphragm naturally returns you will lose contact with the needle carrier and measure a lower force and higher hysteresis. Pre-conditioning might also affect the results. When a viscous elastic sample is repeatedly loaded the energy losses per cycle decrease and start behaving more elastically. This is beneficial when using the device during the multiple required load cycles and might result in better functioning of the device after repeatedly loading. However, preconditioning can result in differences between repetitive tests.

In general, comparisons are hard to make due to the limited amount of data. The amount of prototypes is limited to spare costs and time. Each test is only repeated once per prototype due to limited time at the testing facility. Moreover, due to early breakage, the speed test could not be repeated for multiple prototypes and only a limited amount of results could be shown. The tests could give an indication but to draw hard conclusions on the influence of the spring thickness, spring shape or applied pressure more tests are required. Moreover, it was not exactly determined when the samples became leak or broke. Breakage was only noted when the leak was to such an extent that the diaphragm could not be moved forward anymore. This might for example caused a decrease in speed for an increased pretension without noticing the reason. Breakage of the parts forms a limitation of the number of tests and accuracy of the obtained data but on the other hand, breakage also shows an important negative effect of the design. Overall, test limitations result in inaccuracies of the measurements making it hard to find the exact result and make a comparison between different design parameters like the pressure, thickness and pretension. However, test inaccuracies also partly reflect the main problem of the design showing a fast breakage and a lack of consistency.

8.3 Design limitations

The prototypes showed that the durability of the diaphragm forms the main limitation of the design. The diaphragms are either not capable of withstanding high pressures or multiple load cycles. According to the manufacturer, Agilus30 is capable of withstanding repeated flexing and bending [59]. The thickness of the diaphragm might have had a negative effect on its durability. However, also with a thicker Agilus30 diaphragm, the durability of the spring itself forms a concern. The unknown material properties make it hard to optimize the design. Due to unknown material factors and time dependency, a lot of iteration steps based on trial and error are required. The time dependency of the material also forms a general limitation of the design.

The speed of the backward motion still forms a major drawback of the design. Adding a spring to the diaphragm did not seem to lower the damping ratio sufficiently, the system remains overdamped resulting in a too slow backward motion. Changing the shape or thickness did not appear to offer a direct solution. The exact influence of the shape and thickness is hard to identify. However, a small thickness of 0.28 mm did appear unpractical. The needle carrier could not be kept straight and the diaphragm was often already deformed before applying the first load. Moreover, the thin diaphragm did not start exactly at the designed start position, causing a different stroke length. Moreover, a too thin spring is more unlikely to completely return to the start position at lower pretensions.

Increasing the thickness does appear to partly solve the problem. However, Z2.24 might be more likely to break at higher pretensions when relocating the start further away from the natural start. For the forward motions on the contrary Z2.24 is able to withstand a higher pressure before breakage and shows the fastest measured forward motion. Moreover increasing the thickness indeed allowed to increase the stiffness, making Z2.24 meet the requirements of 8N at an extension of 0.8mm. Z1.12 appears to withstand higher pretensions before breakage while still returning to the start position but does not meet the force requirements. Overall, altering the thickness, shape or relocating the start position does not sufficiently decrease the return time. The material exhibits hysteresis resulting in damping and a to slow backward motion. With the currently available materials and 3D Printing techniques, the design can probably not meet all requirements.

8.4 Recommendations and further research

Both the force test and speed test can only serve as a primary indication of the working of the spring-reinforced diaphragm. Since the number of prototypes and tests is limited, to reduce cost and testing time, no immediate conclusions with high certainty can be drawn. If the potential of the spring-reinforced diaphragm design must be completely proven, the test should be repeated with more prototypes for higher fidelity. Moreover, the test should be repeated with the EVA pressure supply system to investigate the exact behaviour of the spring under pressure pulses. However, it is expected that the spring-reinforced diaphragm will not offer a high potential solution path in the current state.

The design should be optimized such that the durability and speed can be increased. FEA is a key tool in this optimization process. However, the material properties used in this research appeared non-compatible with the final tested results. Moreover, the time dependency of the material was not taken into account beforehand. To form an improvement, FEA requires better-specified material properties. Current PolyJet material models are inconsistent and the time-dependency is often over-simplified due to the limited amount of research into PolyJet materials [58]. Since the required force, speed and durability play a key role in the working of the vitreous cutter, but are highly dependent on the material properties and time-dependency, the production of a valid material model suitable for FEA is crucial and hence recommended for further research. Moreover, other available materials should also be tested to provide more insight into the best suitable material. Overall, for all possible design directions depending on flexible material first further research into the mechanical response of the 3D Printed material is required.

Since the spring-reinforced dual flat diaphragm concept is strongly dependent on the mechanical response of the material it is expected that multiple optimizations are required to meet the speed and lifetime requirements, which might form a time-consuming process or might even be impossible within the currently available printable material properties. This research tested if the most preferable solution path could lead to a design meeting all requirements. It was aimed to design a non-assembly device directly adaptable to the EVA pressure supply system. However, to faster come to a solution it is recommended to not aim for the most ideal solution but do some consensus on the list of requirements and wishes.

When doing a consensus on the preferred pressure supply a higher pressure could be used or an alternating pressure. The dual actuated flat diaphragm design makes use of an alternating pressure to move both forward and backward. This concept is recommended for further research since this system it is more likely to meet the speed requirement. The speed decrease due to damping

might be compensated by applying a higher pressure and less emphasis is on the spring constant of the diaphragm. Another option would be de increase of the pressure supply allowing for designs with a higher spring constant and decreasing the need for flexible materials. The bellow concept might be produced out of stiff material like metal. Also, a consensus on the size requirements might allow the production of a bellow concept.

The force requirement might also be altered. It is unknown how much force is exactly required to cut vitreous. When further optimizing the design it is recommended to further investigate the minimal required force. Furthermore, there can also be done a consensus on the non-assembly requirement. Instead of aiming to make a complete non-assembly device, the assembly process might be simplified such that trained technicians are no longer required. 3D Printing might still offer opportunities in this simplification process. Simplifying the assembly process is recommended to partly offer a solution when a quick solution is required. However, better solutions might already become available in the near future. 3D Printing techniques and materials are still evolving and might allow for a non-assembly vitreous cutter.

9 CONCLUSION

The aim of this study was to deliver a non-assembly 3D Printed driving mechanism design for a high-speed reciprocating needle used during vitrectomy. In this research, multiple design directions are found and the spring reinforced dual flat driving mechanism is indicated as the most ideal solution if all requirements can be met. A first step in the validation of the design is made by means of prototypes and tests. Tests indicate that the desired speed cannot be obtained and durability forms a major concern. However, relocating the start position appeared beneficial, showing a decrease in the return time of 98. With the currently available materials and 3D Printing techniques, the spring-reinforced diaphragm design can probably not meet all requirements. However, a design for a non-assembly high-speed vitreous cutter is presented and with the upcoming developments in 3D Printing techniques and materials, the design might form the basis of a high-speed vitreous cutter such that the need for trained technicians for assembly can be eliminated.

10 REFERENCES

[1] C. F. Blodi, “David Kasner, MD, and the Road to Pars Plana Vitrectomy,” *Ophthalmol Eye Dis*, vol. 8s1, no. Suppl 1, p. OED.S40424, Jan. 2016, doi: 10.4137/oed.s40424.

[2] J. Keller and H. Madi, “Increasing frequency of hospital admissions for retinal detachment and vitreo-retinal surgery in England 2000-2018,” *medRxiv*, p. 2020.11.06.20214734, Nov. 2020, doi: 10.1101/2020.11.06.20214734.

[3] “Eye anatomy, illustration - Stock Image - F026/6747 - Science Photo Library.” https://www.sciencephoto.com/media/1052245/view/eye-anatomy-illustration (accessed Jun. 26, 2021).

[4] P. Bishop, “The biochemical structure of mammalian vitreous,” in *Eye*, 1996, vol. 10, no. 6, pp. 664–670. doi: 10.1038/eye.1996.159.

[5] P. J. Missel, Y. Ma, B. W. McDonell, D. Shahmirzadi, D. J. K. Abulon, and R. Sarangapani, “Simulation of vitreous traction force and flow rate of high speed dual-pneumatic 7500 cuts per minute vitrectomy probes,” *Transl Vis Sci Technol*, vol. 9, no. 8, pp. 1–15, Jul. 2020, doi: 10.1167/TVST.9.8.46.

[6] J. P. Hubschman, A. Gupta, D. H. Bourla, M. Culjat, F. Yu, and S. D. Schwartz, “20-, 23-, and 25-Gauge vitreous cutters: Performance and characteristics evaluation,” *Retina*, vol. 28, no. 2, pp. 249–257, Feb. 2008, doi: 10.1097/IAE.0b013e31815ec2b3.

[7] B. Diniz *et al.*, “Analysis of a 23-gauge ultra high-speed cutter with duty cycle control,” *Retina*, vol. 33, no. 5, pp. 933–938, May 2013, doi: 10.1097/IAE.0b013e3182733f38.

[8] D. J. K. Abulon and D. C. Buboltz, “Porcine vitreous flow behavior during high-speed vitrectomy up to 7500 cuts per minute,” *Transl Vis Sci Technol*, vol. 5, no. 1, pp. 7–7, Jan. 2016, doi: 10.1167/tvst.5.1.7.

[9] T. D. Ngo, A. Kashani, G. Imbalzano, K. T. Q. Nguyen, and D. Hui, “Additive manufacturing (3D printing): A review of materials, methods, applications and challenges,” *Composites Part B: Engineering*, vol. 143. Elsevier Ltd, pp. 172–196, Jun. 15, 2018. doi: 10.1016/j.compositesb.2018.02.012.

[10] M. A. E. Saleh and A. E. Ragab, “Ti-6 Al-4 V Helical Spring Manufacturing via SLM : Effect of Geometry on Shear Modulus,” 2013.

[11] K. J. DeLaurentis, J. Won, and M. Alam, “Fabrication of Non-Assembly Mechanisms and Robotic Systems Using Rapid Prototyping,” 2001, doi: 10.1115/1.1415034.

[12] K. Lussenburg, A. Sakes, and P. Breedveld, “Design of non-assembly mechanisms: A state-of-the-art review,” *Additive Manufacturing*, vol.

39. Elsevier B.V., p. 101846, Mar. 01, 2021. doi: 10.1016/j.addma.2021.101846.

[13] http://fyra.io, "Achieving High-performance Vitrectomy With Smaller-diameter Systems - Retina Today", Accessed: Aug. 14, 2021. [Online]. Available: https://retinatoday.com/articles/2008-july/0708_17-php

[14] Y. Wei, Y. Chen, Y. Yang, and Y. Li, "Novel design and 3-D printing of nonassembly controllable pneumatic robots," *IEEE/ASME Transactions on Mechatronics*, vol. 21, no. 2, pp. 649–659, Apr. 2016, doi: 10.1109/TMECH.2015.2492623.

[15] M. J. Stolk and K. Lussenburg, "Development of a non-assembly 3D printed driving mechanism for a vitreous cutter," Sep. 2020.

[16] P. R. C. de Oliveira, A. R. Berger, and D. R. Chow, "Vitreoretinal instruments: vitrectomy cutters, endoillumination and wide-angle viewing systems," *International Journal of Retina and Vitreous 2016 2:1*, vol. 2, no. 1, pp. 1–15, Dec. 2016, doi: 10.1186/S40942-016-0052-9.

[17] M.J. Stolk and K. Lussenburg, "Driving Mechanisms of Vitreous Cutters," 2020.

[18] U. Spandau and H. Heimann, "Practical Handbook for Small-Gauge Vitrectomy," *Practical Handbook for Small-Gauge Vitrectomy*, 2018, doi: 10.1007/978-3-319-89677-9.

[19] "Disposable High Speed TDC Cutter 27G / 8000 CPM DORC Continuum range - D.O.R.C. Dutch Ophthalmic Research Center |." https://dorcglobal.com/product/disposable-high-speed-tdc-cutter-27g-8000-cpm-dorc-continuum-range (accessed Nov. 14, 2021).

[20] "EVA UPGRADED*: Phaco-Vitrectomy system that maximizes surgeon control - D.O.R.C. Dutch Ophthalmic Research Center |." https://dorcglobal.com/eva (accessed Nov. 14, 2021).

[21] G. W. Aylward, "25th RCOphth Congress, President's Session paper: 25 years of progress in vitreoretinal surgery," *Eye 2014 28:9*, vol. 28, no. 9, pp. 1053–1059, Jul. 2014, doi: 10.1038/EYE.2014.142.

[22] M. Juraeva, D. J. Song, and D. J. Kang, "Optimum Design of the Dental Air-Turbine Handpiece System Using the Design of Experiment Method," *International Journal of Precision Engineering and Manufacturing*, vol. 21, no. 2, pp. 265–272, Feb. 2020, doi: 10.1007/s12541-019-00294-8.

[23] "patent pneumatic tattoo pen".

[24] R. Shams, "Dynamic measurement of the torque-speed characteristics of dental high speed air turbine handpieces," *Aust Dent J*, vol. 39, no. 1, pp. 33–38, 1994, doi: 10.1111/j.1834-7819.1994.tb05544.x.

[25] A. Zapciu, C. G. Amza, C. Rontescu, and G. Tasca, "3D-Printed, Non-assembly, Pneumatically Actuated Mechanisms from Thermoplastic Materials," *Materiale Plastice*, vol. 55, pp. 517–520, Dec. 2018, doi: 10.37358/mp.18.4.5065.

[26] R. Maccurdy, R. Katzschmann, Y. Kim, and D. Rus, "Printable Hydraulics: A Method for Fabricating Robots by 3D Co-Printing Solids and Liquids," 2016. Accessed: Jun. 27, 2021. [Online]. Available: http://hdl.handle.net/1721.1/103072http://creativecommons.org/licenses/by-nc-sa/4.0/

[27] I. Lazar. Krivts and G. Vladimir. Krejnin, "Pneumatic actuating systems for automatic equipment : structure and design," 2006, Accessed: Oct. 12, 2021. [Online]. Available: https://books.google.com/books/about/Pneumatic_Actuating_Systems_for_Automati.html?hl=nl&id=LkErBgAAQBAJ

[28] J. Wang *et al.*, "3D-printed peristaltic microfluidic systems fabricated from thermoplastic elastomer," *Microfluid Nanofluidics*, vol. 21, no. 6, Jun. 2017, doi: 10.1007/S10404-017-1939-Y.

[29] M. Vázquez, E. Brockmeyer, R. Desai, C. Harrison, and S. E. Hudson, "3D Printing Pneumatic Device Controls with Variable Activation Force Capabilities," *undefined*, vol. 2015-April, pp. 1295–1304, Apr. 2015, doi: 10.1145/2702123.2702569.

[30] G. Weisgrab, A. Ovsianikov, and P. F. Costa, "Functional 3D Printing for Microfluidic Chips," *Adv Mater Technol*, vol. 4, no. 10, p. 1900275, Oct. 2019, doi: 10.1002/ADMT.201900275.

[31] M. Schubert, S. Friedrich, K. Bock, D. Wedekind, S. Zaunseder, and H. Malberg, "European Microelectronics Packaging Conference 3D printed flexible substrate with pneumatic driven electrodes for health monitoring", Accessed: Aug. 14, 2022. [Online]. Available: www.empc2017.pl

[32] A. P. Taylor and L. F. Velásquez-García, "Miniaturized diaphragm vacuum pump by

multi-material additive manufacturing," *Journal of Microelectromechanical Systems*, vol. 26, no. 6, pp. 1316–1326, Dec. 2017, doi: 10.1109/JMEMS.2017.2743020.

[33] G. Dämmer, S. Gablenz, A. Hildebrandt, and Z. Major, "PolyJet-printed bellows actuators: Design, structural optimization, and experimental investigation," *Frontiers Robotics AI*, vol. 6, no. MAY, p. 34, May 2019, doi: 10.3389/frobt.2019.00034.

[34] X. Sheng, H. Xu, N. Zhang, N. Ding, X. Zhu, and G. Gu, "Multi-material 3D printing of caterpillar-inspired soft crawling robots with the pneumatically bellow-type body and anisotropic friction feet," *Sensors and Actuators A*, vol. 316, p. 112398, 2020, doi: 10.1016/j.sna.2020.112398.

[35] B. Sparrman *et al.*, "Printed silicone pneumatic actuators for soft robotics," *Addit Manuf*, vol. 40, p. 101860, 2021, doi: 10.1016/j.addma.2021.101860.

[36] C. Tawk, G. M. Spinks, M. in het Panhuis, and G. Alici, "3D Printable Linear Soft Vacuum Actuators: Their Modeling, Performance 3D Printable Linear Soft Vacuum Actuators: Their Modeling, Performance Quantification and Application in Soft Robotic Systems Quantification and Application in Soft Robotic Systems." Accessed: Jun. 17, 2021. [Online]. Available: https://ro.uow.edu.au/eispapers1https://ro.uow.edu.au/eispapers1/3375

[37] C. Zhang *et al.*, "Fluid-driven artificial muscles: bio-design, manufacturing, sensing, control, and applications," *Biodes Manuf*, vol. 4, pp. 123–145, 2021, doi: 10.1007/s42242-020-00099-z.

[38] M. Schaffner, J. A. Faber, L. Pianegonda, P. A. Rühs, F. Coulter, and A. R. Studart, "3D printing of robotic soft actuators with programmable bioinspired architectures," *Nature Communications 2018 9:1*, vol. 9, no. 1, pp. 1–9, Feb. 2018, doi: 10.1038/S41467-018-03216-W.

[39] M. de Volder and D. Reynaerts, "Pneumatic and hydraulic microactuators: A review," *Journal of Micromechanics and Microengineering*, vol. 20, no. 4. IOP Publishing, p. 18, Mar. 19, 2010. doi: 10.1088/0960-1317/20/4/043001.

[40] B. Gorissen, D. Reynaerts, S. Konishi, K. Yoshida, J. W. Kim, and M. de Volder, "Elastic Inflatable Actuators for Soft Robotic Applications," *Advanced Materials*, vol. 29, no. 43. Wiley-VCH Verlag, p. 1604977, Nov. 20, 2017. doi: 10.1002/adma.201604977.

[41] J. Z. Gul *et al.*, "3D printing for soft robotics – a review," *http://www-tandfonline-com.tudelft.idm.oclc.org/action/journalInformation?show=aimsScope&journalCode=tsta20#.VmBmuzZFCUk*, vol. 19, no. 1, pp. 243–262, Dec. 2018, doi: 10.1080/14686996.2018.1431862.

[42] D. Yang *et al.*, "Buckling Pneumatic Linear Actuators Inspired by Muscle," *Adv Mater Technol*, vol. 1, no. 3, Jun. 2016, doi: 10.1002/ADMT.201600055.

[43] F. Schmitt, O. Piccin, L. Barbé, and B. Bayle, "Soft Robots Manufacturing: A Review," *Front Robot AI*, vol. 0, no. JUN, p. 84, 2018, doi: 10.3389/FROBT.2018.00084.

[44] J. Walker *et al.*, "Soft Robotics: A Review of Recent Developments of Pneumatic Soft Actuators," *Actuators 2020, Vol. 9, Page 3*, vol. 9, no. 1, p. 3, Jan. 2020, doi: 10.3390/ACT9010003.

[45] "BELLOWS DESIGN - breathney.vub.be." https://breathney.vub.be/nl/bellow-design/ (accessed Jun. 30, 2021).

[46] M. di Giovanni, *Flat and corrugated diaphragm design handbook*. M. Dekker, 1982.

[47] M. Aurisicchio, R. Bracewell, and G. Armstrong, "DETC2012-70944 THE FUNCTION ANALYSIS DIAGRAM," 2012. [Online]. Available: http://www.asme.org/about-asme/terms-of-use

[48] "Advanced ULTRAVIT® Beveled High Speed Probe | MyAlcon Professional." https://professional.myalcon.com/vitreoretinal-surgery/vitrectomy-platforms-and-probes/ultravit-bevel-tip-probe/ (accessed Aug. 11, 2022).

[49] J. Schuurman, "Improvements on a Dual Diaphragm Driving Mechanism used in a Non-Assembly Vitrectome," 2021.

[50] F. Ulu, R. P. S. Tomar, and R. Mohan, "Processing and mechanical behavior of rigid and flexible material composite systems formed via voxel digital design in polyjet additive manufacturing," *Rapid Prototyp J*, vol. 27, no. 3, pp. 617–626, Apr. 2021, doi: 10.1108/RPJ-06-2020-0119.

[51] "DIA·COM CORPORATION DIA·COM CORPORATION The Diaphragm Company Diaphragm Design Guidebook," 2018. Accessed: Jun. 07, 2021. [Online]. Available: www.diacom.com

[52] "The Shape Optimization of the Pneumatic Valve Diaphragms." Accessed: Jun. 06, 2021. [Online]. Available: https://www.naun.org/main/NAUN/mcs/20-849.pdf

[53] D. Robijns, K. Lussenburg, and P. Breedveld, "Mechanical spring design for additive manufacturing A design review," 2021.

[54] Larry L. Howell *et al.*, "Compliant, ortho-planar, linear motion spring," Apr. 2001.

[55] Parise J.J, John J, L. L. Howell, and S. P. Magleby, "Ortho-planar linear-motion springs." [Online]. Available: www.elsevier.com/locate/mechmt

[56] C. Thurnherr, L. Ruppen, G. Kress, and P. Ermanni, "Non-linear stiffness response of corrugated laminates in tensile loading," *Compos Struct*, vol. 157, pp. 244–255, Dec. 2016, doi: 10.1016/j.compstruct.2016.08.038.

[57] "Vero Family (Rigid) | Stratasys™ Support Center." https://support.stratasys.com/en/materials/polyjet/vero-family (accessed Aug. 17, 2022).

[58] F. F. Abayazid and M. Ghajari, "Material characterisation of additively manufactured elastomers at different strain rates and build orientations," *Addit Manuf*, vol. 33, p. 101160, May 2020, doi: 10.1016/J.ADDMA.2020.101160.

[59] "Agilus30 - Stratasys." https://www.stratasys.com/en/materials/materials-catalog/polyjet-materials/agilus30/ (accessed Jul. 15, 2022).

[60] "Fused Deposition Modeling | Design Guide - Stratasys." https://www.stratasys.com/en/stratasysdirect/resources/resource-guides/fused-deposition-modeling/ (accessed Jul. 30, 2022).

APPENDIX I BELLOW-DRIVEN DRIVING MECHANISM DESIGN

Bellow configuration

To fit a bellow driving mechanism in the vitreous cutter handle, a large bellow or multiple small bellows can be used, like depicted in Fig. 39 (a) and Fig. 39 (b) respectively. The inner needle passes through the entire length of the device to provide a passage for the vitreous through the device. For a large bellow, this will require the needle to pass through the bellow enclosing an air chamber in order to fungate. Since the working of the bellow is based on the elongation of this air chamber, the needle needs to be fixed on one side of the bellow and should be movable on the other side of the bellow. As a result, the large bellow requires an airtight movable sealing around the needle. For the small bellows on the contrary, the needle does not need to pass through the air chambers. The needle can be attached to a platform that can be driven by the multiple small bellows while allowing a passage for the needle. However, due to the minimal handle size, the bellows are relatively small. Making adding a hole for support removal difficult and only allowing a minimal effective area required to push the bellows forward. A double wall bellow, like depicted in Fig. 39 (c) might offer an outcome. This doughnut-shaped bellow consists of an outer bellow and inner bellow enclosing an air chamber. The double wall bellow allows a passage for the inner needle while still optimal taking advantage of the total available space. Moreover, the double wall bellow can be easily actuated while the multiple small bellows need to be acting exactly similar, so pressurizing synchronously and returning synchronously. Overall the double wall bellow is expected to offer the best solution.

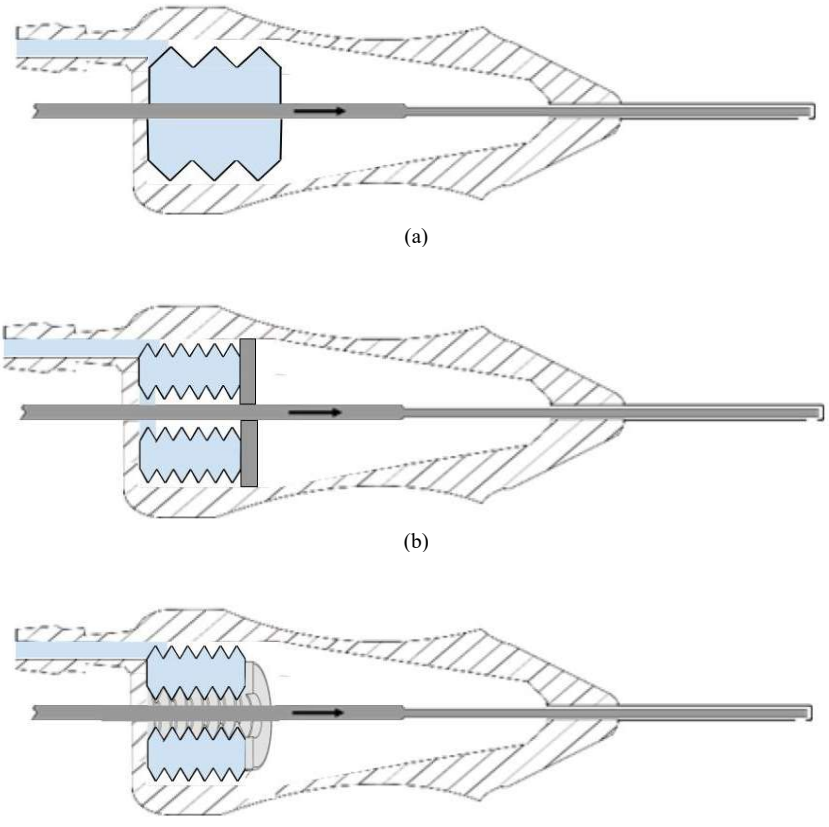

(a)

(b)

(c)

Fig. 39. Graphical visualization possible bellow configurations (a) multiple small bellows (b) one large bellows (c) double wall bellow

Material and AM technique

To print the double wall below multiple materials and techniques can be used. However, failure due to fatigue after repeated loadings forms a concern [33]. A relatively higher lifetime is reported for bellows printed with TPU [36]/[45]. Therefore, it is decided to first explore the possibilities of FDM printing an TPU bellow design. TPU printing with FDM requires an optimization of the printer settings like the layer height, layer width, speed and temperature. The most optimal setting can slightly vary per printer and design. For the first attempt, the optimized printer settings reported by Tawk et al [36] can be used. Due to the restricted access to co-printing of soluble supports, it is first aimed to print a design without requiring support.

Bellow shape

A wide range of possible designs for double wall TPU bellows can be made. The working of bellows is influenced by the design parameters, like the wall thickness, number of corrugations, corrugation depth and hight. Increasing the number and height of the corrugations and decreasing the thickness, decreases the stiffness of the bellow. On the one hand, stiffness is required to allow the minimal required backward force and additional backward speed. On the other hand, flexibility minimizes the pressure required to drive the needle which allows to faster pressurize the enclosed air chamber in addition to a faster forward motion due to the minimal backward force. The parameters can also influence the lifetime of the bellow. Bellows with a thin printed wall show a significantly higher lifetime [36]. However, thin wall structures are harder to print airtight and are more prone to shrinkage and warping. Overall, the parameters need to be rightly balanced to fulfil all requirements.

Probably multiple iterations are needed before obtaining a suitable bellow. To give a first indication, two bellows are designed, like depicted in Fig. 40. The outer diameter of the bellows is set to 14 mm to allow a maximal size of the bellow while still fitting in the handle of the vitreous cutter. A minimal wall thickness is chosen to increase the durability and allow to fit a double wall bellow into the vitreous cutter handle. A minimal wall thickness of 0.5 mm is chosen considering the FDM guidelines [60]. This thickness is larger than four times the layer height and forms a multitude of the layer width. Two different shapes are selected that might allow printing without support, a circular-based corrugation and a triangular-based corrugation, like depicted in Fig 40 (a) and Fig 40 (c) respectively. The triangular-shaped corrugations have a 50-degree inclination of the walls such that the guidelines for the minimal self-supporting angle are followed. Eliminating the need for support is preferred since it is not known if it would be possible to remove the support out of the bellow through the small air holes. For testing purposes, designs with a different number of corrugations can be made such that the behaviour of different stiffnesses can be researched.

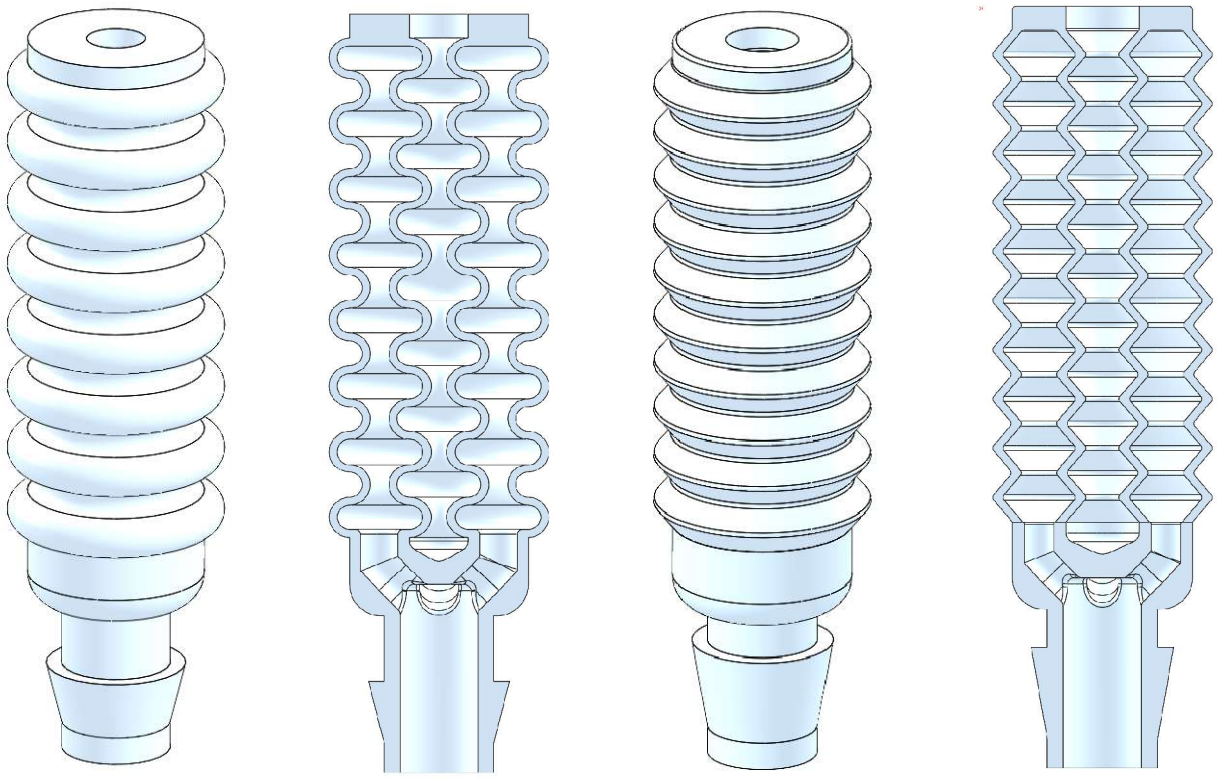

(a) (b) (c) (d)

Fig. 40. 3D model of two possible double wall bellow designs (a) bellow with circular based corrugation (b) cross-section circular based double wall bellow (c) bellow with triangular based corrugation. (d) cross-section triangular based double wall bellow

APPENDIX II PROTOTYPES BATCH 1

The prototypes of batch 1 are used for speed tests and force tests of different spring shapes and thicknesses. The prototypes are produced at TU Delft on a Stratasys PolyJet printer using Vero-yellow and Agilus30. The prototypes are printed with the Agilus30 diaphragm facing the build plate such that the spring is printed on top of the diaphragm. Soluble support is used during printing. The support is partly manually removed and by using a sodium hydroxide solution. The exact dimensions of the prototypes can be found in the following drawings.

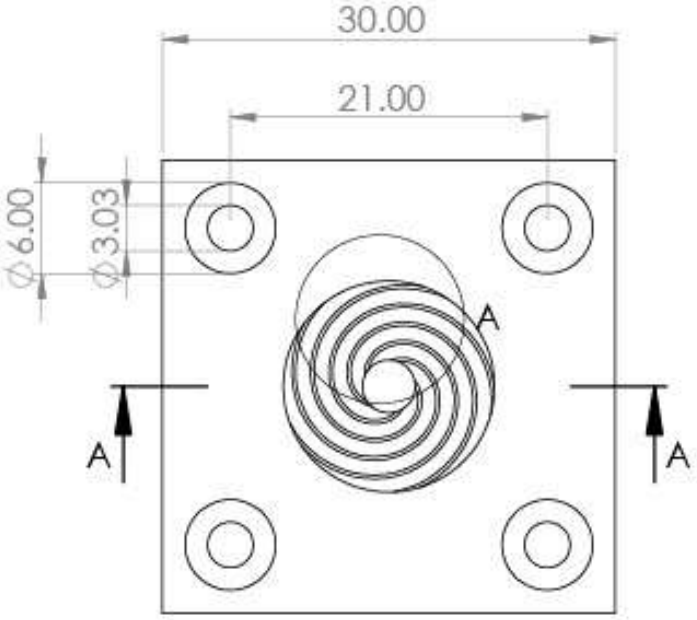

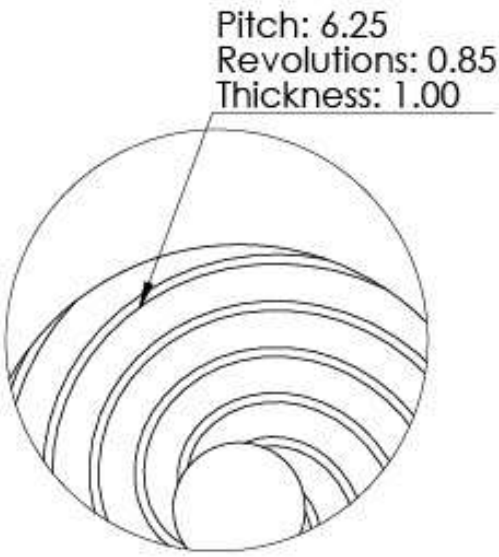

DETAIL A
SCALE 5 : 1

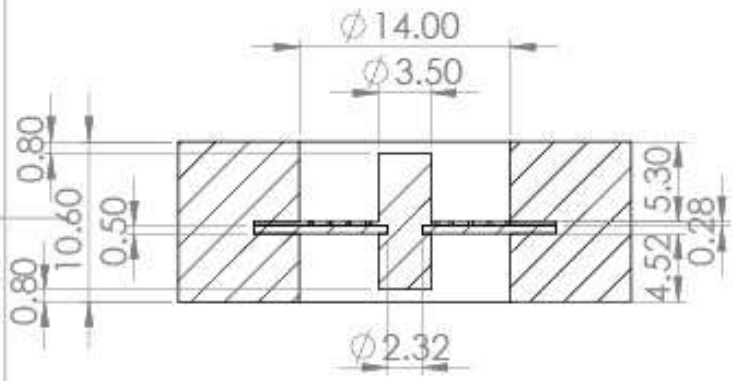

SECTION A-A
SCALE 2 : 1

3D model:

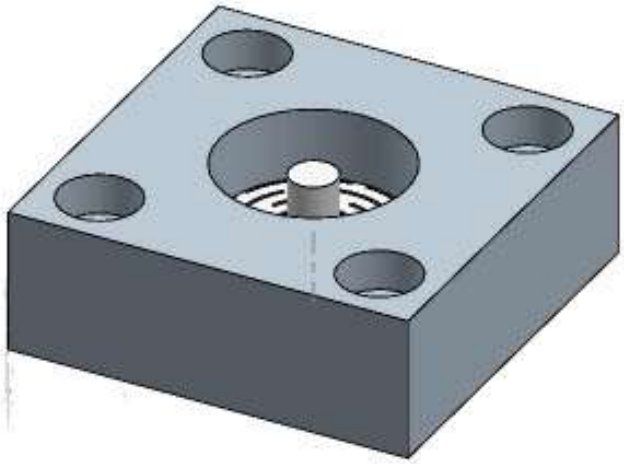

Name:
S0.28

Material:
Vero / Agilus30

Scale:
2:1

Dimensions are in mm **A4**

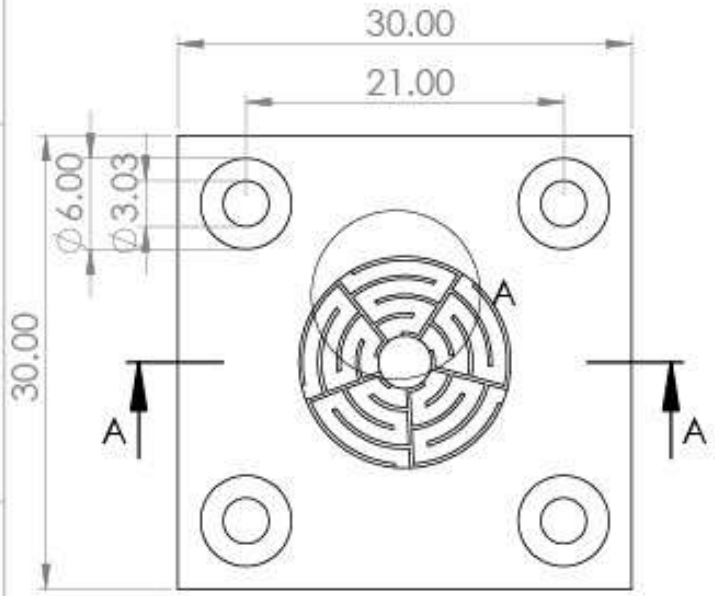

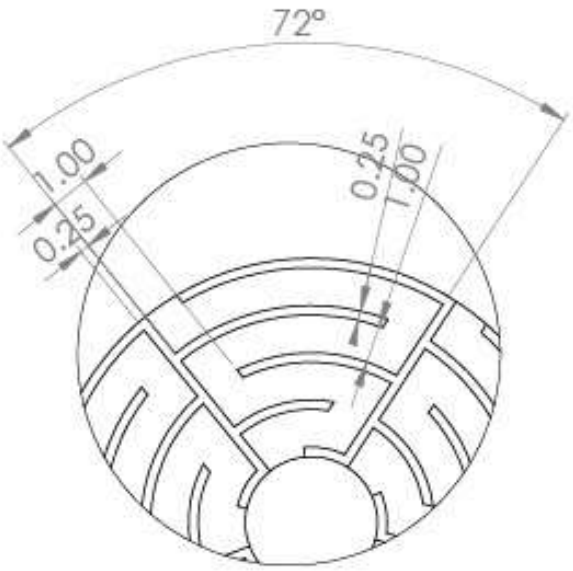

DETAIL A
SCALE 5 : 1

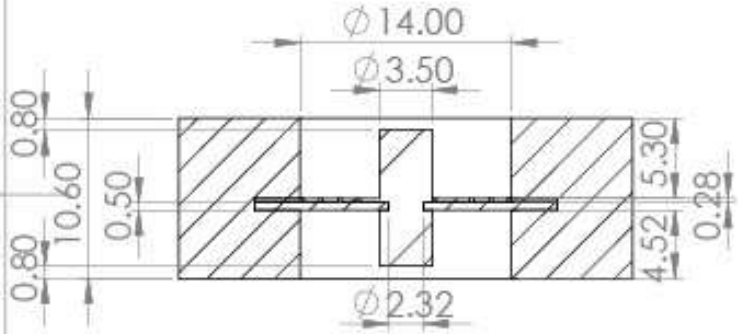

SECTION A-A
SCALE 2 : 1

3D model:

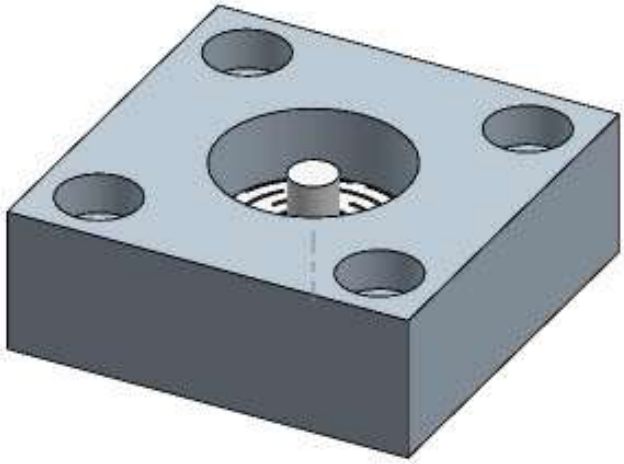

Name:
Z0.28

Material:
Vero / Agilus30

Scale:
2:1

Dimensions are in mm **A4**

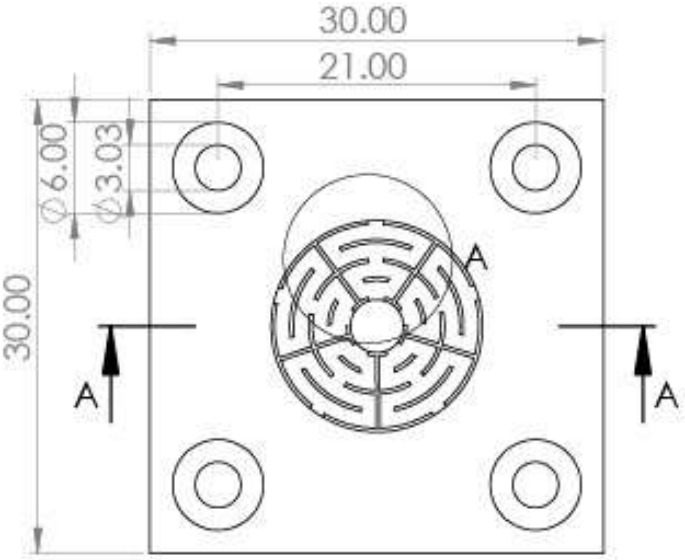

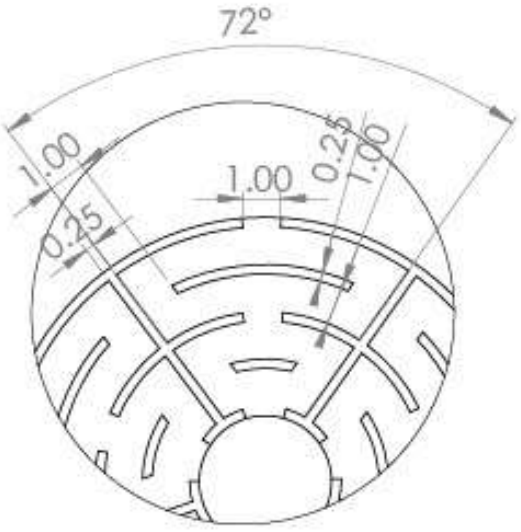

DETAIL A
SCALE 5 : 1

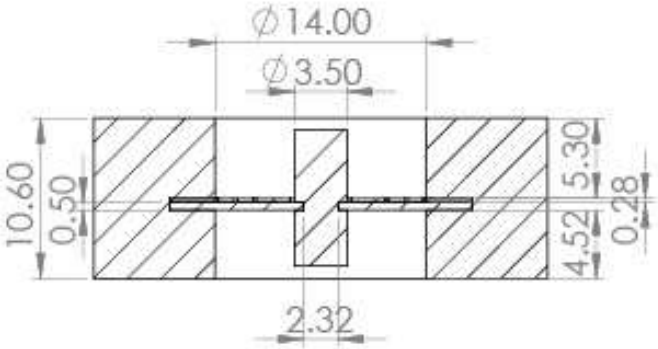

SECTION A-A
SCALE 2 : 1

3D model:

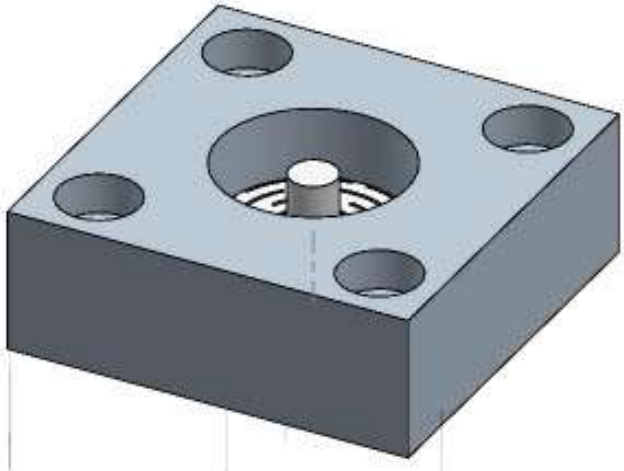

Name:
F0.28

Material:
Vero / Agilus30

Scale:
2:1

Dimensions are in mm **A4**

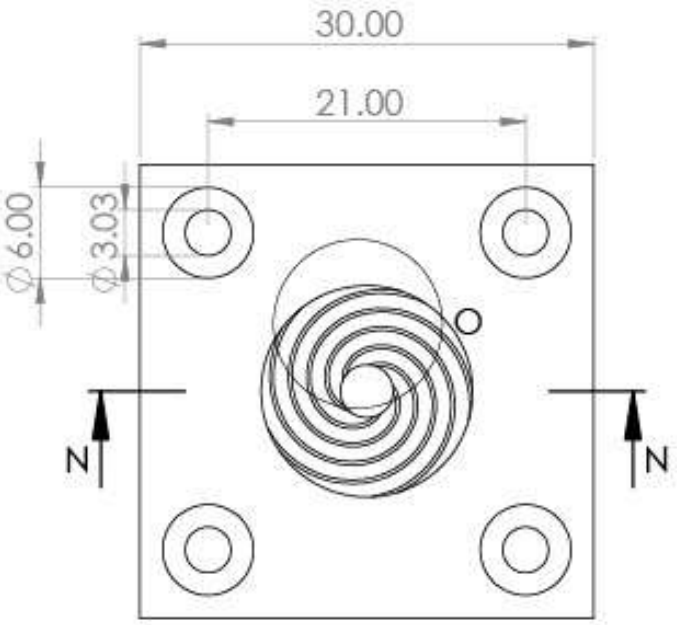

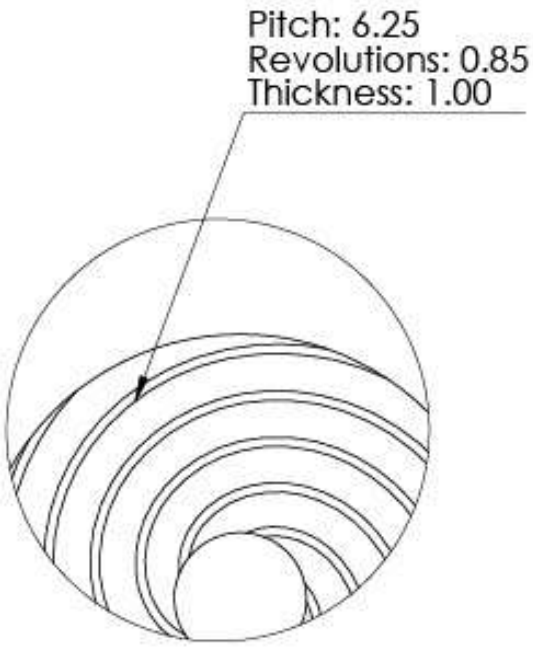

DETAIL O
SCALE 5 : 1

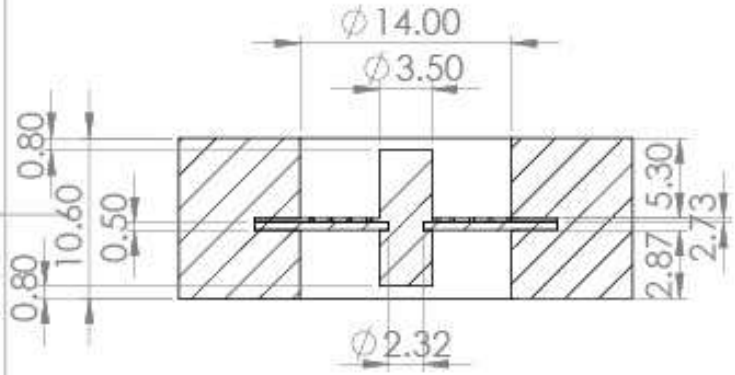

SECTION N-N
SCALE 2 : 1

3D model:

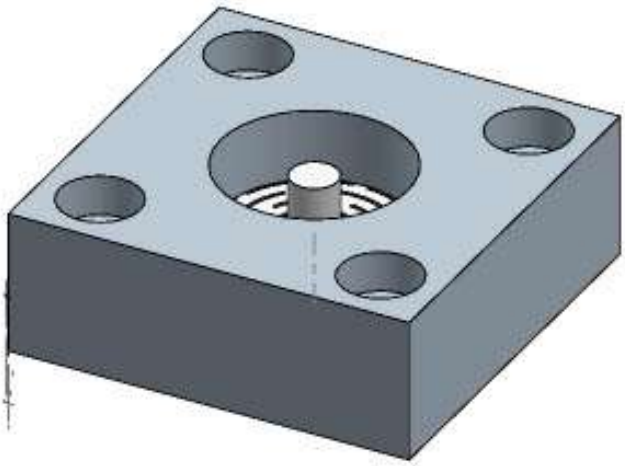

Name:
S2.73

Material:
Vero / Agilus30

Scale:
2:1

Dimensions are in mm **A4**

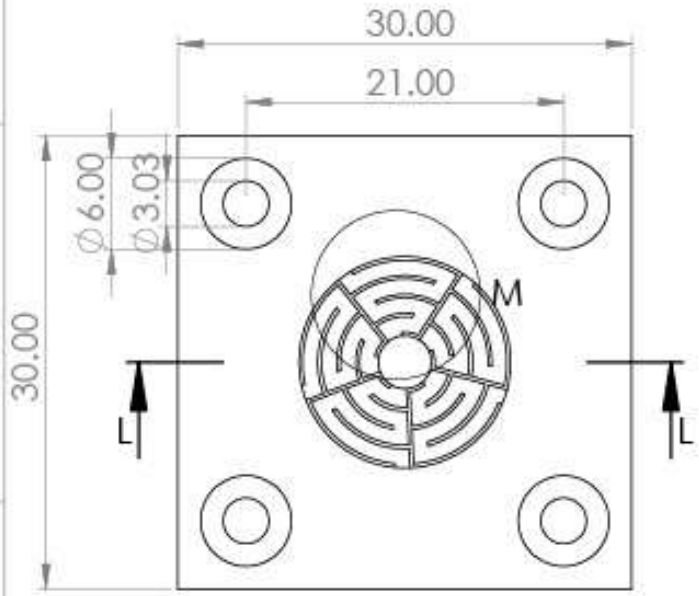

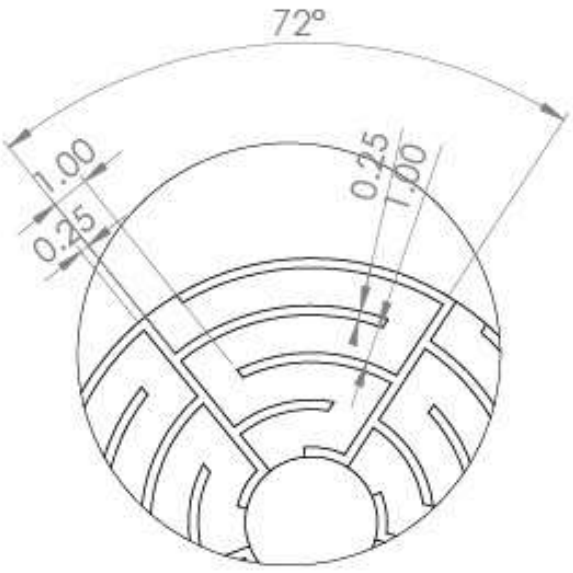

DETAIL M
SCALE 5 : 1

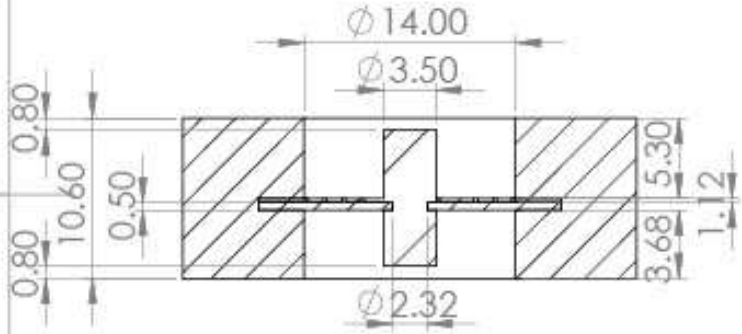

SECTION L-L
SCALE 2 : 1

3D model:

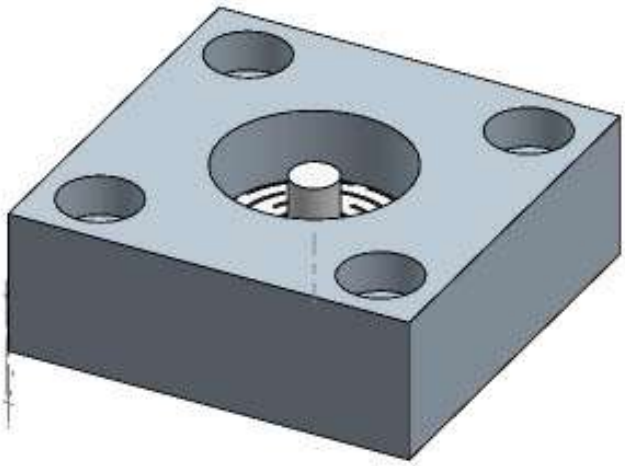

Name:
Z1.12

Material:
Vero / Agilus30

Scale:
2:1

Dimensions are in mm **A4**

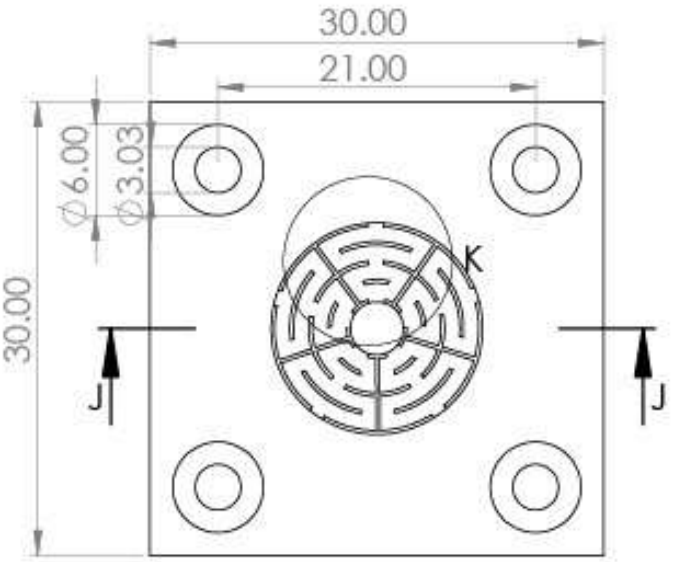

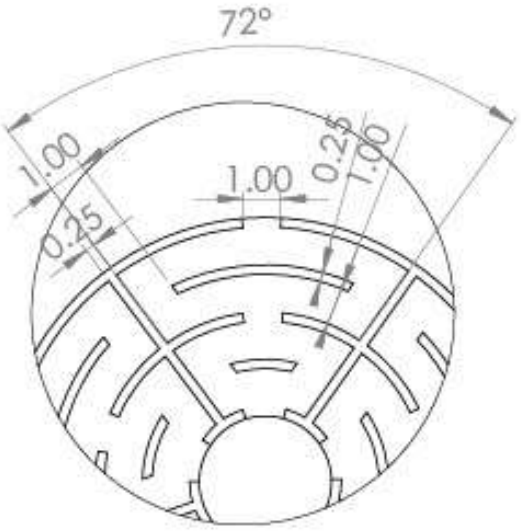

DETAIL K
SCALE 5 : 1

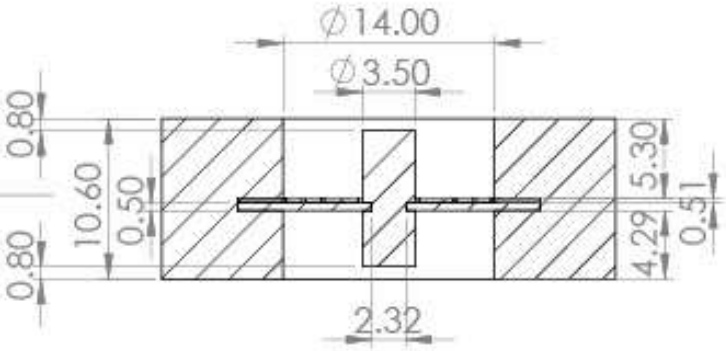

SECTION J-J
SCALE 2 : 1

3D model:

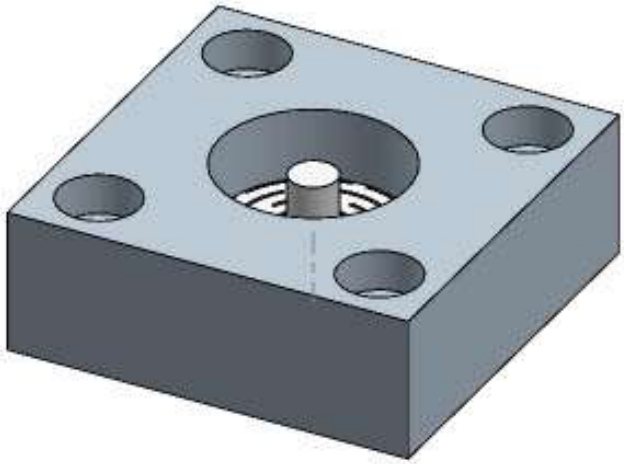

Name:
F0.51

Material:
Vero / Agilus30

Scale:
2:1

Dimensions are in mm **A4**

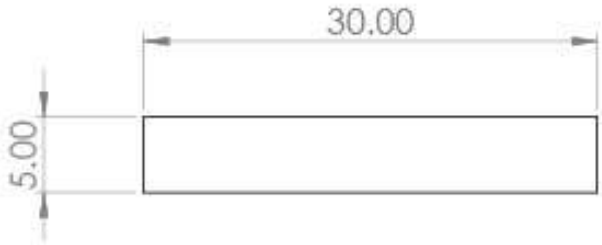

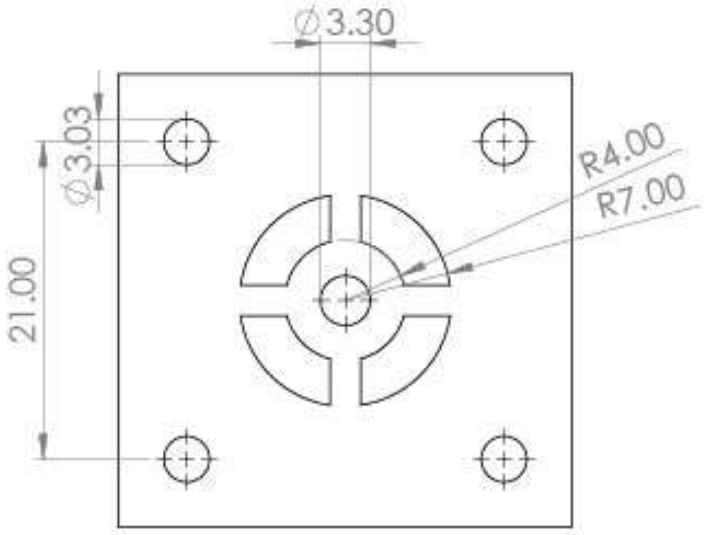

3D model:

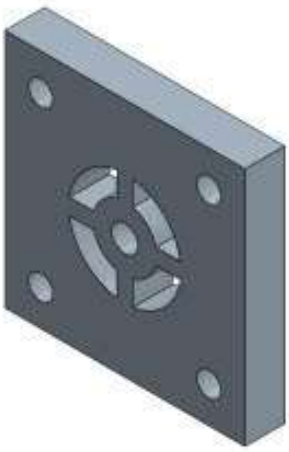

Name:
Stop plate

Material:
Vero

Scale:
2:1

Dimensions are in mm **A4**

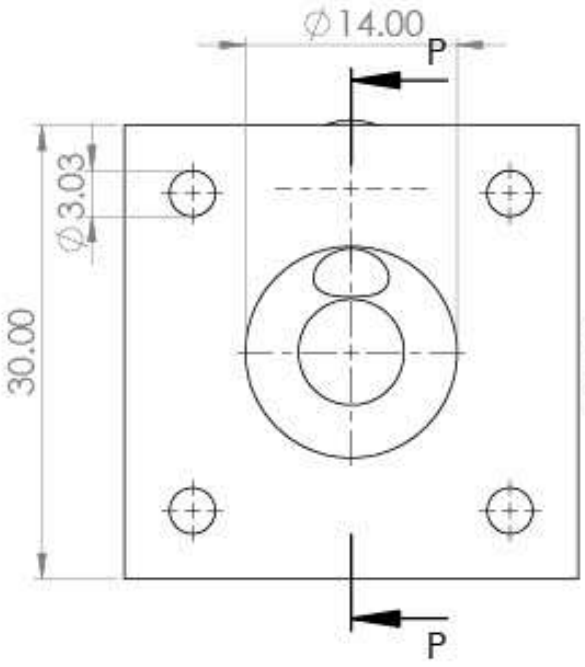

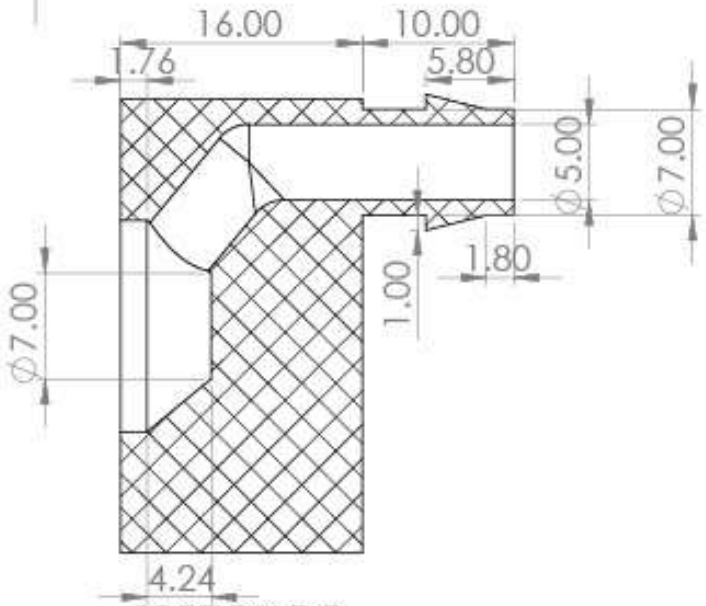

SECTION P-P
SCALE 2 : 1

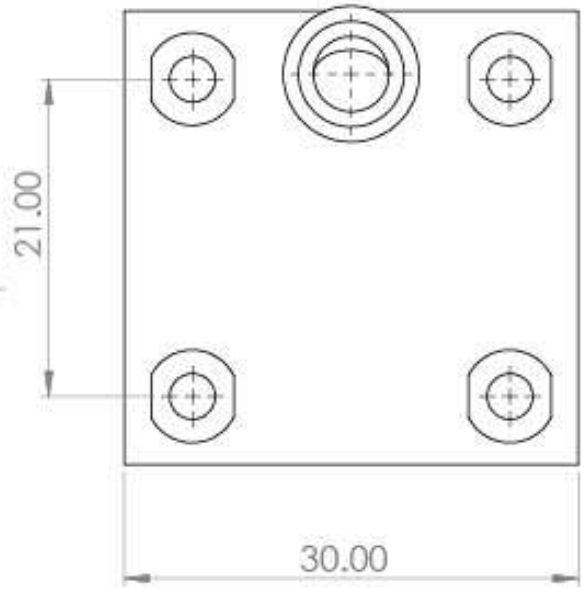

3D model:

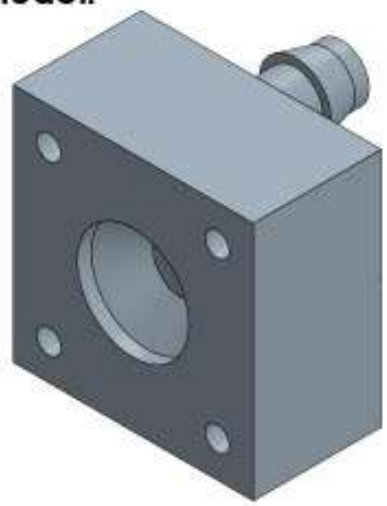

Name:
Air inlet

Material:
Vero

Scale:
2:1

Dimensions are in mm **A4**

APPENDIX III PROTOTYPES BATCH 2

The prototypes of batch 2 are used for speed tests and force tests of different spring thicknesses and relocated start positions. The prototypes are produced by 3D LifePrints on a Stratasys PolyJet printer using Vero-white and Agilus30. The prototypes are printed with the Agilus30 diaphragm facing the build plate such that the spring is printed on top of the diaphragm. Soluble support is used during printing. The support is removed by 3D lifeprints using waterjets according their standards. The exact dimensions of the prototypes can be found in the drawings on the next pages.

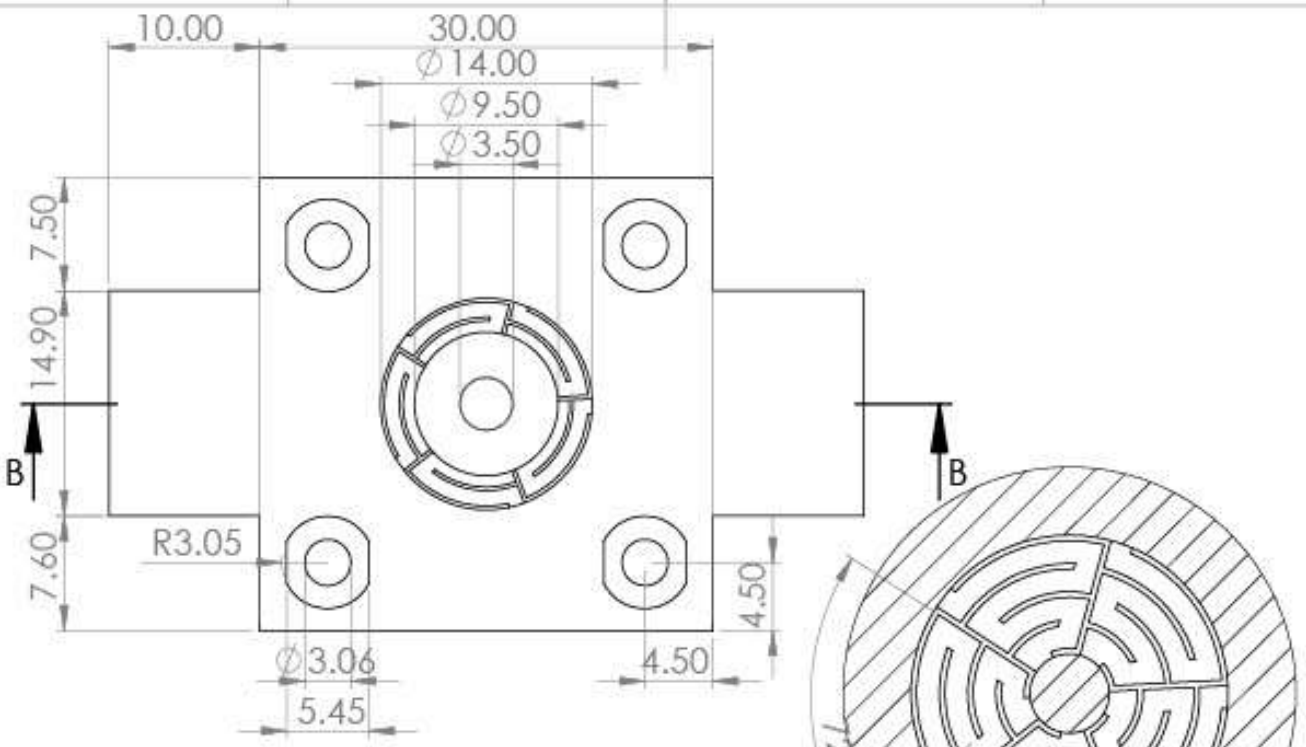

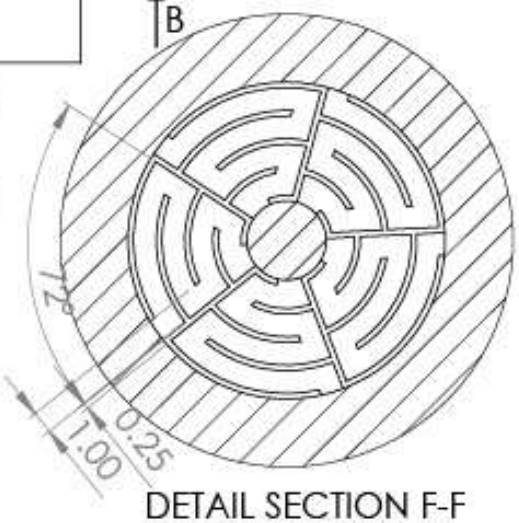

DETAIL SECTION F-F
SCALE 3 : 1

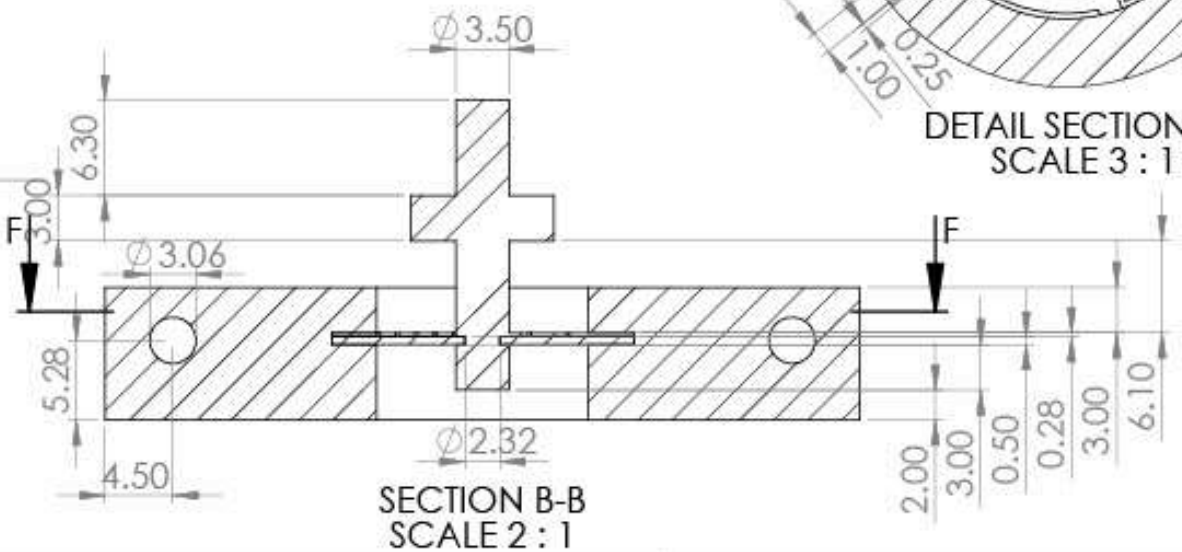

SECTION B-B
SCALE 2 : 1

3D model:

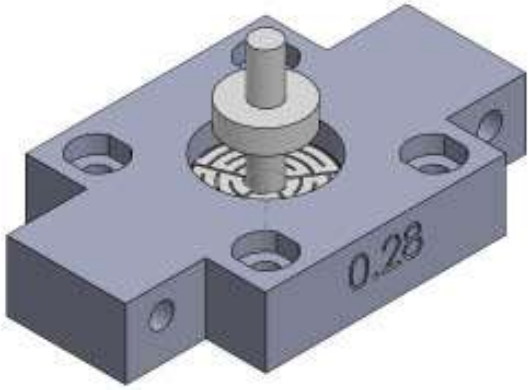

Name:

Z0.28

Material:

Vero / Agilus30

Scale:

2:1

Dimensions are in mm **A4**

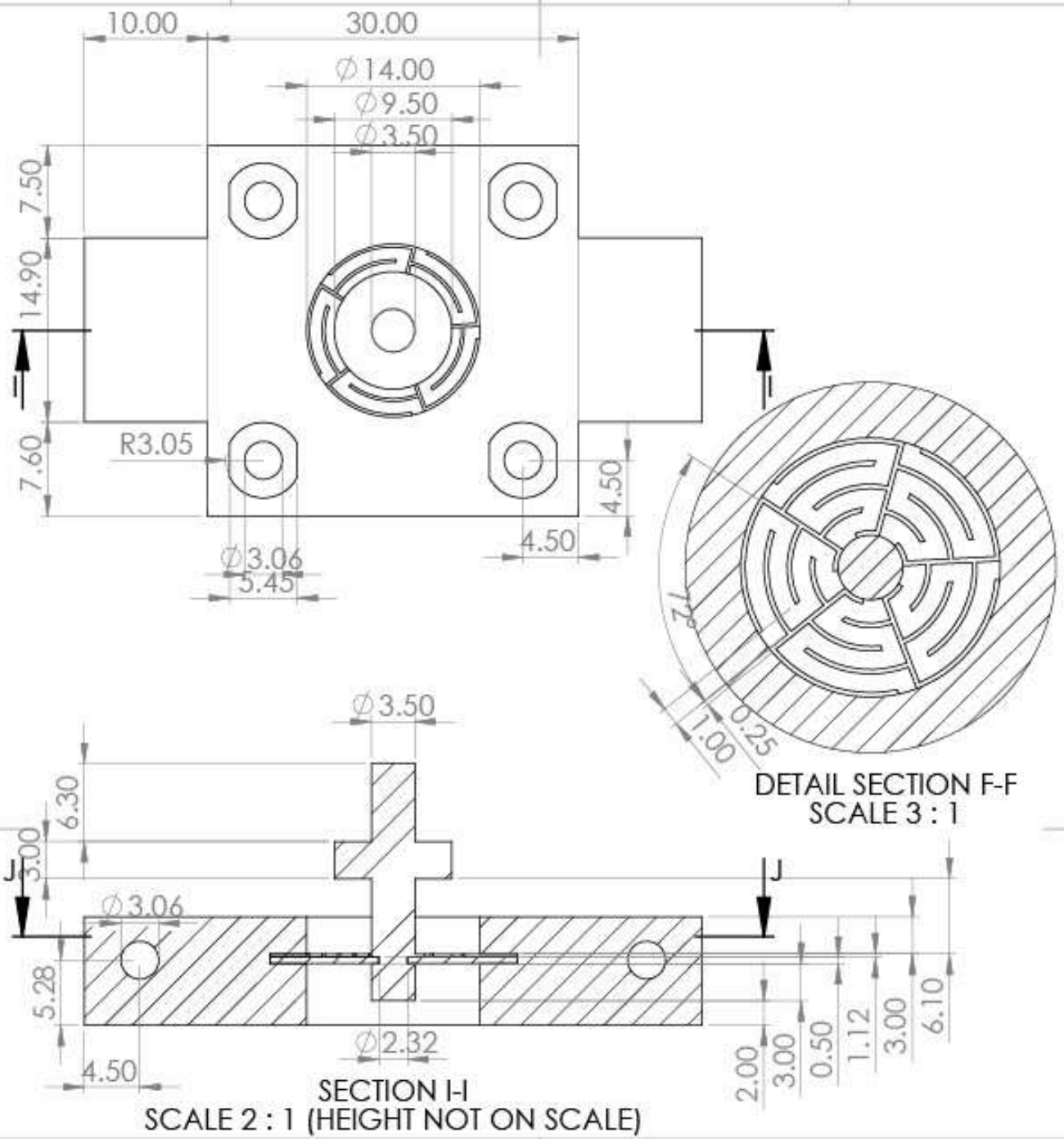

3D model:

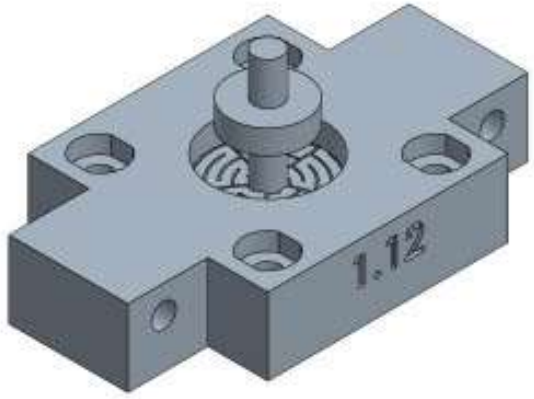

Name:

Z1.12

Material:

Vero / Agilus30

Scale:

2:1

Dimensions are in mm **A4**

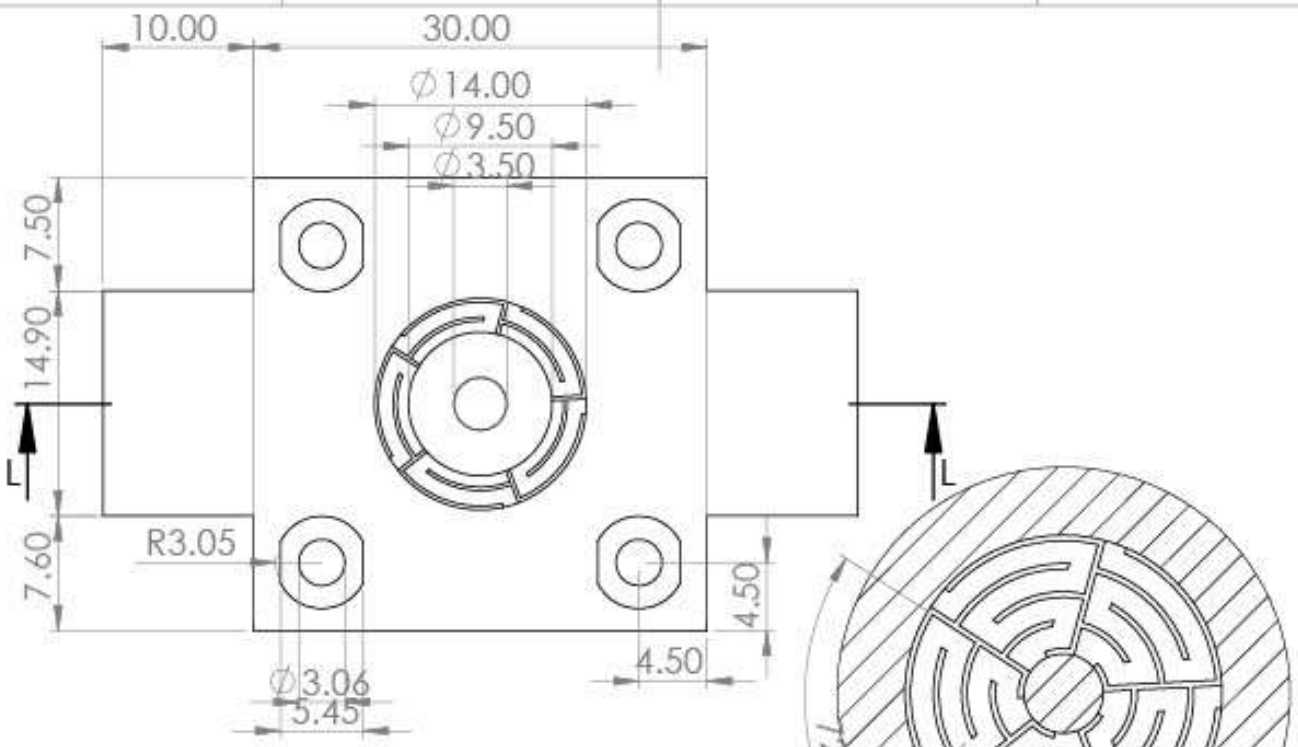

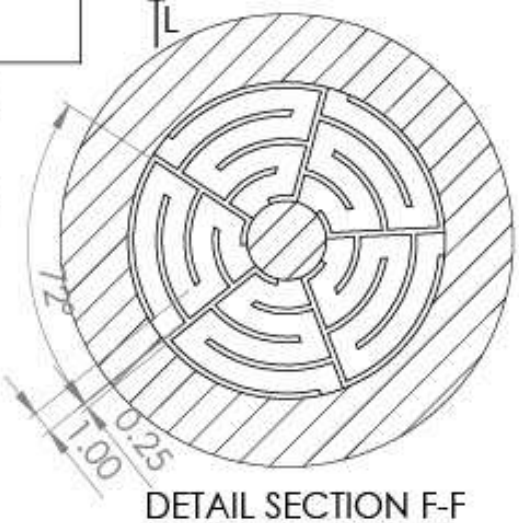

DETAIL SECTION F-F
SCALE 3 : 1

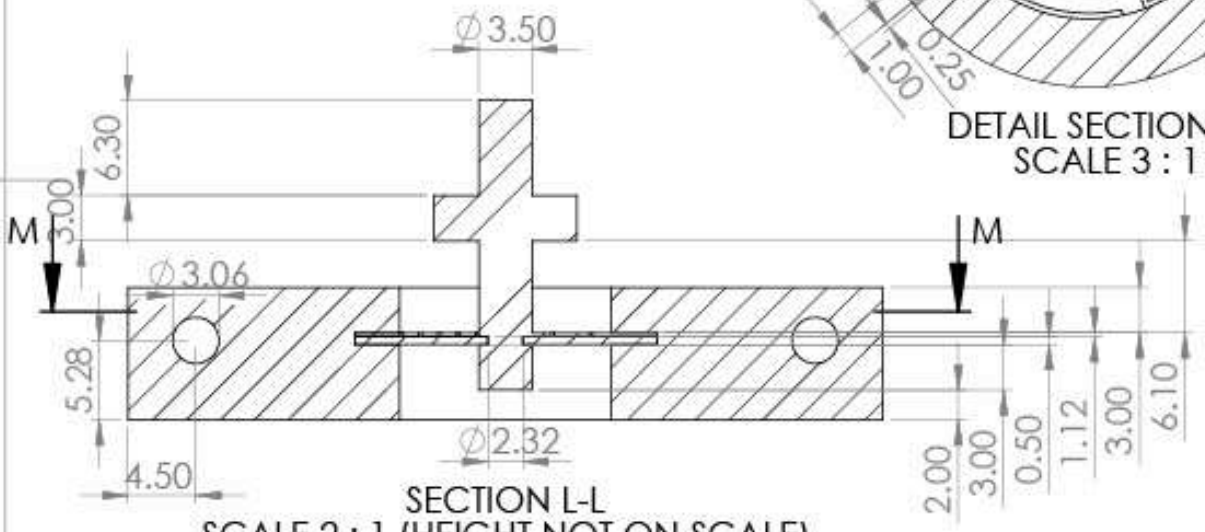

SECTION L-L
SCALE 2 : 1 (HEIGHT NOT ON SCALE)

3D model:

Name:

Z2.24

Material:

Vero / Agilus30

Scale:

2:1

Dimensions are in mm **A4**

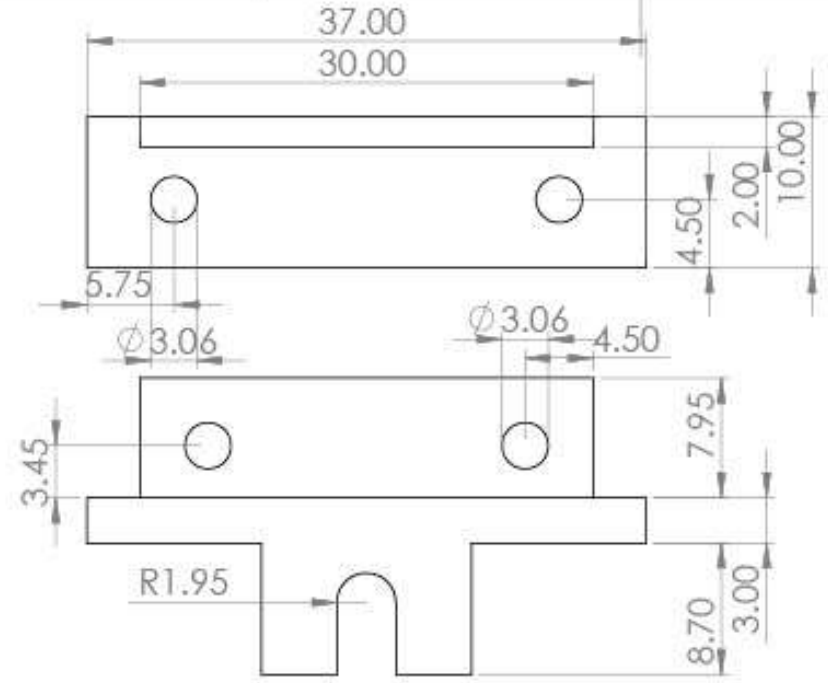

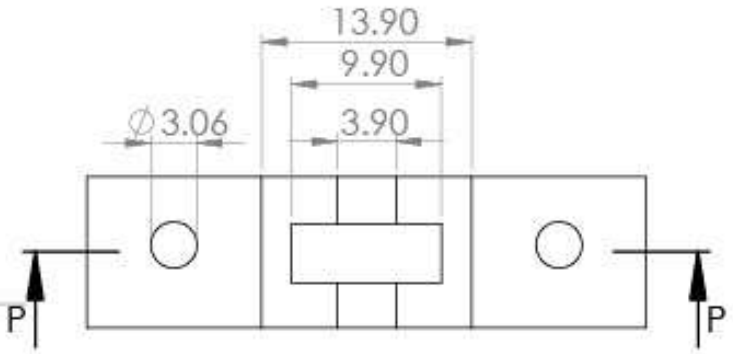

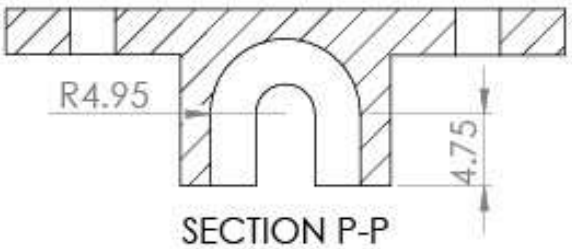

SECTION P-P
SCALE 2 : 1

3D model:

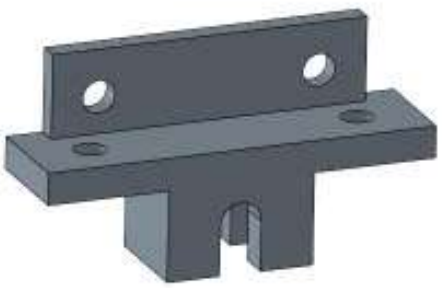

Name:
Pretension part 1

Material:
Vero

Scale:
2:1

Dimensions are in mm **A4**

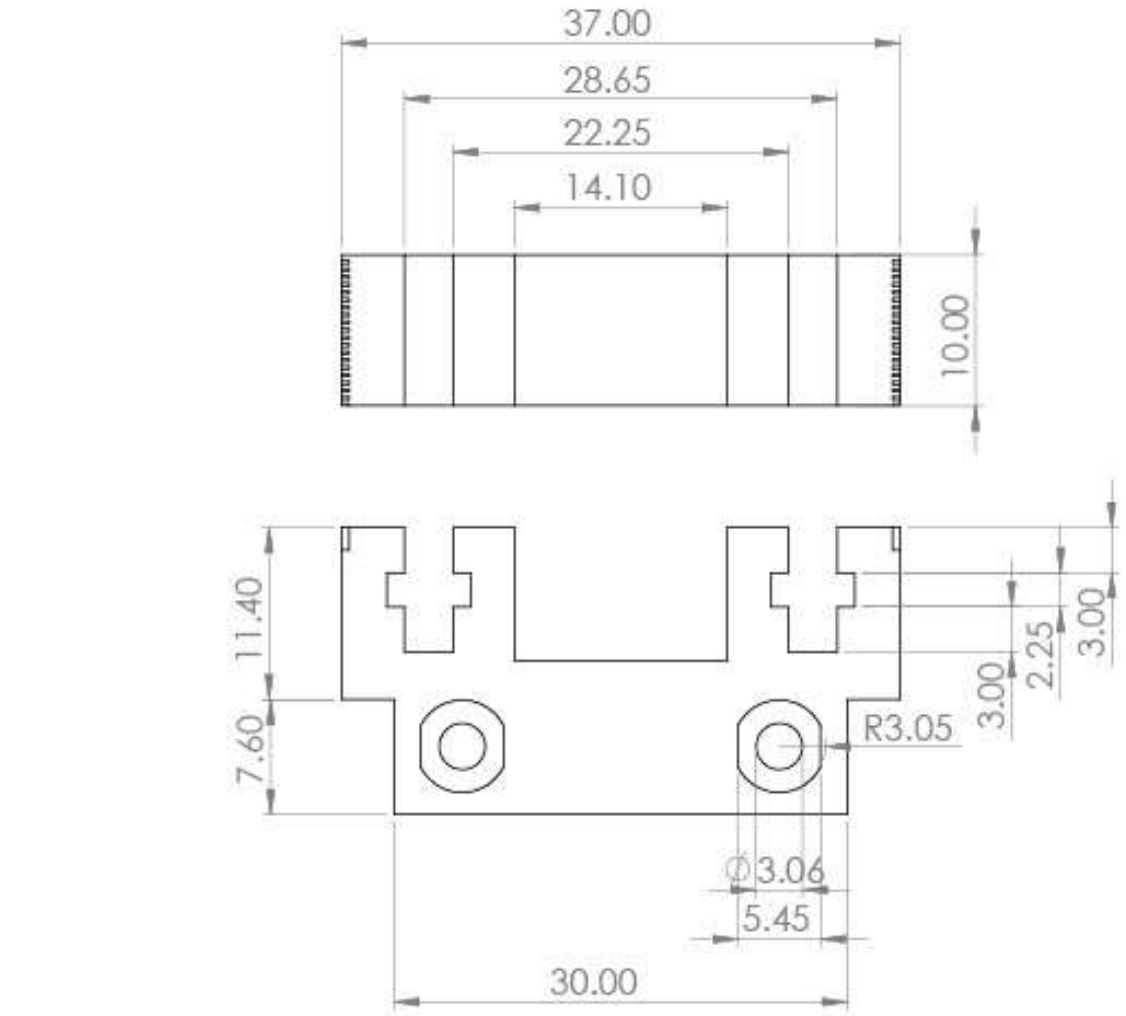

3D model:

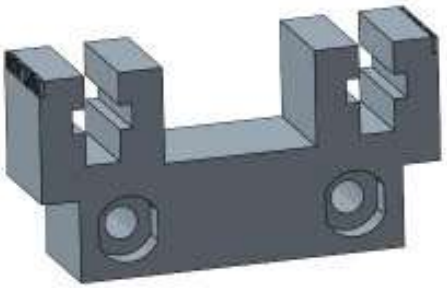

Name:
Pretension Part 2

Material:
Vero

Scale:
2:1

Dimensions are in mm **A4**

APPENDIX IV FIXTURES

The fixtures used for the speed tests and force test are produced at the student workshop of the TU Delft using milling and laser cutting. Steel plates are used for laser cutting and aluminium for the milling. The exact dimensions of all fixtures can be found in the next pages.

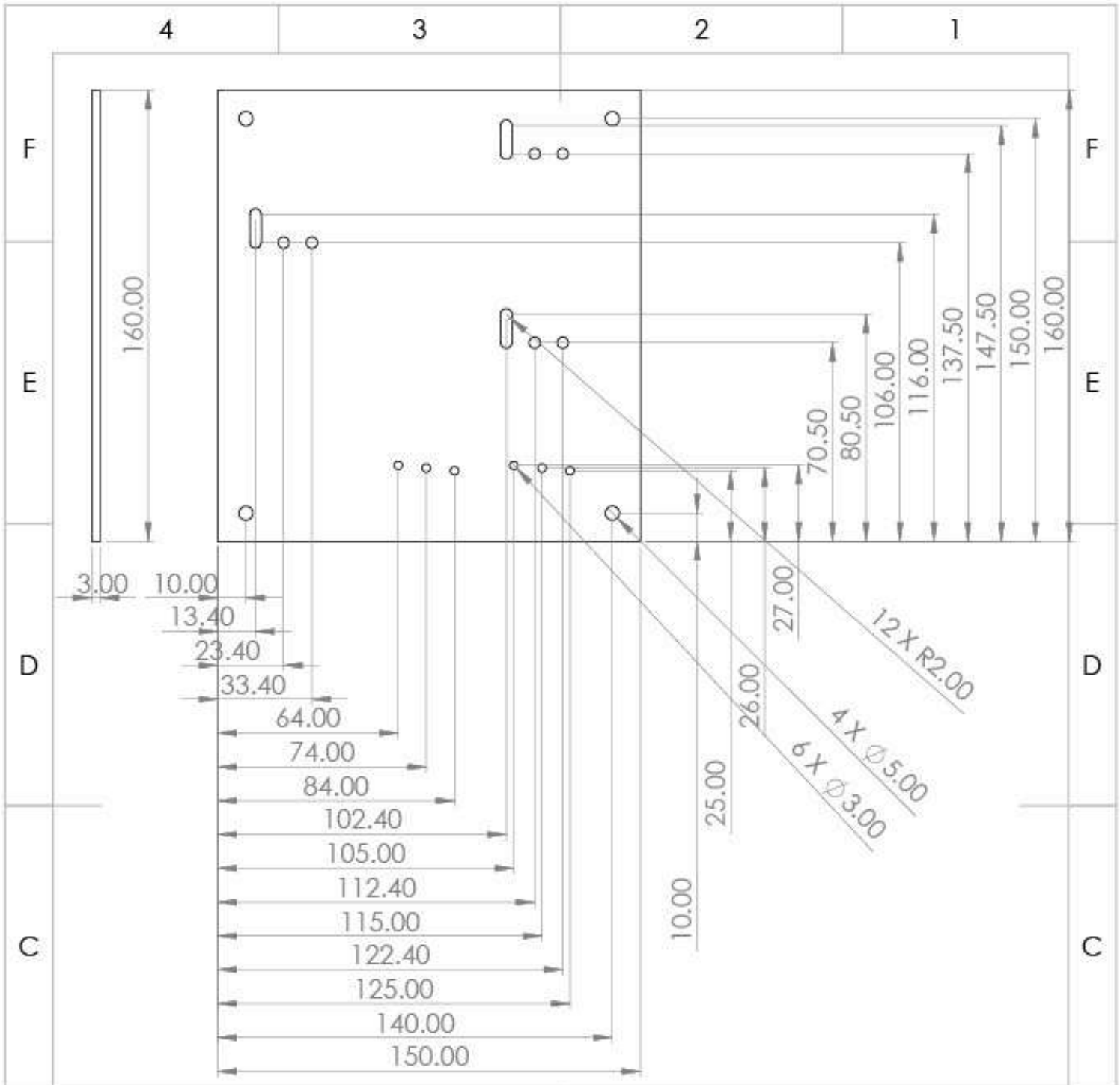

3D model:

Name:

Fixture Micro-Epsilon ILD1750-2 laser

Material:

steel

Scale:

1:2

Dimensions are in mm **A4**

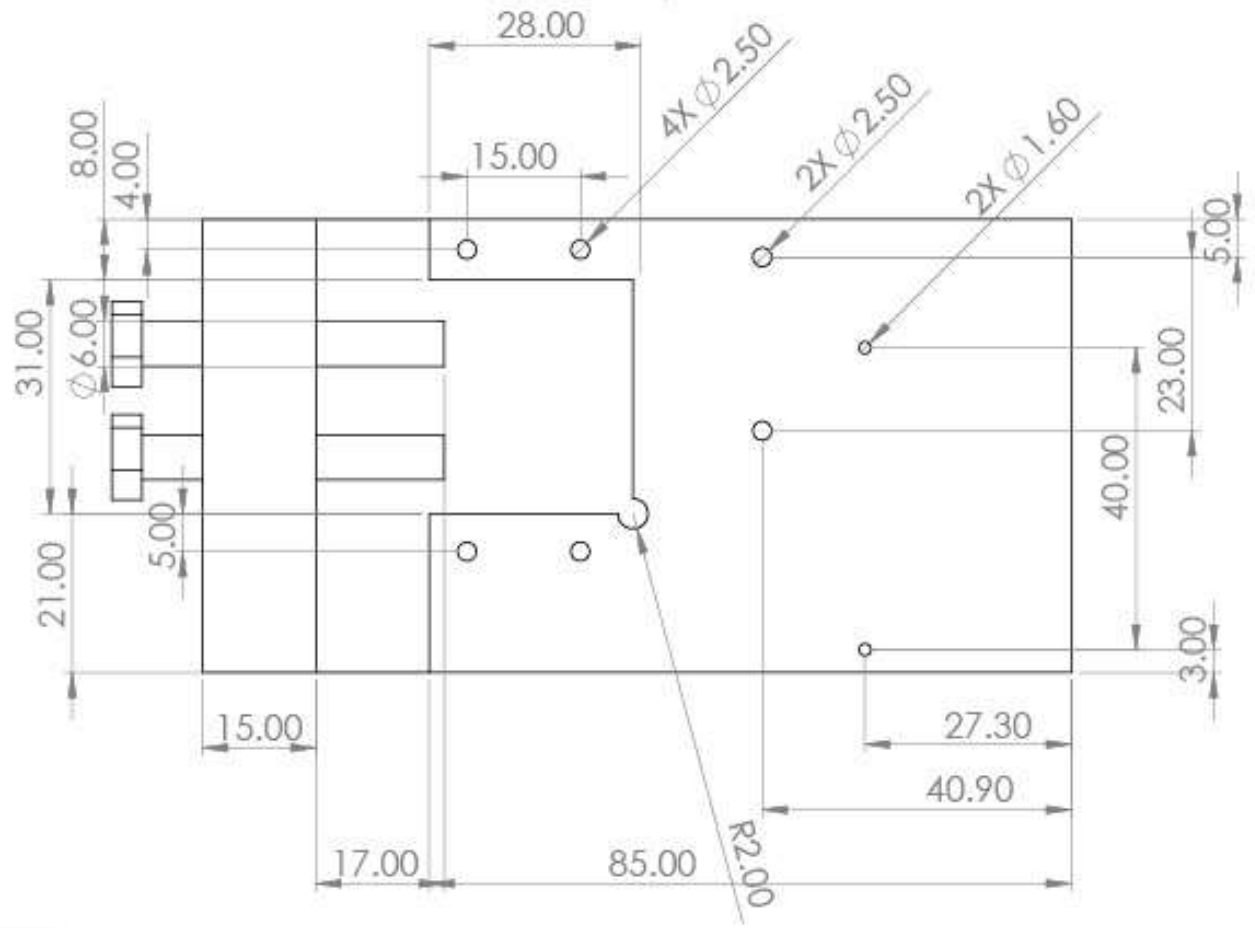

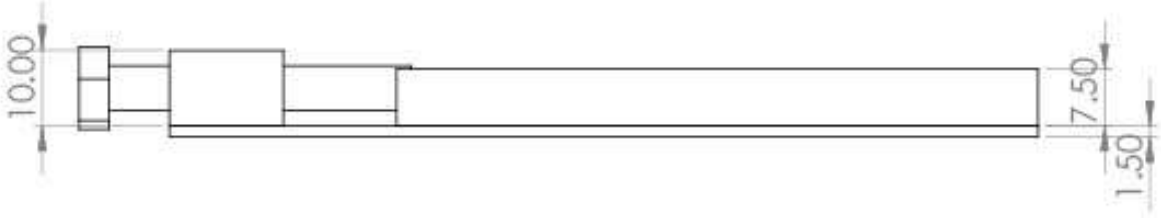

3D model:

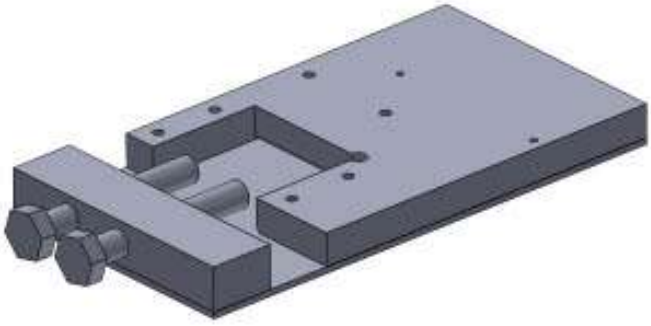

Name:

Fixture Micro-Epsilon ILD142010 laser

Material:

Aliminium + steel plate

Scale:

1:1

Dimensions are in mm **A4**

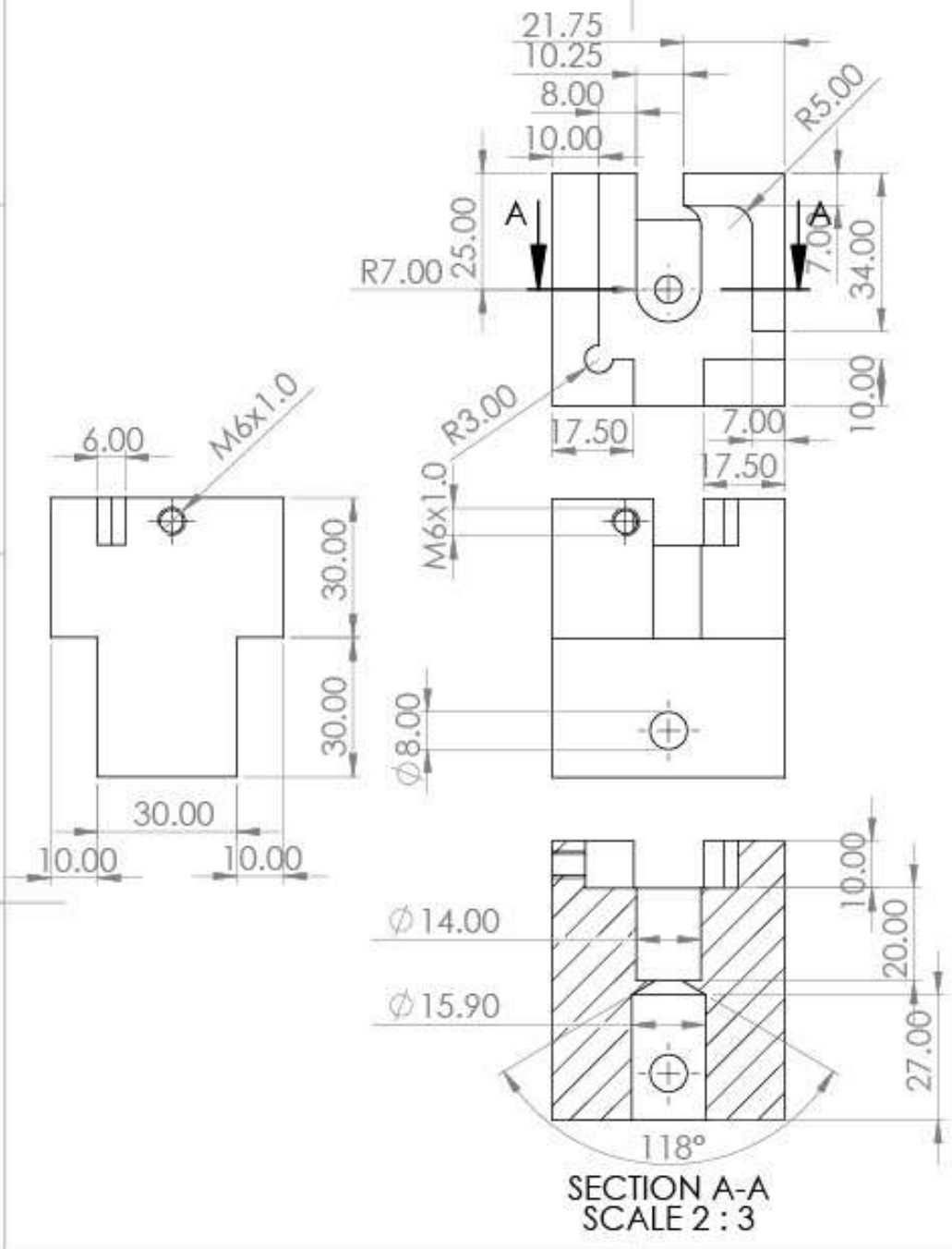

SECTION A-A
SCALE 2 : 3

3D model:

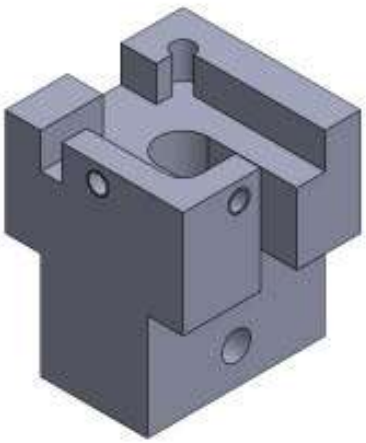

Name:

Fixtire tensile tester

Material:

Aluminium

Scale:

2:3

Dimensions are in mm **A4**

APPENDIX V LABVIEW PROGRAM MICRO EPSILON ILD1420-10 LASER

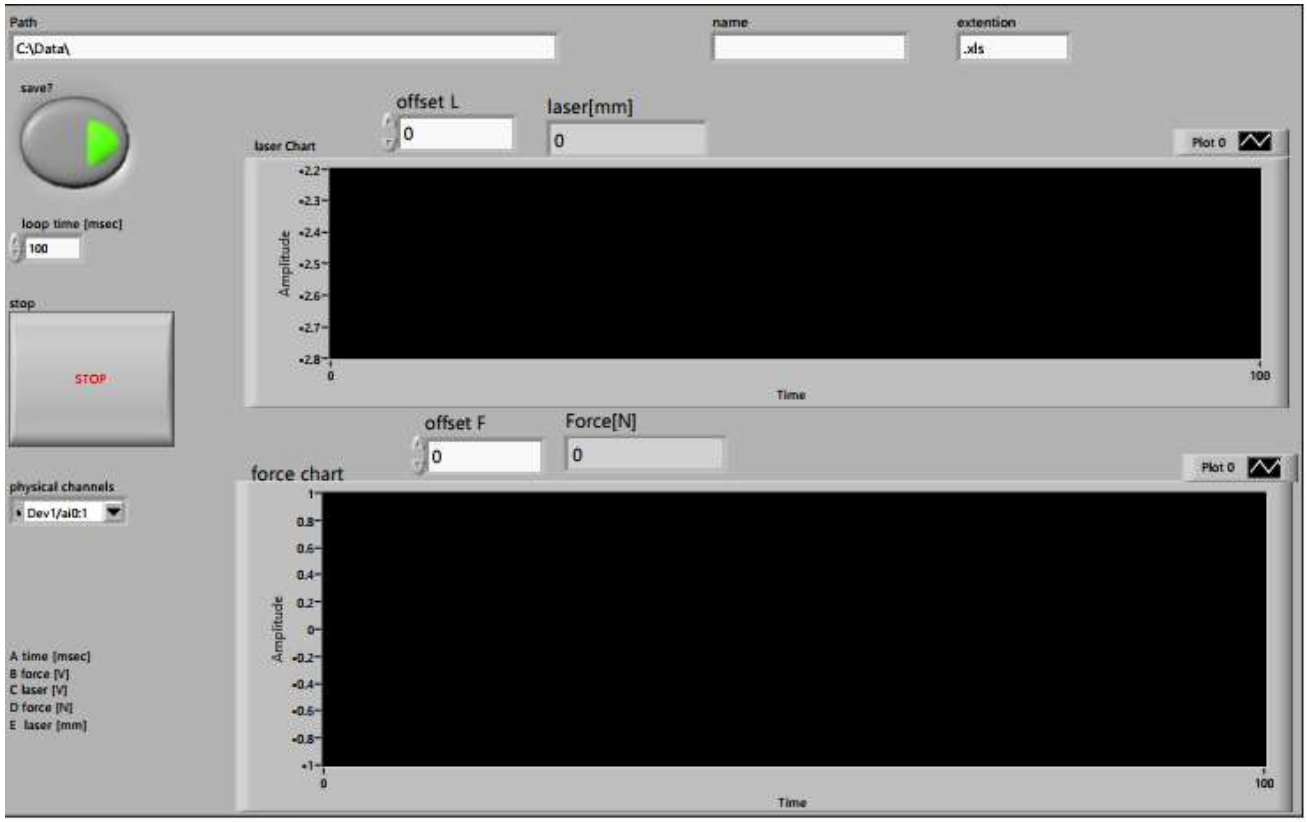

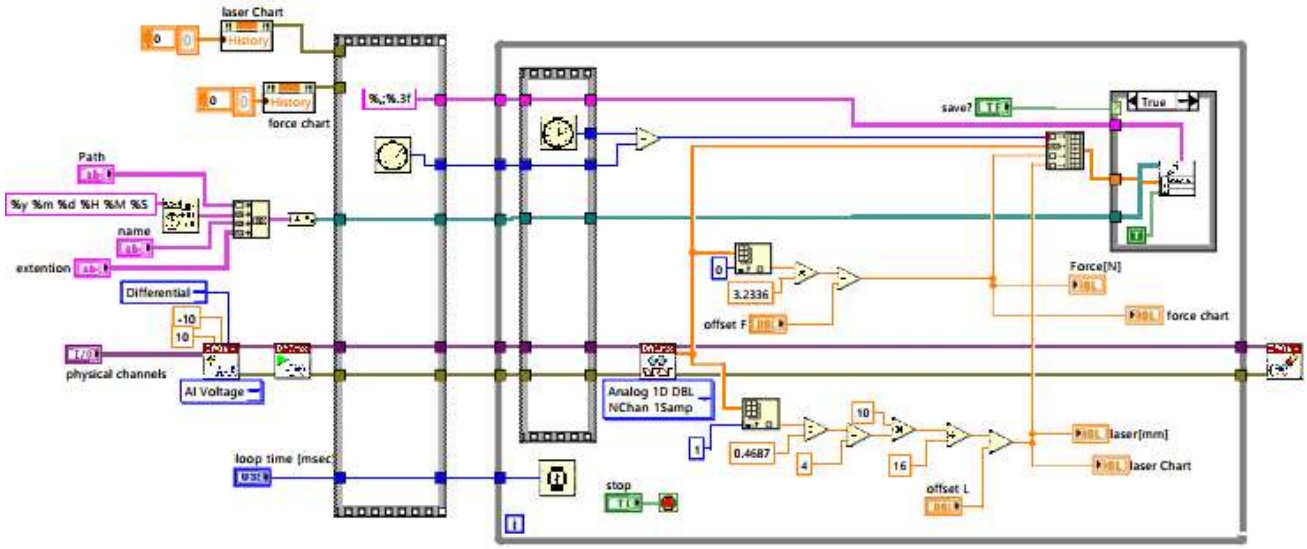

APPENDIX VI LABVIEW PROGRAM MICRO EPSILON ILD1750-2 LASER

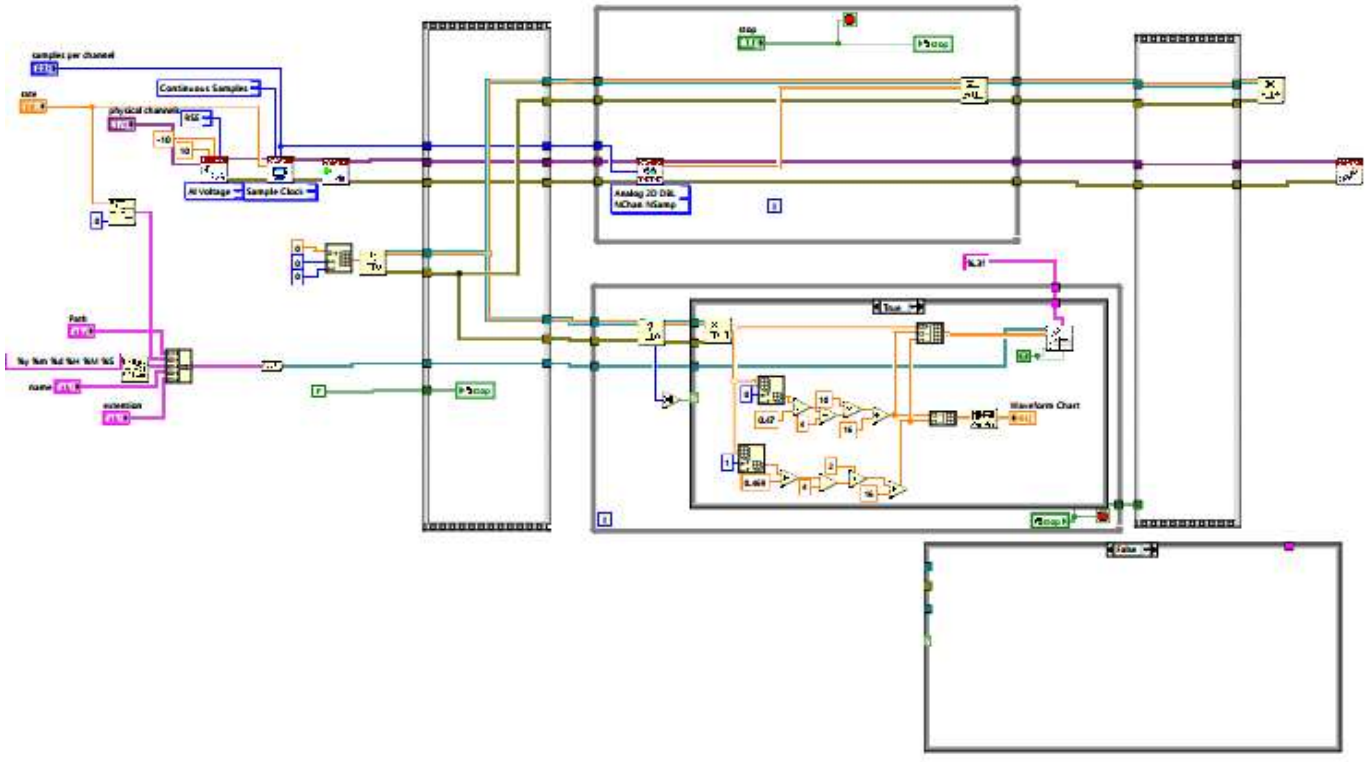

APPENDIX VII CALCULATION MINIMAL THICKNESS

```
%% simplified analytical stiffness approximation

%dimensions
Do  = 14e-3;
Di  = 2.72e-3;
n   =Do/Di;

% stiffness Agilus diaphragm
T   = 0.5e-3;
E   = 0.24;
u   = 0.33;
k_agilus   = (16*pi*E*T^3*n^2*(n^2-1))/(3*Do^2*(1-u^2)*((n^2-1)-4*n^2*log(n)^2))

%stiffness vero diaphragm
syms T real
E   = 2000e6;
u   = 0.33;
k_vero   = (16*pi*E*T^3*n^2*(n^2-1))/(3*Do^2*(1-u^2)*((n^2-1)-4*n^2*log(n)^2))

%total force at 0.8mm extension
F = k_vero*0.8e-3 + k_agilus*0.8e-3

% required thickness vero diaphragm
solve (8 == k_vero*0.8e-3 + k_agilus*0.8e-3, T)
```